All Dissertations   Dissertations

12-2015

ROBUST MODEL DEVELOPMENT FOR EVALUATION OF EXISTING STRUCTURES

Saurabh Prabhu

Clemson University, saurabp@g.clemson.edu

Follow this and additional works at: https://tigerprints.clemson.edu/all_dissertations

 Part of the Civil Engineering Commons

ROBUST MODEL DEVELOPMENT FOR EVALUATION OF EXISTING STRUCTURES

A Dissertation
Presented to
the Graduate School of
Clemson University

In Partial Fulfillment
of the Requirements for the Degree
Doctor of Philosophy
Civil Engineering

---

by
Saurabh Prabhu
December 2015

Accepted by:
Dr. Sez Atamturktur, Committee Chair
Dr. Vincent Blouin
Dr. C. Hsein Juang
Dr. Nadarajah Ravichandran

Abstract

In the context of scientific computing, validation aims to determine the worthiness of a model in supporting critical decision making. This determination must occur given the imperfections in the mathematical representation resulting from the unavoidable idealizations of physics phenomena. Uncertainty in parameter values furthers the validation problems due to the inevitable lack of information about material properties, boundary conditions, loads, etc. which must be taken into account in making predictions about structural response. The determination of worthiness then becomes assessing whether an unavoidably imperfect mathematical model, subjected to poorly known input parameters, can predict sufficiently well in its intended purpose. The maximum degree of uncertainty in the model's input parameters which the model can tolerate and still produce predictions within a predefined error tolerance is termed as *robustness* of the model. A trade-off exists between a model's robustness to unavoidable uncertainty and its agreement with experiments, i.e. fidelity. This dissertation introduces the concept of satisfying boundary to evaluate such a trade-off. This boundary encompasses the model predictions that meet prescribed error tolerances. Decisions regarding allocation of resources for additional experiments to reduce uncertainty, relaxation of error tolerances, or the required confidence in the model predictions can be arrived at with the knowledge of this trade-off. This new approach for quantifying robustness based on satisfying boundaries is demonstrated on an application to a nonlinear finite element model of a historic masonry monument Fort Sumter.

Contents

List of Figures

1 INTRODUCTION

1.1 Motivation

Analysis of civil engineering structures is increasingly reliant on physics-based computational models, thanks to capable and expanding computational resources. However, computational models simply provide approximations of the underlying physics of the structure. Uncertainties inevitably arise in the definition of material properties, support conditions and loading configurations due to lack of knowledge about the system properties [1–4]. Given such unavoidable uncertainty, the accuracy and precision of the predictions of these computational models depend on two main factors: (i) how well the model predictions match experimental observations, i.e. *fidelity*, and (ii) how well the model maintains fidelity under the unavoidable uncertainty, i.e. *robustness* [5, 6]. It has been demonstrated that fidelity to observations and robustness to uncertainty are antagonistic attributes of computational models [7, 8]. Thus, the model developer is required to accept sub-optimal, yet satisfactory predictions in order to ensure the model's usefulness (or applicability) in the entire input parameter domain [9].

Thus, developing computational models of structural systems, keeping both fidelity to experiments and robustness to uncertainty as the objectives, requires analyzing the trade-off between these two attributes. Such a trade-off analysis can allow the model developer to make decisions regarding allocation of resources either to reducing uncertainty by performing more experiments or accepting more error in predictions depending on the importance of the structure and consequence of failure.

1.2 Problem Statement

Traditionally, input parameters of computational models are calibrated to maximize fidelity of experimental measurements [10–15], thus allowing their treatment as an optimization problem. However, as [16] have noted, it is common with this approach to obtain an optimal model that shows large variations due to relatively small perturbations in the problem variables. In other words, calibrated models may demonstrate large variations in their predictions under small perturbations in input parameters [2, 7, 8, 17, 18]. The usefulness of such models is limited for systems, such as historic structures, in which variability (spatial and temporal) and uncertainty (due to lack of knowledge regarding the system properties) is inherent and unavoidable. It is, thus, imperative that the computational model that is developed to represent these structures must be robust to such uncertainty.

1.3 Background Overview

Engineering problems are typically classified as direct or inverse problems [19, 20] (Figure 1). Direct problem, in the context of structural engineering and mechanics, may be regarded as the prediction of structural response to known input parameters [21]. Inverse problem then, refers to inferring the unknown parameters of a system from known (i.e. experimentally determined) system response [10–13]. Thus, inverse analysis can be configured to supply the system parameters for solving the direct problem. In literature, the process of finding solutions to inverse problems appears under different names, e.g. model updating [22–24], calibration [14,15,25], parameter identification [26, 27], back-analysis [28] etc., depending on the specific field.

Published studies on inverse analysis in structural engineering applications is primarily aimed at determining the material properties and boundary conditions from
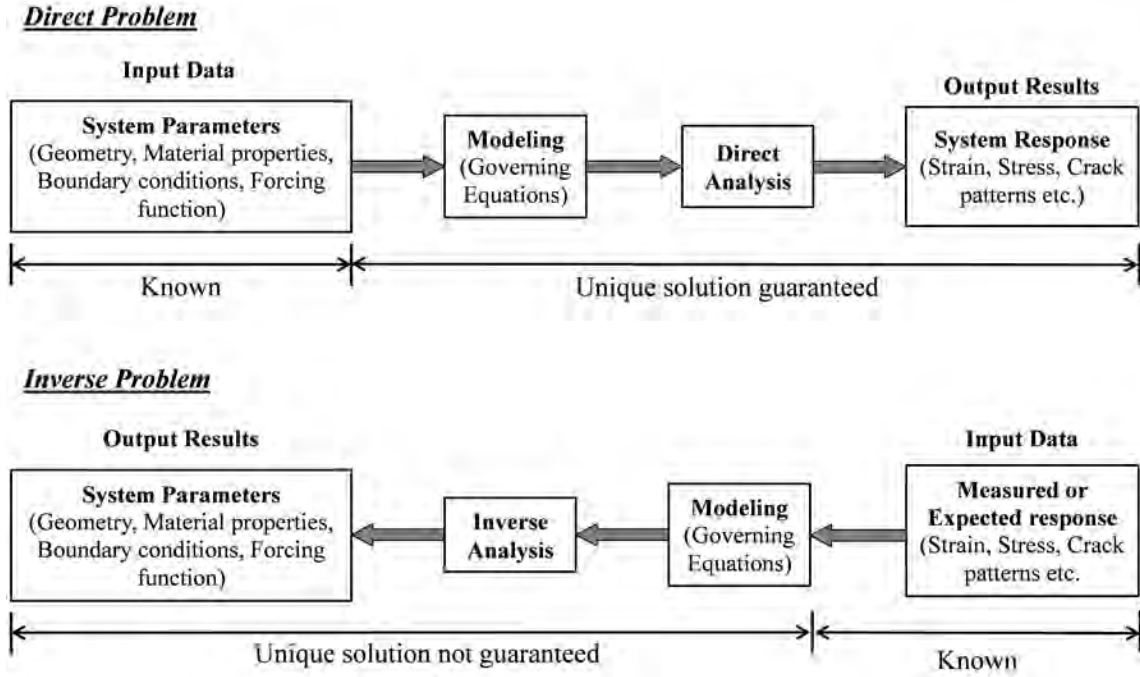
Figure 1: Comparison of process flow in direct and inverse problems.

measurements [25, 29–36] or at determining the damage present in the structural system [37–41]. The latter is typically achieved by characterizing the damage as a function of the material properties and/or boundary conditions. In structural engineering, implementation of inverse analysis techniques to determine the loads from measurements is limited to structural dynamics applications where the impact force is inferred by measuring dynamic response of the structure [42–45], in a well-researched field of study also known as force reconstruction. In most of the applications of inverse analysis in structural engineering, the experimental data is either provided by non-destructive tests on the actual structures or destructive tests on laboratory models.

Inverse problems may be ill-posed [46, 47]. According to Hadamard's definition, a well-posed problem is defined as the one whose mathematical models have the following properties [48–51]:

1. A solution exists

2. The solution is unique

3. The solution is not susceptible to a slight change in the initial condition.

Liu and Han [21] classified ill-posedness of general inverse problems as Type I, Type II and Type III following a thought process very similar to Hadamard's. Type I ill-posedness refers to the non-uniqueness of solutions caused due to the problem being under-posed, i.e. the number of unknowns is greater than number of knowns (second item in Hadamard's definition). Type II ill-posedness is caused due to the insensitivity of the unknowns to the knowns, which may result in an unsolvable problem or a divergent behavior of solutions (first item in Hadamard's definition). Lastly, Type III ill-posedness is caused due to the excessively high sensitivity of the outputs to noise or uncertainty in the inputs, or in other words, the solutions are unstable (third item in Hadamard's definition).

Broadly speaking, a computational model of a structural system is composed of four inputs, namely, the geometry, material properties, boundary conditions and, loads. The governing equations adopted in the model relate these input parameters with the output response. Solution of the inverse problem, in the context of this dissertation, refers to identifying a set of model input parameters that results in model output response that matches experimental observations within specified tolerances on fidelity. Classical parameter identification involves systematically adjusting the parameters in a model until a desired level of fidelity to observations is achieved [12]. In classical parameter identification, as in any inverse analysis, uniqueness of solution is not guaranteed [20, 21]. Several factors contribute to this non-uniqueness. Firstly, the measurements are obtained on a finite number of spatial locations on the system (i.e. spatial incompleteness), while the system response is a continuous function of infinite number of spatial co-ordinates. Also, in the comparison of the model pre-

dictions with observations, a low-dimensional fidelity metric is utilized (even when the observation data is large in quantity, it is typically reduced to a manageable size through data reduction or feature extraction techniques). The low-dimensionality of the fidelity metric makes it susceptible to tightly coupled interactions and compensating effects between parameters [52]. Another source of non-uniqueness of solutions is the uncertainty prevalent in the model predictions as well as the measurements. In civil engineering applications, the sources of modeling uncertainty are numerous (refer [53–55]). Uncertainties in the measurements can be attributed to the measurement error and variations in the system response due to uncontrollable environmental factors. As a result, inverse analysis techniques that are configured to find deterministic solutions that yield optimal fidelity to observations cannot affirm the credibility of the solution, since the model predictions are not guaranteed to be useful after considering all the sources of uncertainty. Robustness of the model to handle the uncertainties is a requirement that is often ignored.

1.3.1 Quantification of Robustness

In this dissertation, robustness of a model is defined as the amount of uncertainty that can be accommodated in the model's input parameters for a desired level of agreement with experimental measurements. Optimal solutions to inverse problems that minimize errors are not guaranteed to be the most robust [56, 57]. Analysis of robustness to uncertainties has been studied in a vast number of fields including engineering, mathematics, networks, biotechnology, finance, social sciences, etc. Irrespective of the application domain, the primary motive of robustness analysis is to study the effects of unavoidable uncertainties on the system outputs of interest [58]. In manufacturing engineering, robust design concept [59] was pioneered by Taguchi in the quality engineering domain for reducing the effects of uncertain environmental

and operational variables on performance and reliability of manufactured products. Since then, robust design has found application in several fields including structural design [60–63]. The objective of robust design in the Taguchi sense is to minimize the variation of system performance due to variations in the design variables and/or uncontrollable environmental and operational variables.

Info-gap decision theory (IGDT) is another robust design technique [64,65] that is fundamentally different from Taguchi methods in that a design is sought that satisfies a given level of performance under uncertainty. The only information required about the input variables is their nominal estimates and no assumptions or knowledge on the error bounds or uncertainty distributions are required. The IGDT approach seeks designs that are least sensitive to hard-to-control variability while maintaining a given level of performance rather than designs that minimize performance variability under uncertainties. While IGDT and Taguchi methods are fundamentally different in their definition of robustness, they do not replace one another.

1.4 Main Dissertation Contributions

This dissertation contributes to the field of modeling and simulation in three distinct ways. First, a novel model evaluation technique is presented that analyzes the trade-off between the model's fidelity to available experimental measurements and its robustness to unavoidable uncertainty. Such an evaluation helps model developers to make decisions regarding a model's usability for the purpose it is meant to serve. Furthermore, such a trade-off analysis facilitates the resource allocation question of whether to perform further experiments to reduce uncertainty or relax fidelity requirements of the model. An additional probabilistic measure quantifies the confidence level in the model in making predictions within tolerable error, offering another

degree of freedom for the model developer.

Secondly, the comprehensive process of model development is demonstrated on a case-study full-scale historic monumental structure, beginning from on-site data collection to the calibration of model using non-destructive test data. Using this model, the full-scale engineering application of the satisfying boundary concept is tested and the practical issues of the application are explored.

Lastly, an approach is developed that can relate structural damage to the structure's loss in strength in terms of its load-carrying capacity. A novel measure of structural redundancy is formulated which accounts for the position of damage relative to the applied operational loads on the structure. The loss in redundancy due to damage is quantified as the consequent change in the structure's internal load paths between the load and the supports.

Along with model evaluation, this dissertation provides a thorough account of the process of model development of existing structures using on-site destructive and non-destructive tests, which acts as a significant addition to the knowledge base for computational modeling of historic masonry monuments. The contents of this dissertation are submitted as four separate articles to peer reviewed journals.

1.5   Dissertation Overview

Chapter 2 contains an overview of the computational modeling techniques commonly used for evaluation of masonry structures. Some of the subsections in this chapter are part of a review paper accepted for publication in The Masonry Society Journal [66]. Other subsections are part of a proceeding paper published by EuroDyn [67].

The concept of satisfying boundary introduced in Chapter 3 produces a trade-off between the uncertainty in model input parameters and maximum prediction error

that can be tolerated. A third criteria which is the probability of satisfying is introduced to quantify the confidence in the model predictions to meet prescribed error tolerances under uncertainty. The decisions that can be arrived at using the resultant trade-off analysis are discussed. This chapter also compares some of the existing model evaluation metrics with the proposed approach. This chapter is conditionally accepted for publication in Computers and Structures Journal (Elsevier) [68].

The concept of satisfying boundaries is first demonstrated on a controlled academic example which exhibits strict proper continuous behavior. To evaluate the concept on a non-trivial example a full-scale model of an existing unreinforced masonry monument is developed in Chapter 4. The process of model development is first detailed, covering on-site experiments, incorporation of the experiments in the computational model and finally, calibration of the model to vibration test data. The model is used to make predictions under differential foundation settlement and a qualitative metric is defined to evaluate the extent of damage. Uncertain input parameters are calibrated to experimental data gathered via vibration testing with fidelity as the objective. Next, the analysis of trade-off between robustness and fidelity is performed according to the satisfying boundary concept to assess the usability of the model in making predictions of response to foundation settlements. Practical considerations and discussion on decision making using the trade-off analysis is also provided. The contents of this chapter have been published in Engineering Structures Journal [69].

In Chapter 5, the computational model of the historic masonry monument developed in Chapter 4 is used to demonstrate a novel measure of a structure's post-damage loss in redundancy, which is based on load paths within the structure. Using this redundancy measure, non-destructive measurement that characterize structural damage can be related to the remaining load-carrying capacity by developing empirical relationships. This chapter has been submitted to ASCE Journal of Structural

Engineering [70].

Finally, Chapter 6 provides the conclusions of the dissertation long with the major findings of each chapter. Also, the limitations and avenues for expansion of the study are given in this chapter.

2   LITERATURE REVIEW

Much of the world's architectural monuments are survived by their masonry elements. However, these masonry monuments are continually degraded by the multitude of physical, chemical and biological processes that subvert their material and structural characteristics. At critical levels, the degradation caused by these processes may lead to structural failure and to the ultimate loss of these culturally-significant monuments. Examples throughout the last century include the 1902 collapse of St. Mark's Campanile in Venice, Italy, the 1989 collapse of the Civic Tower of Pavia, Italy [71], the 1990 collapse of the Church of Kerksken, Belgium [72]; the 1992 collapse of a bell tower at the church of St. Maria Magdalena in Goch, Germany, the 1996 collapse of the Noto Cathedral in Sicily Italy [73]; the 2006 partial collapse of the Maagdentoren Tower in Zichem, Belgium [74] and the bell tower of the St. Willibrordus Church in Meldert, Belgium [74]. While failures such as these are typically sudden events, the preceding processes of material and structural decline tend to be gradual, often going unaddressed for extensive periods.

The processes of gradual, time-dependent degradation typically occur in three phases [75] (Figure 2). In the first phase, initial instances of material degradation occur at a local level. In the second phase, degradation progresses in severity and can spread to affect the structural components of a monument. In the third phase, structural damage caused by gradual material degradation can lead to secondary damage in an exponential manner and to the ultimate failure of vital structural elements. In a structural health monitoring framework, damage from the first phase may be imperceivable while detection of that from the third phase may not provide sufficient time for intervention. Health monitoring and damage assessment should therefore focus on damage from the second phase in order to provide timely warning of the

10
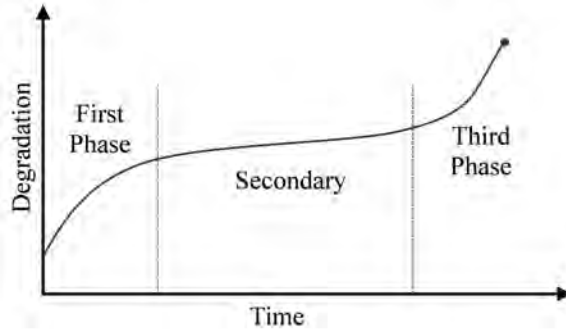
Figure 2: Three phases of continual degradation leading to ultimate failure.

oncoming third phase and the possibility of structural failure.

Historic masonry structures are subjected to a variety of physical processes that slowly degrade their material composition. Differential foundation settlement, a common problem amongst historic masonry buildings, can pose a direct threat to the overall integrity of a structure. While the process of settlement does not typically continue indefinitely, changes in the local groundwater level or soil moisture content, nearby excavation activities [76–78], nearby vibration sources (i.e. construction, railroads, vehicle traffic, etc.) [79–81], and the decay of wood piles (if used beneath the foundation) can lead to increased foundation settlement long after a monument's initial construction has taken place and the weight of the structure itself has caused initial compaction in the soil beneath the foundation.

Given the large weight of historic masonry monuments, creep (a material process that involves the gradual and permanent deformation under long-term loading) can contribute to the slow, gradual decline of masonry materials and may ultimately lead to structural failure [82, 83]. For instance, the collapses of both the Civic Tower of Pavia (Italy) and the Tower of Maagdentoren (Belgium) are attributed to increased strains in heavily loaded elements due to creep [84]. Furthermore, temperature fluctuations over several years lead to weakening of the unit-mortar bond primarily due

to variations in thermal expansion properties and inception of tensile stresses [85].

Persistent, chemical and biological processes also cause gradual degradation of the composition and durability of masonry materials. In many of these processes, water is a key factor that can both initialize and sustain the processes of weathering, ice formation, freeze/thaw cycling, capillary flow, and biological growth [86–89]. At the macro-scale, historic masonry buildings may fall under the attack of larger plant systems [90–92]. The continual growth of these plants, as well as their invasive root systems, cause stresses in the masonry materials that can lead to pervasive damage. As the size and complexity of these plant systems grow with time, their damaging effect on masonry structures can worsen.

Preservation of the heritage structures is pivotal in the conservation of the culture and history of a region for future generations. The assessment of the structural safety is a major component of any preservation effort, which is increasingly reliant on computational modeling. The following section overviews the practices in computational modeling of historic masonry including the modeling philosophy, obtaining and recreating geometry, material behavior assumptions, element and meshing options, and calibration of input parameters.

2.1   Computational Modeling of Masonry

Computational modeling historic masonry presents a unique set of challenges, mostly related to lack of information regarding composition, materials, construction history and support conditions for defining the model's input parameters and geometry. Parameter values that cannot be obtained directly must be inferred via calibration of the computational model to match model predictions with experimental measurements. Notwithstanding, uncertainty in the parameter values cannot be entirely eliminated

for the following reasons:

(i) *Spatial and temporal variation in the masonry material.* No two masonry units in a historic building show the same material properties, given the workmanship and varying degradation patterns. The properties are also sensitive to moisture level and ambient temperature. Masonry is essentially a composite of unit and binder. Since modeling every brick unit and mortar is impractical for full-scale structures, homogenized material properties have to be assumed over the volume of the structural components leading to idealization errors [93].

(ii) *Lack of knowledge of the structure's interior composition.* The internal composition and degradation characteristics on masonry components is most often unknown and hard to evaluate. Thus, assumptions often have to be made regarding masonry that cannot be directly observed. The presence of internal damage adds to this uncertainty.

Given the current and continuing advancements in computational processing power, model developers can accommodate this unavoidable uncertainty in the model's predictions. Therefore, it is only appropriate for the model developer to embrace the presence of uncertainty and errors in model-based decision making.

Unreinforced masonry exhibit a highly non-linear behavior owing to low tensile capacity and composite nature. Furthermore, the complex geometries of the curved members found in most historic monuments makes the use of analytical relations impractical for full-scale structural analysis. Three-dimensional finite element (FE) modeling has proven successful for the non-linear structural analysis of historic monuments due to its capabilities in creating complex geometries, incorporating non-linear material behavior and utilizing high-performance computational resources for predicting a wide range of system response and easy visualization of the predicted results [25,94,95]. Some of the pioneering studies that applied FE modeling to struc-

tural analysis of historic monuments include [96–101]. The primary difficulties in development of FE models arise from the selection of modeling type, recreating the geometry, and selecting material behavior, boundary condition and element formulation. Each of these issues are discussed in the following subsections in the context of historic masonry structures.

2.1.1 Modeling types

The accuracy of the computational model largely depends on the accuracy with which the mechanical behavior of the heterogeneous composite masonry is reproduced. Indeed, the selected modeling type affects every subsequent step of the model development process. In unreinforced masonry (URM), tensile cracking is the most primary form of damage. Cracking leads to formations of internal hinges in the structure and once a sufficient number of hinges is formed, the structure can collapse without clear visual warning in the form of large deformations. Thus, any modeling approach adopted for URM must account for cracking of the material.

Three plausible modeling strategies are available to model the masonry composite: (i) detailed micro-modeling, (ii) simplified micro-modeling and (iii) macro-modeling [102–105]. *Detailed micro-modeling* provides the most realistic representation of the masonry assembly by modeling the units and the mortar separately and assigning independent material properties for the two [103, 106–111]. Detailed micro-modeling, however, requires the highest effort in development of the geometry, thus demanding highest computational effort, limiting its application to smaller components of a building such as walls and arches [103]. Micro-modeling is recommended only when local failure modes within structural elements are of interest. In the *simplified micro-modeling* approach [112–119], the each unit and the surrounding mortar is homogenized into a single fictitious unit, a.k.a. Representative Volume El-

14

ement (RVE), with homogenized material properties. *Macro-modeling* assumes the masonry composite as a homogenized continuum throughout the structural member, making no distinction between the masonry units and joints. Macro-modeling is the most commonly used modeling strategy for full-scale structures owing to its geometric simplicity and relatively low computational effort.

In a comparative study of the three modeling approaches on a model of a scaled masonry dome [102], detailed micro-modeling was found to be most accurate in the prediction of load-carrying capacity, stiffness, and distribution of cracks, while macro-modeling was the least accurate. Although micro-modeling provides the most accurate predictions, it is computationally intensive, requires hard-to-obtain material parameters defining friction behavior and bond strength. Furthermore, for using detailed micro-modeling and simplified micro-modeling approaches, two feasibility conditions must be satisfied: (i) the bond pattern or RVE is repetitive throughout the structure and (ii) the knowledge of the masonry bond type beneath the surface is known. Also, it is not feasible to model every brick and mortar joint separately for medium to large scale structures. Moreover, additional material parameters entail additional sources of uncertainty in the parameter values.

Modeling support settlement: This dissertation is focused on the simulation of foundation settlements of historic structures. Previously, a number of modeling strategies have been employed for extracting structural response to settlement. For instance, [120–122] have used the simplified micro-modeling approach to simulate foundation settlements in unreinforced masonry structures. The masonry blocks were modeled as elastic or rigid volumes while the joints are idealized either as frictional contacts or contact surfaces with tensile and shear strengths governing the separation of the blocks. Differential settlements in masonry buildings have been studied most

commonly using the macro-modeling approach. For instance, Liu et al. [123] investigated the damage to masonry buildings due to tunneling induced settlements using 2D FE model with elastic no-tension material model to represent masonry. In this study, the elements were assumed to be cracked if the principal stress state is tensile. The cracking was smeared across the element by assuming a small value of stiffness in the direction normal to the major principal stress direction. A similar treatment can be seen in [77, 124–126]. Rots [127] used a smeared cracking approach to represent fracture in masonry to simulate settlement damage due to settlement of historic masonry monument in Amsterdam. Invernizzi et al. [128] presented the results of a FE analysis of differential settlement of a two-span masonry arch bridge using the smeared cracking approach governed by specified limit tensile and compressive strengths. Domede et al. [129] analyzed a masonry arched railway bridge for failure load after applied differential settlement. A homogenized orthotropic material model was assumed using a smeared crack analogy with the possibility of crack opening and closing. These studies emphasize the requirement of incorporating post-cracking behavior of masonry for analysis under differential settlements. In this dissertation, macro-modeling approach is employed due to (i) relative difficulty in regenerating the complex structural geometry by modeling every brick and joint individually, (ii) lack of knowledge of the bond type underneath the surface layer, (iii) lack of knowledge of the brick-mortar interface characteristics, and (iv) significantly lower computational demand.

2.1.2 Geometry

Construction drawings, if available may be used to recreate the solid geometry. These drawings, however, rarely match the on-site geometry owing to any age-related permanent deformations (for instance, foundation settlement and creep). On the other

hand, on-site measurements which ensure the recreation of the as-is geometry, can be time-consuming, especially for a large building with inaccessible components. 3D photogrammetry [130–133] is a fast and accurate technique that allows visualization of the structure to account for existing cracks and other structural degradation of the masonry. These techniques, however only provide information on the surface of the masonry. The thickness of the members beneath the surface must be obtained either via direct measurement, if possible or from construction drawings.

3-D laser scanning [132, 134–136] is another fast and accurate technique that is gaining popularity. The laser scans typically produce a cloud of points, which can be reduced in a CAD modeling software to specific keypoints preserving the structurally significant features of the monument. If the interior surfaces of a structural component, such a wall or a vault are accessible, with the 3-D laser scanning, the thickness of members can be obtained by stitching the scan data.

In situations where the rear region of the walls and vaults is inaccessible and there are no readily available holes to measure the depth, non-invasive techniques such as impact-echo, impulse radar, sonic tomography or electromagnetic conductivity [137] may be used to determine the thickness. The unit dimensions and mortar joint depth are typically assumed to be perfectly uniform throughout the structural member, thus disregarding the minor variations due to uneven workmanship, minor material degradations as well as non-structural elements. Such property-preserving simplifications, while making the process of geometry creation and meshing much easier, negligibly affect the model predictions.

2.1.3   Material Properties and Material Models

Unreinforced masonry (URM) is one of the oldest but least understood building materials still in use. Key characteristics of URM include highly non-linear behavior

17

owing to low tensile capacity and composite nature. Accurately defining material properties is challenging because of the spatial and temporal variability of material properties, typical of historic structures. At best, one may obtain samples from the site in the form of cores or loose material. In such samples, however, large sample-to-sample variability is typically observed [138–140]. If distributions of the material property values are available through testing of a large number of material coupons or samples, these distributions may be used as prior distributions to calibrate the input parameters that define the material behavior.

Masonry may be viewed as a composite material with rigid blocks bound by soft mortar. However, in realistic full-scale applications, macro-modeling approach is invariably used where masonry is treated as a homogeneous material where homogenized properties of the masonry assemblage are obtained either from tests on the assembly or using one of the numerous homogenization techniques [117,118,141–149]. The primary mode of failure of masonry material is brittle tensile cracking, which is why obtaining tensile properties is necessary for prediction of structural damage due to applied loads. Although masonry behavior is largely non-linear due to the formation of extensive micro-cracking, a simple linear elastic treatment of the material is justified under small loads, such as self-weight, to understand the stress distributions and to identify regions with high tensile stresses [150–152].

2.1.4 Boundary Conditions

Computer models often focus on the components of larger structural systems, for instance a single bay of a Gothic Cathedral or a single casemate of a fort or the bell tower of a church. Defining the structural behavior at the boundaries between modeled and unmodeled components of a structural system is a challenging undertaking [153, 154]. Theoretically fixed or free boundary conditions that are readily

available in most structural analysis software packages are only approximations of the complex, semi-rigid behavior of real life masonry systems at their boundaries. The restraining forces at these boundaries are dependent on the masonry material properties and the configuration of the adjacent members. Unlike material properties, non-destructive test methods to estimate such boundary conditions are limited.

One suitable technique for accounting for boundary conditions is *substructuring*, which essentially reduces the adjacent structure to its interface degrees of freedom that it shares with the structure of interest to form superelements. This approach is advantageous for structures with repetitive geometries such as Gothic cathedrals, forts, etc. since the same FE model may be used to generate the substructures of adjacent structures.

Component mode synthesis [155–158] is usually employed for dynamic analysis of large structures. The method consists in dividing the structural system into a number of substructures or components and then coupling the components to form the reduced system. This approach is useful for analyzing a specific component of a structural system where reduced order models of the adjacent components are employed on the interface. Component mode synthesis involves three principal steps: (i) division of the system into components, (ii) calculation of component modes and (iii) coupling of the component models to form the reduced order system. The component modes of each structure are calculated independently which are then assembled systematically through compatibility constraints.

Another widely used technique to approximating the boundary conditions is applying translational and rotational springs at the boundary with assumed (but unknown) spring stiffness [153, 154]. These stiffness constants must then be calibrated using non-destructive test data. A parametric analysis, with the spring stiffness as the variable, may be completed to define a range of stiffness values that lead to a

19

semi-rigid connection. This range can be identified by observing the response of interest of the system at varying spring stiffness and selecting the range in which the response of interest varies between an upper and lower converged limit.

2.1.5 Element Type and Meshing

In the context of FE modeling, the cracking and crushing damage in the masonry, which is assumed as a continuum, is usually incorporated in either a smeared sense or discrete sense [152]. Under the smeared crack assumption cracking and crushing is modeled via modification of the material properties of the damaged elements [152, 159]. As such, geometric continuum is maintained throughout the solution. In the discrete crack approach, cracking is accounted for via modification in the geometry by disrupting continuum or elimination of elements. The discrete approach becomes infeasible for large scale structures due to its heavy computational demand.

Many available FE software packages commonly offer dedicated element types that offer smeared crack analogy. For instance, the SOLID65 element provided by ANSYS was originally designed to emulate concrete [160, 161]. The element introduces a plane of weakness in the direction of the failure by modifying the elastic modulus at the element face to a near-zero value, thus replicating the cracking behavior while maintaining mesh continuity. Consequently, this and other elements have been extensively applied to model the unique material properties and geometric irregularities of historic masonry structures [104, 162–164].

The meshing of the FE model must achieve a suitable balance between solution accuracy and computational time. A coarse mesh can degrade solution accuracy while an overly fine mesh can result in excessive computation. A mesh refinement study may be performed by predicting the response of interest at varying mesh sizes followed by an extrapolative calculation of a reference solution [165–167]. The reference solution

is an approximation of the solution corresponding to an infinitesimal element size yielding a theoretically-exact solution. A mesh size must be sought that yields an error with respect to the reference solution that is less than the expected measurement error, which is indicated to be around 10% for large scale civil structures under normal operational conditions [154].

2.1.6 Calibration of Input Parameters

In developing computational models, often the input parameters defining the material and boundary conditions are not directly measurable via experiments. When measurements are available, the spatial and temporal variability still exists in the parameter values. In such situations, measurable quantities that are sensitive to the model input parameters are first obtained via experiments. The input parameters are then adjusted such that model predictions of the measured quantity match the experimental values. This process of systematically adjusting input parameters such that model predictions show maximum agreement with experimental measurements is termed as calibration [15, 168, 169]. To obtain experimental data for correlation, vibration testing is most common for historic structures due to its non-destructive nature. In most applications, material properties that define the stiffness, mass, and damping as well as parameters defining support conditions are calibrated to linear vibration response features such as mode shapes, natural frequencies as well as to the raw time and frequency domain response and their derivatives. Prominent examples of calibration process applied on full-scale masonry monuments using vibration features include [153, 170–178].

Selection of comparative features: The comparative features are the low dimensional signatures extracted from both the model predictions and experimental

measurements. As their name indicates, they serve as a link between test and analysis. Hence, feature extraction is essentially a process of data reduction where a large number of raw data points are reduced to a much smaller vector or a scalar quantity. Comparative features must be selected such that they are sensitive to the selected calibration parameters. A variety of comparative features which can be extracted via on-site dynamic measurements, such as temporal moments and regression characteristics of the time history data, are discussed in [179]. Features most commonly implemented during calibration are the modal parameters including natural frequencies and mode shapes. It must be noted however that modal parameters only allow calibration of the linear parameters in a model, such as elastic modulus, density and linear boundary conditions. For calibration of non-linear parameters such as tensile strength, destructive and semi-destructive tests would be needed [180, 181]. Thus, the process of selecting comparative features and calibration parameters depends on the calibration goals and available experimental data.

Selection of calibration parameters (uncertainty propagation, effect screening): The selection of a model input parameter as a calibration parameter depends on its sensitivity to the model prediction of interest as well as the uncertainty regarding the parameter's precise value. These two factors of sensitivity and uncertainty are assessed in combination in the Phenomenon Identification and Ranking Table [182–184], based on which, a decision is made on the selection of calibration parameters. In the absence of sufficient experimental data, one common approach is defining parametric uncertainty using expert opinion on the minimum and maximum bounds and assuming a uniform distribution within these bounds. Prior to the selection of calibration parameters, a sensitivity analysis must be conducted. The first goal of sensitivity analysis is to ensure that the comparative feature is sufficiently sen-

sitive to the selection of calibration parameters. The second objective of sensitivity analysis is to assess the interactions between the parameters and their combinatorial effect on the comparative feature. If the parameters are strongly interdependent, calibrating one parameter may compensate for the inaccuracy in another parameter and ultimately lead to an unsatisfactory model calibration. The effect of interdependency or correlation between parameters, once identified, may be resolved either by holding one of the correlated parameters at its nominal value (assuming that reliable information regarding the nominal value is available) or by performing co-ordinate transformation on correlated parameters to obtain new uncorrelated parameters.

Test analysis correlation and associated metrics: As the name suggests, test-analysis correlation involves systematic correlations between the comparative features obtained from model predictions and experimental measurements. For such comparison however, a suitable metric that quantifies the agreement (or lack thereof) in the comparative feature must first be defined. The definition of this metric closely depends on the nature of the comparative features. A select few examples of such metrics include the Euclidean distance, i.e. the absolute geometric distance between two points [185]; the Mahalanobis distance, i.e. the weighted distance between a point and a population that considers the correlations [186]; and the Bhattacharyya distance, i.e. the weighted distance between two populations that also considers the correlations [187].

Calibration procedure: The goal of calibration is to adjust the parameters such that the test-analysis correlation metric is improved. The two common approaches to parameter calibration are (i) optimization-based techniques [153], which often treat the model predictions and experimental measurements in a deterministic manner and

(ii) probabilistic techniques [170], which acknowledge the inherent uncertainties in the model predictions and experimental measurements. A notable probabilistic approach is Bayesian inference, which has recently received attention from those involved in the modeling and simulation of masonry monuments [176]. It must be emphasized however that calibrating parameters of a model against experiments neglects any potential biases that might be present in the model due to unavoidable model imperfections. Such biases, which may result from simplifying assumptions established during the development of the geometric model or through the use of a homogenized, macro-model representation of the heterogeneous masonry and mortar assembly, are commonplace in modeling masonry monuments. Bias in model predictions can be approximated through an independently developed error model. Such a model, once trained, can also be used to bias-correct the model predictions. Of course, training of this error model must be completed simultaneously with the parameter calibration. Recently, methods have been developed to simultaneously fine tune calibration parameters and train a model to represent bias [188]. Another future area of study may lie in the development of methods for the determination of predictive maturity among computational models to establish a more quantified level of confidence in model predictions [189].

3 THE CONCEPT OF SATISFYING BOUNDARY

3.1 Introduction

Despite of how sophisticated and detailed they might be, computer models can only provide approximations of the reality they are built to represent. As the famous declaration of statisticians George Box and Norman Draper reminds us, "all models are wrong, but some are useful." Thus, the *raison d'etre* of a model is not to be a *correct* representation of reality, but to include sufficient realism to be useful in decision making [190]. Model prediction accuracy and precision are therefore necessary only to the extent that they contribute to the answers for the questions asked of the model [191]. In this chapter, we are concerned with assessing the usefulness of physics- and/or engineering-based models in aiding our understanding of and our ability to probe the reality of interest. We should therefore consider the three distinct components of the development process for such models:

1. the domain in which the problem will be evaluated, typically defined by the control parameters that dictate the environmental or operational conditions of the system,

2. the mathematical representation of the underlying processes, also referred to as model form, defined in accordance with the identified domain,

3. the input parameters that characterize the properties of the system of interest in accordance with the mathematical representations.

Proper determination of the domain is one of the first and most critical steps in predictive modeling as the model's internal structure will be determined according to this domain. Hence, the domain of interest must be defined strictly based upon

what is necessary for decision making. Herein, we will conveniently[1] assume that the model developer has identified the suitable domain (item 1) and focus our attention on the selection of a model form and its associated parameter values (items 2 and 3).

Item 2 declares that no model form is a perfect representation of reality and is closely associated with item 3, which emphasizes the lack of knowledge in the values of (a subset of) input parameters for virtually all models concerning non-trivial, real-life systems. The close association of items 2 and 3 raises the following question: should we use parameter values that suitably compensate for the model form's imperfectness or rather those that most accurately depict the real parameters? The former is typically what is achieved by calibrating model parameters against experiments and of course, the latter is only possible if the parameter has a physical, measurable meaning (i.e. density of a material, geometric dimension, etc.). How should we approach this problem then if a model's parameters have no physical meaning, or worse, if those with physical meaning are wrongly excluded during model idealization? As seen, a great many complications arise in the selection of input parameters for imperfect model forms while no universally accepted approach exists to help in their determination. One logical way of approaching this problem is to ensure that the selected mathematical representation (i.e. model form) must not only provide sufficiently accurate predictions of observable reality[2], but that it must do so given uncertainty in its own parameter values. We will call the capability of a model form in accommodating parametric uncertainties as robustness [192, 193]. A model is then said to be robust if its predictions remain within acceptable fidelity bounds despite variations in its input parameter values. Models that afford higher uncertainties while satisfying a

---

[1]Note that we have also conveniently assumed that model yields converged solutions within the time and spatial domains and that numerical uncertainties are of little concern.

[2]Of course, the observables must be in sufficient quality and quantity to identify the model's flaws.

predefined agreement with experiments would therefore be preferable [192].

The objective of this chapter is to develop and illustrate decision-making indicators for model selection that effectively evaluate a model's usefulness for its intended use. The indicators presented in this chapter provide information about the structure of the input-output domains and the eventual pitfalls and windfalls that can occur as model evolves through the input parameter domain during a search for a better agreement with experiments in the face of uncertainty. This chapter is organized as follows. Section 3.2 of this chapter overlays the proposed approach to evaluating fidelity and robustness of model predictions based on the concept of a *satisfying boundary*. An optimization based approach to obtain the proposed satisfying boundary is presented in Section 3.3. The development of a case study application involving the proposed approach is presented in Section 3.4. Section 3.5 presents a discussion of the implications of this approach using the case-study application along with generalizations to a wide range of practical problems. In Section 3.6, some existing model selection criteria are put in the perspective of the proposed approach. Finally, Section 3.7 concludes the chapter and discusses limitations of the proposed approach as well as the future direction for improvement.

3.2   Concepts and Methodological Perspectives

In engineering and science, there are many of problems in which the probabilistic knowledge of parameters involved is incomplete or entirely unavailable, but the parameter values can be defined in a bracket with plausible minimum and maximum values [194]. In such situations, representing such poorly known parameters with bounded uncertainty (rather than assuming questionable probabilistic distributions) offers a meaningful alternative. Following the discussions provided by Elishakoff [2]

and Ben Haim [195], we will represent the compact space of input parameters by predefined intervals of bounded uncertainty.

Now, let us consider a model that is a proper, uniformly continuous function within the compact space of its uncertain parameters, where an admissible, finite change in the input parameters will yield a small, finite change in the model's output (i.e. micro-continuity). Hence, unstable systems which may yield disproportionately large changes in their output due to small perturbations in their input are left out of the scope of our discussion. Now, the implication of confining our scope to proper uniformly micro-continuous functions is that for a compact space of input parameters, the model's output will be compact (i.e. closed and bounded) (see Figure 3).

Within the compact output, it might be tempting to seek for the solution that yields the best agreement with available experiments. Seeking this so called "best-fidelity" solution would require that experimental measurements are collected with certainty and are available in sufficient quantity, the ideal metric for calculating the agreement (or lack thereof) between the predictions and measurements are known, the input parameters to be calibrated are orthogonal in that they do not compensate for each other, and the model bias is negligible in that it does not interfere with parameter calibration. In practical applications, these requirements are rarely satisfied and compensations inevitably allow multiple combinations of input parameter values (those both correct and appear to be correct) to yield predictions of similar fidelity, a phenomenon known as non-uniqueness [196]. Thus, a model developer relying solely on fidelity and seeking for the solution that yields the best agreement with available experiments may become unable to distinguish between truly accurate models and those that have benefited from compensations.

With a focus on organizational decision-making and emphasizing the idealized nature of analytical methods, [197] and [198] both suggested evaluating all alternative

solutions that satisfy a minimum threshold rather than selecting single best solution. Following this idea, we can identify the realizations, which satisfy a certain *error tolerance* when compared with experimental observations. Here, we will leave the definition of error and its associated metric up to the user; virtually any measure of error can be applied. Error tolerance is the criteria with respect to which the model's adequacy to fulfill it's purpose will be assessed (see [199] for a discussion on how such criteria can be determined).

Here, we introduce the concept of a *satisfying boundary* that encompasses all model input parameter sets that satisfy the prescribed error tolerance. From another perspective, this boundary marks the periphery beyond which lie combinations of parameter values that yield unacceptable model predictions. This boundary exists as an n-dimensional hyper-volume where n is the number of model input parameters to be evaluated. The volume encompassed by this boundary reminds us Starr's domain robustness criterion [200]. Obviously, the shape and the size of the satisfying boundary are strongly dependent upon the model form itself. Intuitively speaking, two alternative model forms with the same set of uncertain parameters, the model with a larger satisfying boundary, i.e. larger volume of the n-dimensional hypervolume, can accommodate higher levels of uncertainty while meeting the error tolerance requirement.

We build upon this concept and closely integrate two independent pieces of information: a satisfying boundary that is intrinsic to the model form and the bounded uncertainty space that is intrinsic to the uncertain model parameters. Here, we determine a model's *probability of satisfying* a given error tolerance for a given level of uncertainty in its parameters. Hence, for a given error tolerance and uncertain parameter space, a model's performance can be quantified by comparing the parameter sets contained within the satisfying boundary to those contained within the uncertain
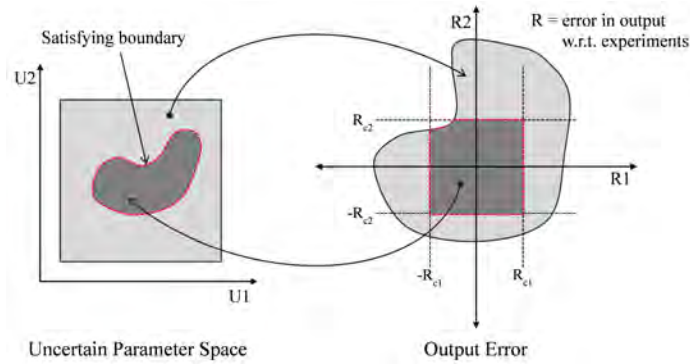
Figure 3: Conceptual figure showing the mapping from uncertain parameter space to output space and the compact satisfying boundary.
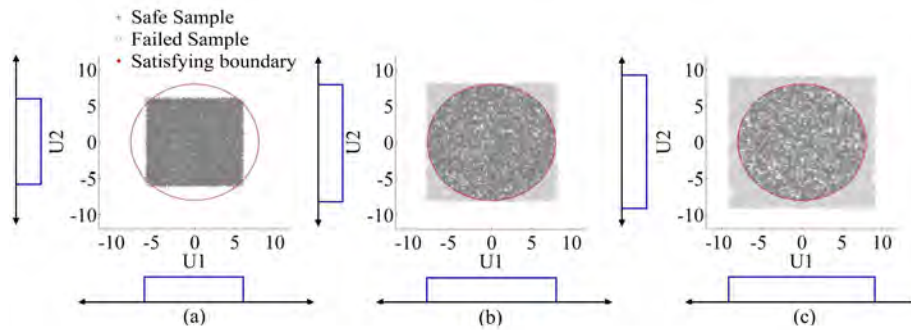
Figure 4: Probability of satisfying the error tolerance for a 2-parameter model given three distinct parameter spaces are (a) 99%; (b) 79%; and (c) 62%.

parameter space. Accepting the principle of indifference, this comparison can be accomplished by calculating the ratio of respective volumes. Hence, the ratio of volume defined by the parameter sets that are encompassed by the satisfying boundary to the volume defined by the uncertain parameter space yields the model's probability of satisfying the error tolerance. Figure 4 demonstrates how this ratio can be calculated for a two-parameter model for increasing bounded uncertainty[3].

The knowledge of the satisfying boundary can help determine the influence of parameter uncertainty on the output of a model. For instance, for a given error tol-

---

[3]If one has better knowledge regarding the parameter values however, nothing prevents him/her from incorporating this knowledge in this step.
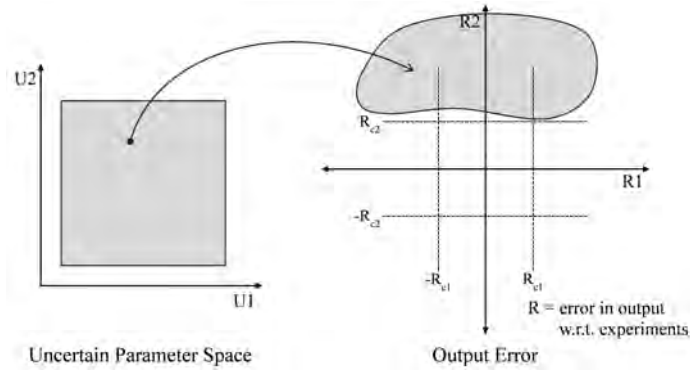
Figure 5: Conceptual figure showing the absence of a satisfying boundary as output errors fall outside the error tolerance.

erance, if 100% of the parameter value sets within the bounded uncertainty space are effectively contained within the satisfying boundary, parameter uncertainty can be deemed inconsequential as the model predictions satisfy the error tolerance requirement regardless of lack of precise values for the parameters. Thus, the model form can be said to be robust and able to make reliable predictions. However, if this is not the case, then we can resort to quantifying the probability that the model output will satisfy the error tolerance given the uncertainty of its parameters. For the desired error tolerance, if the probability of satisfying is inordinately low, it may indicate a problem with either (1) the model form or (2) the uncertain bounds suggesting that we must invest in developing a better model form or in better defining our parameters. Figure 5 demonstrates such a case where the probability of satisfying the error tolerance is 0%. As the uncertain parameter space expands, some model instances may begin to satisfy the error tolerance leading to a counter-intuitive increase in probability of satisfying with increasing parameter uncertainty. Such behavior can point to the imperfections in either the model form or the uncertainty bounds on the parameter values.

Parametric uncertainties can usually be reduced by additional data collection or

further analysis. What is necessary however is to first inquire as to whether a reduction in parameter uncertainty will indeed improve the usefulness of the model (i.e. in our definition, the probability of satisfying a prescribed error tolerance). Hence, in our evaluation, we do not require that a single uncertainty bound be specified for an input parameter. Instead, an array of differing levels of uncertainty can be studied to observe how a model's probability of satisfying the fidelity tolerance changes with varying levels of parametric uncertainty (see Figure 4). Of course, a higher probability of satisfying relates to an increase in the worthiness of a model for its intended use. Such a trade-off analysis allows us to estimate the potential impact of efforts aimed at reducing uncertainty.

Up to now, we have assumed that a perfect, normative definition for an error tolerance is known. The reality is such a tolerance may not be easy to determine and the decision-maker may first need to decide how to decide (how good is good enough?). The point the decision-maker agrees on a maximum allowable error tolerance however, he/she immediately becomes blind to the differences in the behaviors of alternative models for error tolerances less than that predefined tolerance. Note that in our context setting a maximum tolerance means that the prediction error is expected to be at least a certain amount or less. What would it mean then if a model demonstrates the largest robustness for error tolerance of (say) 10%, but it is the least robust for less error tolerance of (say) 9%? See for instance 6, where Models 1 and 2 appear to be identical as these two models provide the same satisfying boundary for the given error tolerance, however the robustness of Model 1 is superior to Model 2 for error levels less than the maximum tolerance. One possible remedy is evaluating the satisfying boundary for varying levels of error tolerance. One would expect the satisfying boundary to monotonically increase in size as the error tolerance becomes less and less stringent (encompassing more and more input parameter sets) as shown
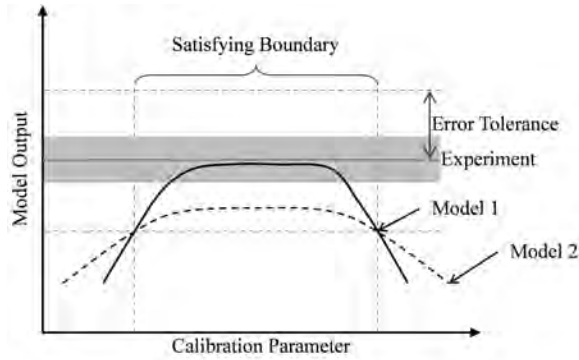
Figure 6: Inability to distinguish between multiple models within the same satisfying boundary. The gray band represents experimental uncertainty.
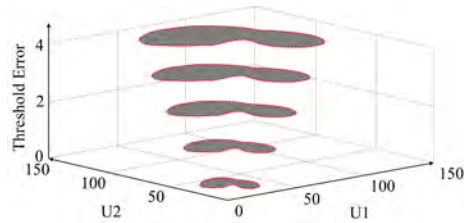
Figure 7: A schematic representation of the satisfying boundary monotonically increasing with increasing error tolerance in the predictions (i.e. decreasing fidelity)

by nested sets in Figure 7. What we propose here is then exploring the trade-offs between model's predictive fidelity and the ill-effects of parameter uncertainty by noting changes in the model's probability of satisfactory prediction within error tolerance.

Note that in Figure 6, the gray band represents the bounded experimental uncertainty, which may originate from a variety of sources including: measurement noise, unit-to-unit variability, operator-to-operator variability, etc. This experimental uncertainty can be reflected in the analysis by defining the error tolerance with respect to these uncertainty bounds (instead of the mean) or by making the error tolerance itself uncertain. The latter option will be discussed later in Section 3.6.3.

3.3 Towards the Derivation of Satisfying Boundary

The satisfying boundary can be constructed by sampling the uncertainty interval and generating hypervolumes (in n-dimensional input space) encompassing instances that satisfy the error tolerance. For instance, [201] implemented Monte Carlo sampling to approximate the volume of the satisfying boundary. Such a method is feasible only in cases where the model is fast-running and the number of uncertain inputs is rather small, otherwise the sampling task quickly becomes prohibitive (i.e. curse of dimensionality). A number of other algorithms have been previously developed for calculating the hypervolume, see for instance [202], [203] and [204]. In our study, in contrast with the previous work, we focus on defining the boundary itself, not the volume. Once the boundary is defined, then low-cost sampling techniques can be adapted to determine the what portion of the parameter space falls within the satisfying boundary. In this section, we will discuss an optimization-based algorithm we have developed to define the satisfying boundary.

Let us now consider a model M which is proper continuous with n uncertain input parameters, $U_i, (i = 1, 2, ..., n)$, defining an n-dimensional parameter space, where

$$y_p = M(U_i) \quad for \, i = 1, 2, ...n \tag{1}$$

where y_p is the model output vector and U_i, are the model input parameters. Here, the analyst is assumed to have prior knowledge regarding the uncertainty bounds for U_i; however, their distributions are unknown. The model error can be defined for instance as the normalized deviation of these model predictions from experimental measurements as given in Equation 2:

$$R = \frac{||y_o - y_p||}{y_o} \tag{2}$$

where R represents the norm of the error between the model predictions y_p and the experimental measurement y_o. In Equation 2, $||.||$ indicates a suitable metric (such as a Euclidean distance, i.e. absolute geometric distance between two points; Mahalanobis distance, i.e. weighted distance between a point and a population that considers the correlations; Bhattacharyya distance, i.e. weighted distance between two populations that also considers the correlations). See [205] for a discussion on these metrics in the context of model validation.

Assuming that a n-dimensional parameter space contains a solution that can identically reproduce the results of an experimental measurement; i.e., $R_t = 0$, where R_t represents the predefined fidelity threshold, it would be possible to find optimal solution(s) U_i that satisfies zero error tolerance. If such a solution(s) does not exist, then there will be solution(s) that would yield the best fidelity (i.e., lowest R value) to experiments. Let us evaluate the functional form of Equation 2 for a model with a two-dimensional parameter domain U_i corresponding to the input parameters U_1 and U_2 given by the following generalized model where the model error R is a function of the parameters:

$$R = f(U_i) \tag{3}$$

This representative functional form of Equation 3 with two uncertain parameters is illustrated in Figure 8. The goal is to find all coordinate pairs of U_1 and U_2 in this three-dimensional domain that give produce error within acceptable error tolerance R_t. Under the given error tolerance, the worst case input parameters U_{i_c} satisfy the following conditions:

$$f(U_{1_c}, U_{2_c}) - R_t \leq \varepsilon \tag{4}$$
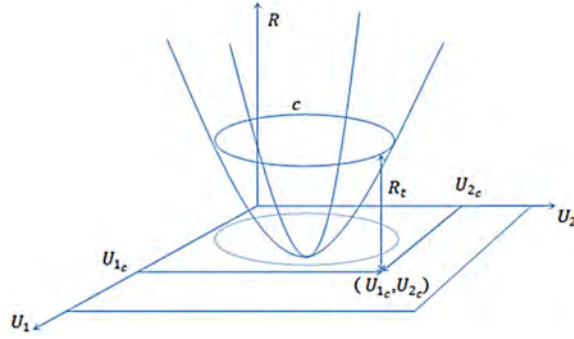
Figure 8: Depiction of a minimization function in two-dimensional parameter space

where ε is tolerance used as the optimization stopping criteria, usually a small value e.g. 10^{-7}.

The set of these input parameter U_{i_c} in the entire uncertainty interval form the satisfying boundary for a given error tolerance. Therefore, by defining an objective function in the following form and minimizing the z value, the points on the satisfying boundary can be sought.

$$\min \ z = \min |f(U_{1_c}, U_{2_c}) - R_t| \tag{5}$$

Most optimization approaches require an initial, starting point for the algorithm. Here, we used the center of the uncertainty interval of the input parameters as the initial starting point. Subsequent points are chosen via a suitable optimization algorithm that searches for an optimal point around the previously selected point. The search is bounded within the specified uncertainty intervals on the input parameters. The number of such points that define the satisfying boundary is decided based on the computational demand of the model. A flow chart describing the algorithm's step-wise process is shown in Figure 9.
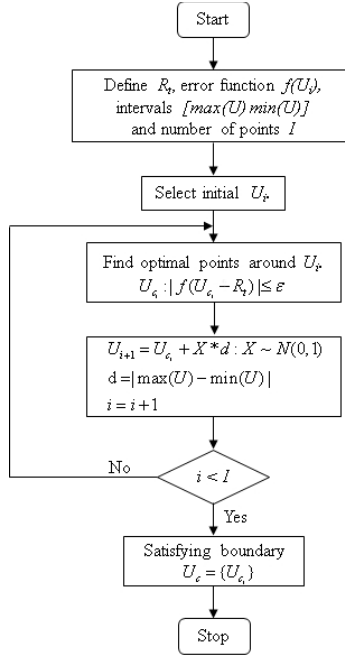
Figure 9: Flowchart of optimization algorithm used to define the failure surface of a two-dimensional uncertain parameter domain

3.4 Proof-of-concept Demonstration: Steel Moment Resisting Frame

3.4.1 Description of Frame Structure

The concepts introduced in the previous chapters are demonstrated on a 2-D steel frame shown in Figure 10. The frame is constructed with vertical columns that rest on fixed supports, while the beams are semi-rigidly connected to the columns at both levels. In steel frame structures, the connection stiffness values are typically highly uncertain due to the natural variability of material properties and geometries as well as the construction practices [206, 207]. Hence, in our proof-of-concept example, the connections stiffness at the top of the first story columns are treated as uncertain parameters. These connections are represented with linear rotational springs with uncertain stiffness constants. All members of the portal frame are assigned uniform

37

Property Description	Beams & Columns
All Member Lengths (in)	72
Cross-Sectional Area (in^2)	4.44
Moment of Inertia (in^4)	48.0
Young's Modulus (ksi)	29000

Table 1: Input values for the portal frame
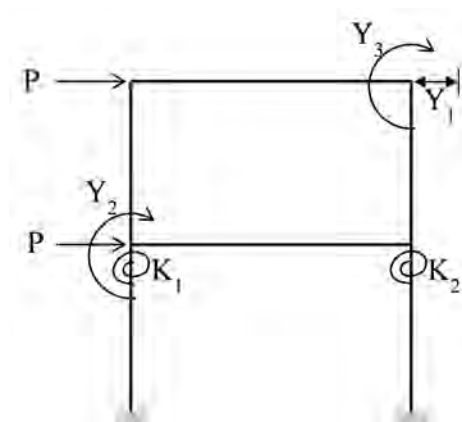
Figure 10: Single-bay, two-story portal frame with rotational springs at the top of the first story columns

dimensions with the geometric data and material properties provided in Table 1. Static, horizontal loads are applied to the portal frame as shown and the members are oriented to bend about their strong axes.

3.4.2 Synthetic Experiments and Satisfying boundary

There is almost always more than one way to develop the mathematical representation for an engineering or natural phenomena. A variety of simplifying assumptions may be established or idealizations may take place leading to multiple competing model forms. In this section, we demonstrate on a controlled academic example how the probability of satisfying the error tolerance can be used to compare three distinct model forms with varying levels of model imperfectness (i.e. prediction bias).

Experimental data describing the frame's translation and rotation response at

each connection while subjected to the loading conditions shown in Figure 10 is synthesized using the so-called *exact* model built using the Timoshenko beam theory [208]. This exact model not only accurately accounts for the effects of axial, shear, and flexural deformations but also uses the so-called true values of K_1 and K_2 of $10\,kip - in/rad$ (Table 1). The corresponding exact Y_1 and Y_2 are $0.095\,in$ and $0.54 \times 10^{-3}\,rad$ respectively for an applied load $P = 1\,kip$.

An example satisfying boundary is shown in Figure 11 for an error tolerance of 2.5% in the output Y_1. Using the optimization algorithm described in Section 3.3 with 200 points, the *entire* satisfying boundary is identified (note that in Figure 11 satisfying boundary goes beyond what is shown in the figure). If a more complex satisfying boundary is of concern, the number of points evaluated during optimization may be gradually increased until a converged definition for the boundary is obtained. Since the frame model is computationally cheap, sampling is also a plausible option for this example. In Figure 11, $40,000$ instances of (K_1, K_2) are sampled within their uncertainty bounds, which in this case is set to be between 5 and $15\,kip - in/rad$. Contours in the input space that join extremities of the sampled point clouds agree well with the satisfying boundary obtained using the previously discussed optimization algorithm.

3.4.3 Competing Model Forms

Alongside the exact model, two inexact (biased) model forms are built: one that underestimates and one that overestimates the shear area by 25% within the Timoshenko beam stiffness formulation. Hence, the two inexact models will inaccurately account for the shear deformations, while all three models will contain uncertainty as to which values of K_1 and K_2 are appropriate for the analysis. These inaccurate and imprecise models will thus result in unavoidable disagreements between predictions
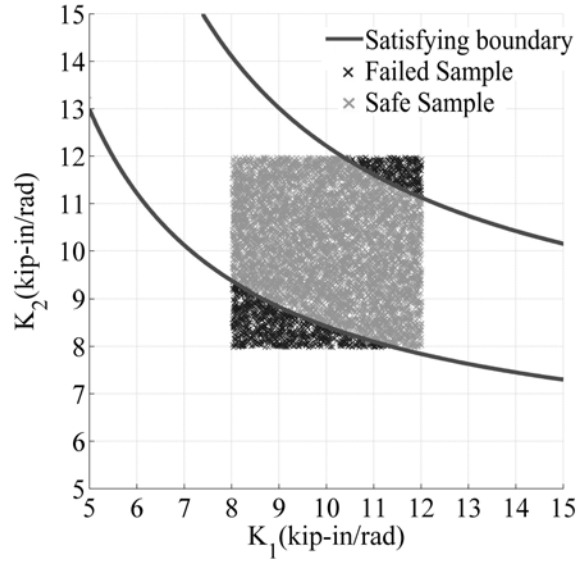
Figure 11: The satisfying boundary for Parameter Y_1 in the input parameter space for an error tolerance of 2.5%.

and experiments offering a decision maker three alternative options.

3.5 Satisfying Boundary for Decision-making: Steel Moment Resisting Frame

3.5.1 Exact Model with Uncertain Input Parameters

Here, the bounds of the parameter space for K_1 and K_2 are set to be between 5 and $15\, kip - in/rad$. For various combinations of K_1 and K_2 within these bounds, the model predictions are compared to the synthetic experimental data to calculate the percentage prediction error. Two outputs of the frame are selected, the rotation at the first story and the translation at the top story (marked as Y_1 and Y_2, respectively in Figure 10). The corresponding prediction errors, R_1 and R_2 are the percentage differences with respect to the exact model. Figure 12 illustrates the relationship between the error in the model output (i.e. lack of fidelity) and the two uncertain
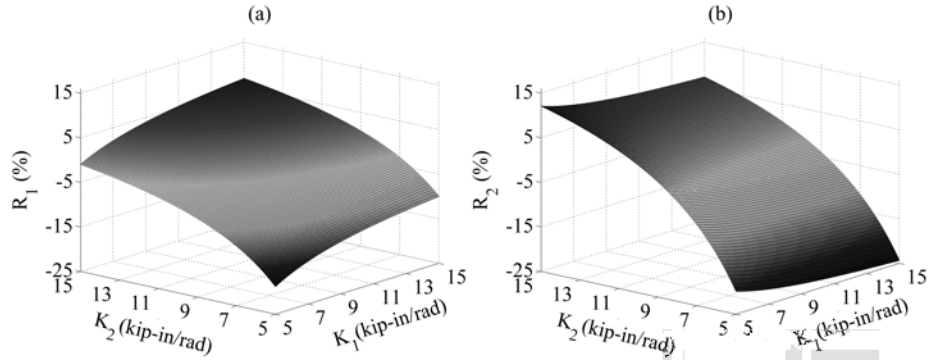
Figure 12: Three-dimensional representation of prediction errors R_1 and R_2 in the exact model.

parameters.

Subsequently, satisfying boundaries are generated for varying error tolerances, R_t, shown in Figure 13. R_t is varied from 0 to 5% prediction error in steps of 0.5%. In Figure 13, each contour corresponds to an error tolerance level R_t such that all instances of K_1 and K_2 that lie within the contour satisfy that error tolerance. As expected of a continuous system, the satisfying boundaries are nested with their size increasing as error tolerance increases. The model form used in the development of this figure was 'exact', which is why the true parameter values are encompassed within the satisfying boundaries.

3.5.2 Inexact Models with Uncertain Input Parameters

The two inaccurate finite element models studied herein underestimate and overestimate the shear area of the beam and column elements by 25% (i.e., 75% and 125% shear area, respectively). This intentional error is meant to mimic a possible modeling mistake resulting in biased model predictions. The satisfying boundaries for the two inexact models are shown in Figures 14 and 15.

As seen in Figure 14, the underestimation of shear deformation causes the satisfying boundaries to shift downwards, which is evident when compared to the satisfying

41
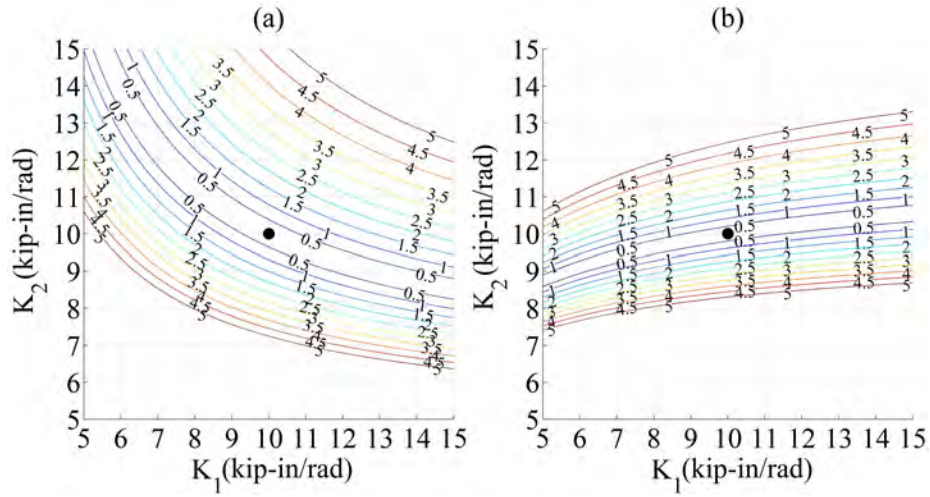
Figure 13: Nested sets of satisfying boundaries for increasing levels of error tolerance for the exact frame model for (a) output Y_1 and (b) Y_2.The black dot represents the location of the "true" parameter values (those that were used while generating synthetic experiments).

Figure 14: Nested sets of satisfying boundaries for increasing levels of error tolerance for the biased frame model (25% lower shear area) for (a) output Y_1 and (b) Y_2. The black dot represents the location of the "true" parameter values (those that were used while generating synthetic experiments).

Figure 15: Nested sets of satisfying boundaries for increasing levels of error tolerance for the biased frame model (25% higher shear area) for (a) output Y_1 and (b) Y_2. The black dot represents the location of the "true" parameter values (those that were used while generating synthetic experiments).

boundaries obtained from the unbiased model shown earlier in Figure 13. An important observation we can garner from Figure 13 is that the true parameter values represented by the black dot ($K_1 = K_2 = 10\,kip-in/rad$) in Figure 14 are no longer encompassed by the initial (smallest) satisfying boundary. This is the result of the inherent bias in the predictions of these two inexact models. Figure 15 shows the satisfying boundaries for the frame model with the shear area overestimated by 25% and a bias in the opposite direction.

3.5.3   Utilizing the Satisfying Boundaries

The satisfying boundaries for the three competing models (one exact and two inexact) discussed in the previous section are used herein to evaluate the probability of satisfying predefined error tolerances within the uncertain parameter space. In this evaluation, bounded uncertainty is allowed to gradually increase from 0.5 to $5\,kip-in/rad$ in steps of $0.5\,kip-in/rad$ as show in Figure 12. An uncertainty of $5\,kip-in/rad$
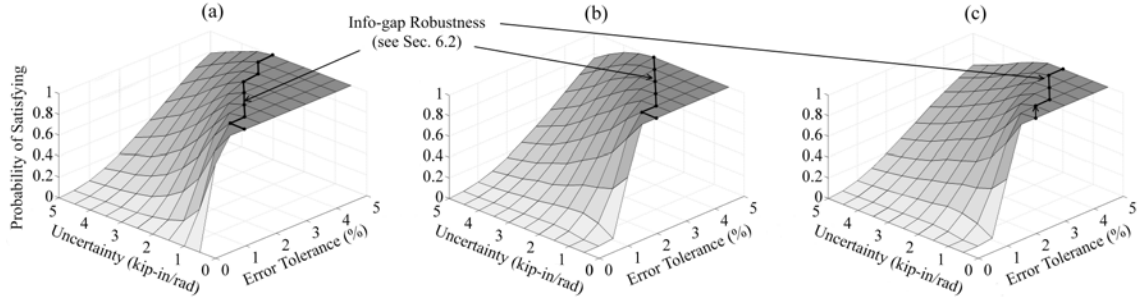
Figure 16: Three-dimensional plot showing trade-off between probability of satisfying, error tolerance and parametric uncertainty for the (a) accurate model, (b) inaccurate model with 25% underestimated shear area and (b) inaccurate model with 25% over-estimated shear area.

means that the parameter value can vary between 7.5 and $12.5\,kip - in/rad$. This evaluation is also repeated for increasing levels of error tolerance from 0 to 5%, in steps of 0.5%. Figure 16 displays the relationship between the varying levels of error tolerance in model predictions, the parameter uncertainty and the subsequent probability that the model satisfies this predefined error tolerance. Since two outputs, namely the translation at the top story (Y_1) and the rotation at the first story (Y_2) of the steel frame, are considered, the joint probability of satisfying the error tolerance in both outputs is calculated (see Figure 16).

Figure 16 can be used as a diagnostic tool to identify the usefulness of a computer model. It can be observed from Figure 16 that as error tolerance increases so does the probability of satisfying the error tolerance. The rate of increase depends on the level of bounded uncertainty. When the uncertainty in the parameters is low, the probability is observed to increase at a more rapid rate than when the uncertainty in the parameters is high. The light region in Figure 16 represents the situation where the model is not suitable for its intended use (as defined by the error tolerance) given the available knowledge (as defined by the parametric uncertainty). On the other hand, the dark region in Figure 16 represents the situation where the model is a good
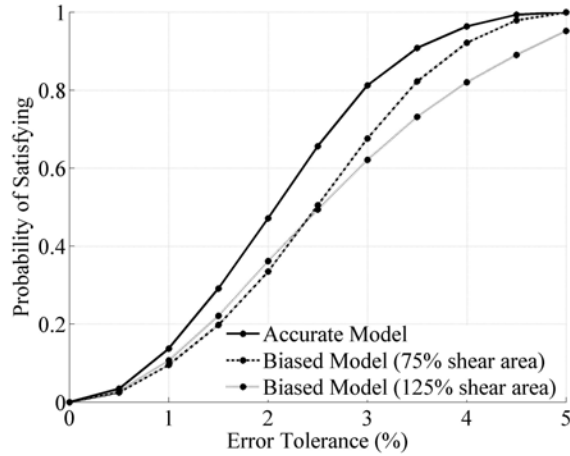
Figure 17: Probability of Satisfying as a function of Error Tolerance for a $3\,kip-in/rad$ uncertainty in K_1 and K_2.

fit for its intended use. This region is obtained when the experimental uncertainty approaches lower values and when the error tolerance approaches higher values. The model with the exact form (Figure16a) displays larger dark region compared to the two inexact models (Figures 16b and c).

Figure 17 depicts the relationship between the probability of satisfying the error tolerance and the error tolerance itself for 30% uncertainty in K_1 and K_2. As can be seen in Figure 17, for an error tolerance of 0%, the corresponding probability of satisfying this tolerance is 0%, meaning that no model form can accommodate the given level of uncertainty and satisfy the required error tolerance. Only by increasing the error tolerance does the probability of satisfying increases. It can be observed in Figure 17 that the exact model consistently yields a higher probability of satisfying the error tolerance compared to the two inexact models[4]. Furthermore, the exact model's probability of satisfying the error tolerance increases more rapidly with error tolerance (higher slope) than the two imperfect models. Although Figure 17 demonstrates this observation for a constant level of uncertainty, this finding is noted to be valid

---

[4]This is of course because our uncertainty bounds for parameter values were centered around the so-called true values.
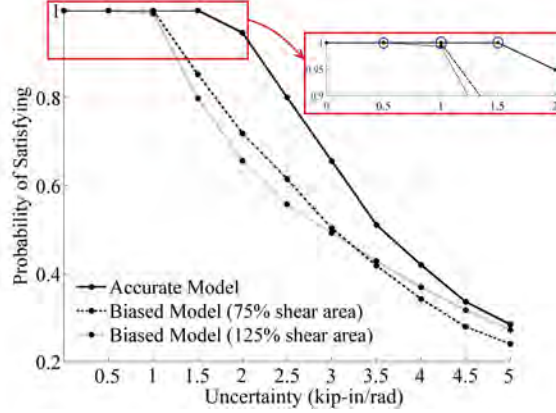
Figure 18: Probability of Satisfying as a function of parameter uncertainty for a constant error tolerance ($R_t = 3\%$).

throughout the entire parameter space evaluated herein.

Figure 18 plots the probability of satisfying the error tolerance of 3% as a function of uncertainty in the input parameters. This plot allows the model developer to observe a potential improvement that can be gained in the probability of satisfying the desired error tolerance by reducing the uncertainty in the input parameters. For instance, if the developer of the exact model wants to ensure at least 90% probability of satisfying the 3% error tolerance, then resources must be allocated to ensure that the uncertainty in the input parameters is lower than $2\,kip - in/rad$. Figure 18 also shows that for uncertainty levels of $0.5\,kip - in/rad$, all models yield predictions that are 100% within the error tolerance. Hence, from this figure, we can deduce that allocating resources for reducing uncertainty below $0.5\,kip - in/rad$ is not justifiable. Increased levels of parameter uncertainty however lead to a reduction in the probability of satisfying, as expected, during which the role of bias once again becomes important. For very high levels of parameter uncertainty, all three models converge to unacceptably low probabilities of satisfying the error tolerance. As seen, Figure 18, similar to Figure 17, can be used as a comparative tool and aid in model

46
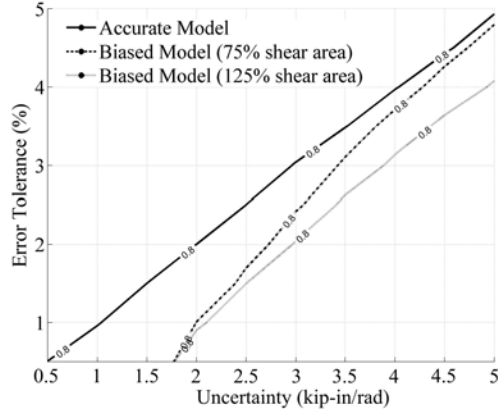
Figure 19: Prediction error as a function of parameter uncertainty for a constant Probability of Satisfying ($P_s = 80\%$).

selection. For instance, a decision maker may establish a minimum probability of satisfying requirement and subsequently evaluate which model performs best given varying degrees of parameter uncertainty.

Alternatively, one can evaluate the relationship between the fidelity of model predictions and parameter uncertainty for a given probability of satisfying (shown for 80% in Figure 19). The two inexact models are inadmissible when the parameter uncertainty is less than $1.8\,kip - in/rad$. This can be explained by the fact that the biased model's satisfying boundaries are offset (recall Figures 14 and 15) resulting in the parameter spaces corresponding to low uncertainty falling entirely outside these satisfying boundaries. This concept, demonstrated earlier in Figure 5, supplies a means for diagnosing fundamental flaws in either our model's form or the values associated with the parameters of these model forms.

3.6 Model Selection Criteria based on Satisfying Boundary

The concept of satisfying boundaries readily presents other useful model selection criteria, including: the optimal deterministic model, info-gap robustness, model distin-

guishability, and the value of information. In this section, we will discuss other, lower dimensional model selection criteria that can be deduced from the three-dimensional plots presented in Section 3.5.

3.6.1 Deterministically optimized model

The special case of $R_t = 0\%$ corresponds to the optimal deterministic design. Preferring one model over another based only on its performance at a point is generally not recommended. Figure 20 shows the satisfying boundaries for varying error tolerances specified on both outputs Y_1 and Y_2 for the biased frame model (25% lower shear area). In this figure, the star represents the deterministic optimal parameter values which differ from the supposed true parameter values used while generating the synthetic experiments. This difference is due to the fact that the deterministic optimal parameter values compensate for the model form error, masking the model's deficiency and making it appear to have good agreement with experiments.

3.6.2 Info-Gap Robustness analysis

Info-gap decision theory [64] provides a framework for investigating the impact of epistemic uncertainty in model parameters on the performance by quantifying the maximum level of uncertainty that can be tolerated while still ensuring a critical level of performance. Info-gap robustness can be evaluated based on the definition of a system model, an info-gap model of uncertainty, and a system performance:

$$\hat{\alpha} = \max \left\{ \alpha \quad : \quad \max_{U \in \Upsilon(U_0, \alpha)} R(U) \leq R_t \right\} \tag{6}$$

where α is the horizon of uncertainty, U is the vector of uncertain parameters, $R(U)$ the scalar measure of performance, and $\Upsilon(U_o, \alpha)$ the info-gap uncertainty model cen-
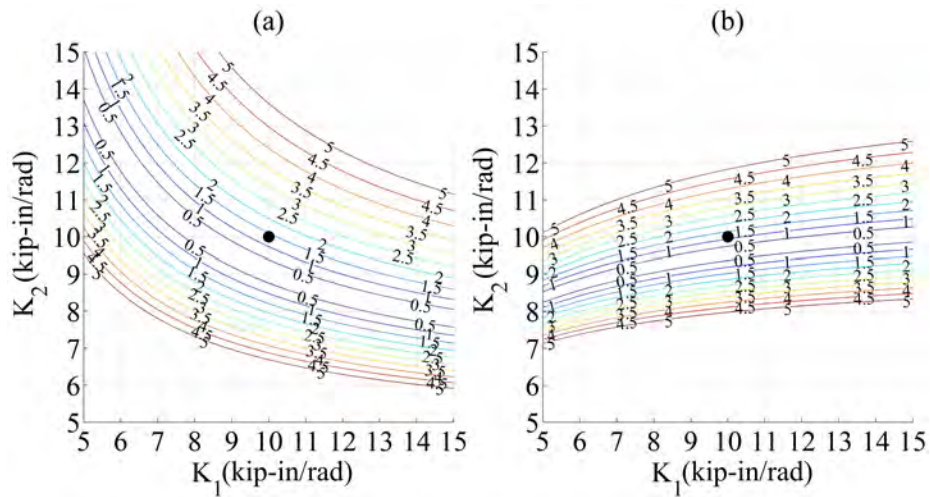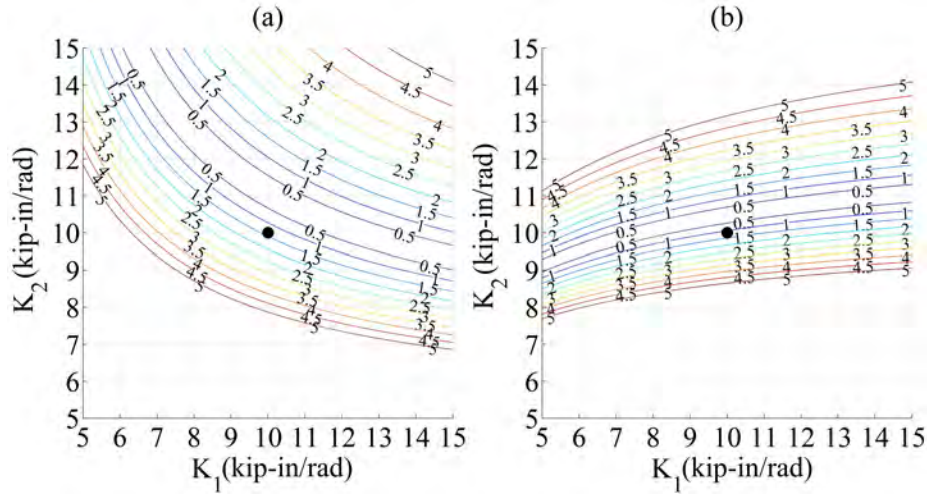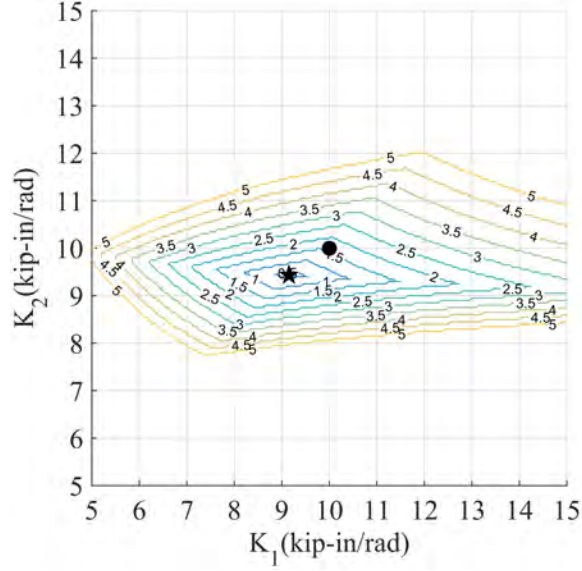
Figure 20: Nested sets of satisfying boundaries for increasing levels of error tolerance for the biased frame model (25% lower shear area). The black dot represents the location of the exact parameter values while the star represents the deterministic optimal parameters.

tered about the nominal design U_0. An example of an envelope bound model for $\Upsilon(U_0, \alpha)$ is:

$$\Upsilon(U, \alpha) = \left\{ U \quad : \quad \frac{\|U - U_0\|}{\|U_0\|} \leq \alpha \right\}, \quad \alpha \geq 0 \tag{7}$$

where α represents the fractional error in the uncertain parameters, representing for instance the compensating effects between the parameter values and various sources of errors (as discussed in Section 3.6.1). Here, it is important to note that Equation 7 requires the definition of a nominal value. Info-gap robustness, $\hat{\alpha}$ is then the maximum allowable α that satisfies a predefined error threshold, R_t.

The robustness, very similar to the way it is introduced in Info-gap decision theory, can also be defined using the satisfying boundaries. For this, one needs to evaluate the largest expansion in the predefined uncertainty bounds for which the probability
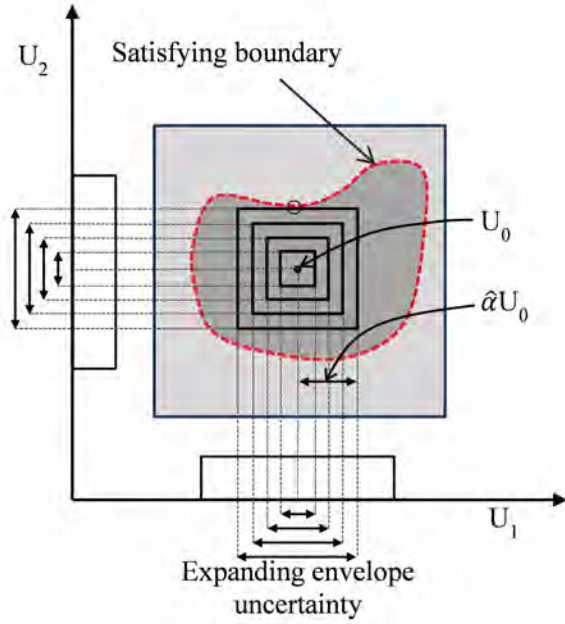
Figure 21: Conceptual figure showing the info-gap robustness $\hat{\alpha}$ with respect to the satisfying boundary in the input space.

of satisfying remains $P_s = 1$. This can be seen in Figure 16, where the info-gap robustness are highlighted for different error tolerance levels. Also recall Figure 18 where the maximum uncertainty (X-axis) corresponding to $P_s = 1$ reflects the info-gap robustness of the three competing models. For an error tolerance of 3%, the info-gap robustness for the accurate model and the two biased models is 1.5, 1 and 0.5 respectively. Schematically speaking, the info-gap robustness for an envelope bound uncertainty model (Equation 7) is the half of the edge-length of the largest the bounded uncertainty envelop that one can fit within the satisfying boundary as conceptualized for a 2-parameter model in Figure 21.

3.6.3 Model distinguishability

Model distinguishability, a fundamental characteristic of input-output spaces, quantifies the extent to which models can be ranked based on their fidelity-to-data alone

given the presence of measurement errors. High model distinguishability indicates that model behaviors are sufficiently distinct from one another and that regions of fidelity-equivalent solutions are relatively small. Low distinguishability indicates that there are large regions in the parameter space with nearly equivalent output errors. This means that fidelity-to-data alone is not sufficient to select a model from a set of indistinguishable models (recall the phenomena of non-uniqueness discussed earlier).

Model distinguishability presents a means for incorporating the experimental uncertainty into the evaluation. If α_e is the measurement noise, the indistinguishable models are a set of all models that satisfy the specified error tolerance R_t within a tolerance of α_e:

$$U_{id}(R_t) = \{U \quad : \quad ||R(U) - R_t|| \leq \alpha_e\} \tag{8}$$

Figure 22 illustrates the notion of model distinguishability based on the nested sets of satisfying boundaries for the biased frame model (25% lower shear area) for the mean output error $R = \frac{1}{2}(R_1 + R_2)$. The colored zones correspond to sets of indistinguishable models for measurement noise of 0.5% and output errors of 0.5%, 1.5%, 2.5%,... etc. Models with these zones are fidelity-equivalent and can not otherwise be ranked without additional information, for example parameter constraints or new experiments.

3.6.4 Value of added information

In general, performance requirements are specified based on more than one experimental outcomes, for example: static tests under different load configurations, subsets of eigensolutions from modal tests, and etc. Having multiple performance requirements can prove both favorable (e.g. reinforcing the uniqueness of the solution and
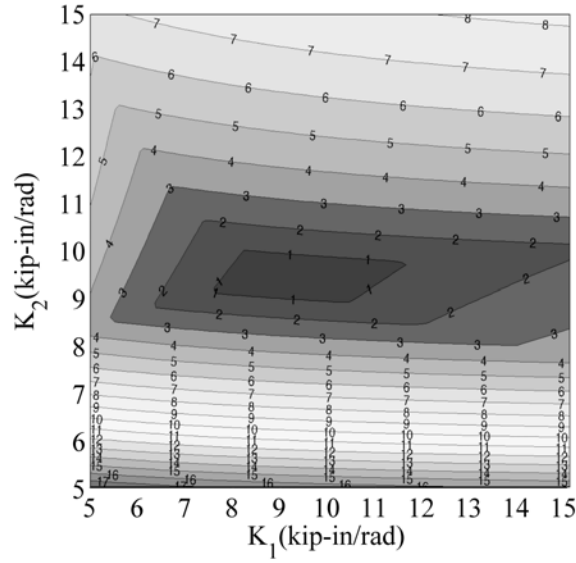
Figure 22: Model distinguishability for the biased frame model (25% lower shear area) assuming measurement noise level of 1% and the mean output error $R = \frac{1}{2}(R_1 + R_2)$ 0.5%, 1.5%, 2.5%, etc.

increasing model distinguishability) and detrimental (creation of multiple minima and reduction of robustness). Therefore, investigating the changes in the satisfying boundary resulting from the inclusion or exclusion of performance requirements provides a useful tool for quantifying the value of information added by including new experiments.

Figure 23 shows how the *global* satisfying boundary, the intersection of the individual satisfying boundaries of each output, is affected as new performance requirements are added. In Figure 23a, performance requirement in terms of error tolerance, $R_t = 2.5\%$, is specified only on the output Y_1 (refer Figure 10). In Figure 23b and Figure 23c, the same performance requirement is added on outputs Y_2 and Y_3, leading to lesser instances of (K_1, K_2) being satisfied, effectively shrinking the satisfying boundary. In this particular example, by adding performance requirements reinforces the uniqueness of the solution, however, there might very well be cases, where multiple satisfying boundaries fail to intersect revealing an inherent deficiency in the model's
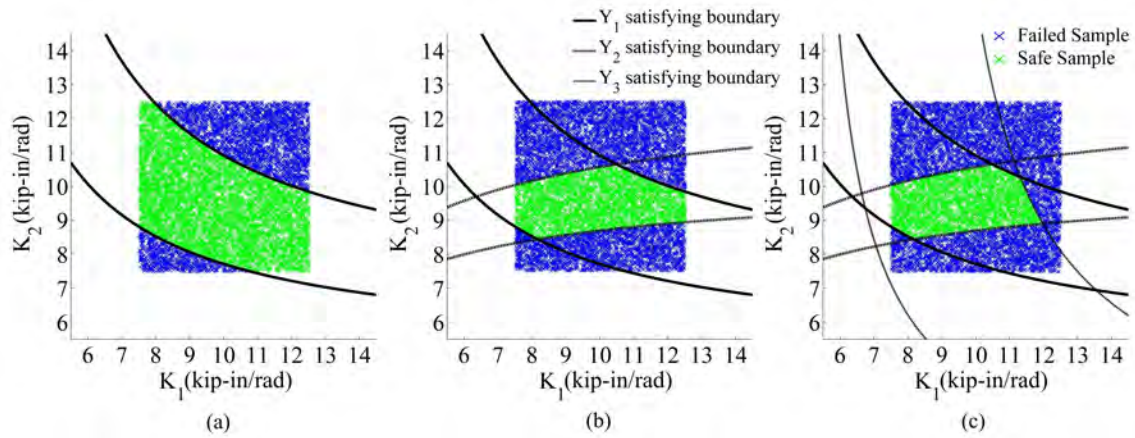
Figure 23: Satisfying boundaries ($R_t = 2.5\%$) of three model outputs and their intersection which is the safe region.

predictive ability.

3.7 Conclusion

In numerical modeling, uncertainties arise due to imprecisely-known input parameter values just as biases arise from our imperfect understanding of the underlying physics. This chapter has presented a method to evaluate the usefulness of alternative model forms in answering the questions asked of them given the availability of information regarding their parameter values. This evaluation is completed considering three criteria. The first criterion, which relates to a model's intended use, involves the desired fidelity of model predictions to experimental observation. The second criterion, which relates to the availability of information, concerns how well a model can maintain these desired fidelity levels given uncertainty in its input parameters. The last criterion combines the first two criteria by assessing a model's probability of satisfying a predefined error tolerance requirement.

In this chapter, we introduced the concept of a satisfying boundary, as the boundary that encompasses all admissible parameter sets. Focusing our attention on uni-

formly continuous, proper functions, we calculated compact satisfying boundaries and observed the trade-off between the error tolerance in the model predictions and the probability of achieving predictions that indeed satisfy this allowable error for various levels of parameter uncertainty. In this study, we evaluated the case where the uncertain parameters are enveloped within bounds. Representation of bounded uncertainty in nested sets allowed us to evaluate the effect of uncertainty in input parameters on the satisfying boundary as well as probability of success, visually depicting the sensitivity of the results to changes in the amount of information available regarding input parameters. However note that if one has more information (such as probabilistic information) about the parameters, nothing prevents him/her from incorporating this information while determining the probability of satisfying.

Here, the individual tasked with validating the model must establish certain adequacy criteria regarding the tolerable error in model predictions or the desired probability of ensuring that the model satisfies this tolerable error. For a given level of uncertainty, only one of these two criteria need be known or defined, from which the third can then be determined. Hence, knowledge of the trade-offs between these two criteria can afford a decision maker useful insight in selecting the most useful or appropriate values based upon the model's intended application. Additional model selection criteria closely related to the notion of a satisfying boundary have been presented to enhance the visibility of important characteristics of the design space, including the deterministic optimal solution, the robust optimal solution, model distinguishability, and the value of added experimental outcomes.

A level of awareness of model's weaknesses is necessary for the approached presented herein as one still needs to select the uncertain parameters to be included in the analysis, the response feature of interest to used to evaluate fidelity as well as the metric (mathematical means) for calculating error. As every aspect of model devel-

opment, the selection of features must depend on and closely relate to the purpose for which the model is built. This issue which requires careful discussion has been left out of the scope of this chapter, but must nonetheless be an integral part of the application of the proposed approach.

As discussed earlier, the discussion in this chapter is limited to uniformly continuous proper functions to ensure compactness of the satisfying boundary. Although satisfying this requirement within the parameter space is sufficient for our proposed approach to be applicable, relaxing this assumption may result in discontinuous or non-compact satisfying boundaries. Therefore, future work must explore this occurrence in hopes of determining its implications and how model validation should occur in these instances.

Also note that our definition of 'usefulness' as the ability to predict available experiments is naive in the sense that models are likely to be build to predict at untested settings. Therefore, an expansion of this study to investigate the ability of the model forms selected through this method in predicting at untested settings within the domain is in order.

4   MODELING AND SIMULATION OF FORT SUMTER

4.1   Introduction

Differential settlements occur when soil conditions below the foundation are inhomogeneous or the load distribution at the soil-structure interface is non-uniform. Anthropogenic activities in the structure's vicinity, such as tunneling and vibration from traffic and construction activity, are also causes for differential settlement. The subsequent angular distortions and tilting of the superstructure disturbs the structure's intended geometry, resulting in the development of tensile stresses. These tensile stresses can lead to cracking if the magnitude of the tensile stress exceeds the rather small tensile capacity of masonry. Thus, a relatively small magnitude of settlement can lead to cracking of the masonry assembly. These cracks, if uncontrolled, can ultimately lead to sudden hinge formations due to the brittle nature of historic unreinforced masonry, which in turn can result in structural instability. Little is known however, about the early warning signs of settlement induced damage to historic masonry structures, which typically are a complex system of arches, vaults, piers and walls. If such warning signs are known, infrastructure managers could identify when support settlement are the cause of structural distress and take precautionary actions to prevent potential structural instability.

For many existing structures, the settlement magnitudes and types that form hinges in the structure and lead to cracking are difficult to determine through analytical, closed-form-solutions, given the structure's complex geometric configuration and material behavior. Empirical approaches published in literature regarding the determination of critical settlements have many limitations such as isolation of

56

settlement-induced damage from other sources and lack of exhaustive, quantitative analyses [209–212]. On the other hand, numerical simulations are identified as effective tools for analyzing the behavior of masonry structures under any settlement severity and configuration [76, 77, 213, 214]. The major challenge in developing numerical models for historic masonry is the assignment of accurate input parameters, such as geometry, material properties and boundary conditions [154, 215]. This challenge is further magnified in the case of historic monuments that have irregular geometric features with permanent deformations, high spatial variability of material properties, and uncertain interactions between adjacent components and between the structure and ground [93, 154, 216].

To ensure model predictions are representative of the actual structural behavior, on-site data must be incorporated to mitigate potential uncertainties and errors in model input parameters [170, 217, 218]. Accordingly, using a numerical approach integrated with experiments, this chapter presents an evaluation of the settlement-induced damage to an unreinforced masonry vaulted casemate of Fort Sumter under the incremental development of a wide range of possible settlement scenarios. This chapter is organized as follows. Section 4.2 provides a brief history and reviews the structural characteristics of Fort Sumter while Section 4.3 details the field investigations that support the development of the numerical models. The development of the three-dimensional nonlinear FE model of the casemate is discussed in Section 4.4, followed by a discussion on the calibration of the imprecisely known parameters of this model against in-situ vibration measurements in Section 4.5. The model calibrated for maximizing fidelity is tested for robustness using the satisfying boundary approach in Section 4.6. Section 4.7 presents the simulated response of the vaulted casemates for various support settlement while, quantitative and qualitative assessments under the simulated support settlement scenarios are provided in Section 4.8. Summary of

57

the chapter and concluding remarks are provided in Section 4.9.

4.2 Fort Sumter National Monument: History and Structural System

The construction of Fort Sumter began in 1829 with local sand being used to create a two-acre island. Ten thousand tons of granite and over sixty thousand tons of other assorted rocks were used to provide a foundation [219]. By 1860, the pentagonal-shaped fort had five ft. thick, 50 ft. tall brick walls, enclosing a parade ground of approximately an acre (Figure 24). The nearly four million bricks used in the construction of the walls were manufactured locally. The mortar used was a mixture of local sand, cement from New York and limestone from burnt oyster shells [219]. The walls of the fort, except for the gorge wall, are made up of a series of structures called casemates which once held two tiers of arched gunrooms. The perimeter of the fort is encased by a scarp wall, which has gun embrasures on four sides to allow cannons to fire. Typical of third system coastal fortifications, the barrel vaulted casemates, which hold the cannons, are built adjacent to, but, detached from the scarp wall. This construction detail separates the scarp wall and the casemate as independent structural entities and keeps any external damage by cannonballs isolated to the scarp wall [220]. During the Civil War, Fort Sumter was bombarded from virtually all sides and left in a state of "practical demolition" [221] (Figure 25a). After the war, three barbette platforms and 11 lower-tier gunrooms were reconstructed. Originally over 50 ft. tall, the fort's walls have been reduced to one tier of casemates (Figure 25b). In 1948, Fort Sumter was declared a national monument and has since been maintained by the National Park Service.
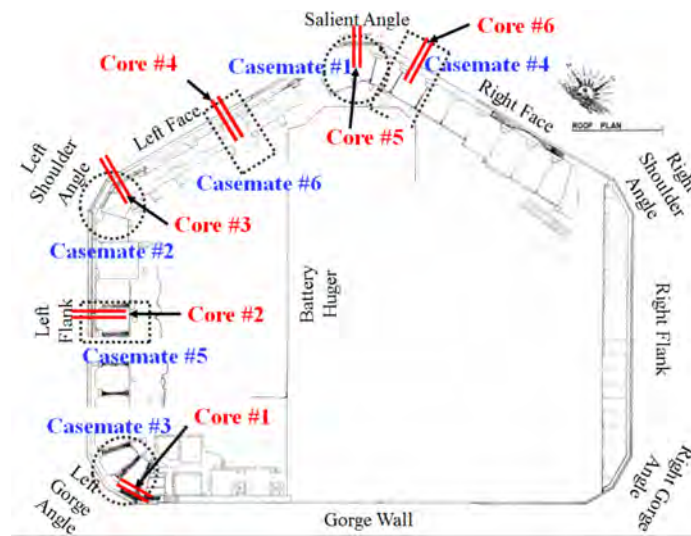
Figure 24: Roof plan marking the six casemates to be modeled and the locations of the core sampling points (plan drawing courtesy of National Park Service).

Figure 25: (a) Photo taken on August, 1863 showing the first breech in Fort Sumter walls (original photograph by G.S. Cook), (b) Photo taken in August, 2011 showing the current condition of Fort Sumter casemates.
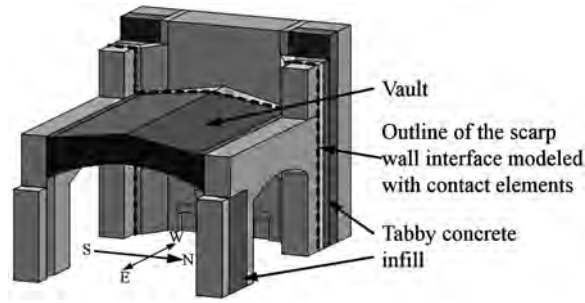
Figure 26: Solid model of the casemate showing the different material assignments and the location of the scarp wall interface modeled with contact elements.

4.3 Site Inspection and Evaluation: Data Collection for Model Development

This section discusses the field inspections of the present condition of Fort Sumter, including (i) physical tests on material samples, (ii) three-dimensional laser scanning of the fort's geometry and (iii) ambient vibration testing of the casemates.

4.3.1 Coring Samples and Material Testing

Although the construction drawings of the fort indicate the fort was originally designed with brick masonry all throughout the walls (see U.S. National Archives, Drawer 66, Sheet 1), on-site evaluations and cored samples reveal a construction of masonry walls with concrete infill (Figure 26). Therefore, the brick walls of Fort Sumter are heterogonous in nature, not only in the use of masonry units and mortar joints, but also in the inner morphology of the structural system with lower strength filler material or cavities. To reflect this heterogeneity, three distinct regions with individual material properties are identified in the numerical model: (i) the masonry walls and piers, (ii) the barrel vault of the casemate and, (iii) the tabby concrete infill in the scarp wall and piers (Figure 26). An independent parameter value is assigned for the vault to reflect the differences in the joint orientation.

60

Figure 27: (a) Block specimen from the remains of the fort; (b) block specimen segmented into smaller samples for testing; (c) Coring of the wall in progress; (d) an intact core sample of tabby concrete infill.

Most masonry mortar used at Fort Sumter is constituted of natural cement (also known as Rosendale cement), lime and sand [222]. Rosendale cement is a binder generally producing lower strength mortar than Portland cement-sand mortars [223]. The concrete infill of the fort can be best described as "tabby concrete"- a concrete-like compound generally composed of quicklime (obtained by burning oyster shells) and aggregate (composed primarily of oyster shells and sand with some brick pieces) [224]. To determine characteristics of brick and mortar used during the construction, a 305×355×152 mm block sample is collected from the site and tested in the laboratory (Figure 27a & b); while the characteristics of the concrete infill are determined from the cored specimens.

Two samples, cut from the block specimen collected on site (Sample A and Sample B as shown in Figure 28), are tested to obtain both compressive and tensile material properties. During compression experiments, sample A is tested for compressive strength in the direction normal to the bed-joint (Figure 28a), while Sample B is tested for compressive strength in the direction parallel to the bed-joint (Figure 28b). The compressive strength of the brick and mortar assembly is determined using 50 mm cube specimens according to ASTM C109/109M -11a. The modulus of elasticity is calculated as the slope of the elastic region of the stress-strain curves as shown in Figure 28c. For both samples, averaged modulus of elasticity of 3.57 GPa and compressive strength of 20.7 MPa are obtained. The mean values for modulus of elasticity are considered as prior information for the calibration of the numerical model against experimentally obtained vibration measurements (discussed later in Section 4.5.2).

Three point flexural tests conducted on samples cut from the block specimen (Figure 29) yield the tensile strength of mortar and brick as 0.65 MPa and 2.37 MPa, respectively. The final tensile strength is calculated as a volumetric average of the mortar joints and brick units and set to 2.07 MPa. Moreover, bulk densities are calculated by cutting the specimen into cylinders and measuring the weight-to-volume ratio. The densities of brick and mortar that are measured as 1490 kg/m^3 and 1670 kg/m^3, respectively. A volumetric average yields a density of 1500 kg/m^3 for the masonry assembly.

Diametral tests on three core samples of tabby concrete, shown in Figure 27d, provide a compressive modulus of elasticity of 530 MPa and average tensile and compressive strength of 0.53 MPa and 6.37 MPa, respectively. The density of the tabby concrete infill is measured from the core samples as 1600 kg/m^3. The material properties used in the FE model are summarized in Table 2. Note that values of the
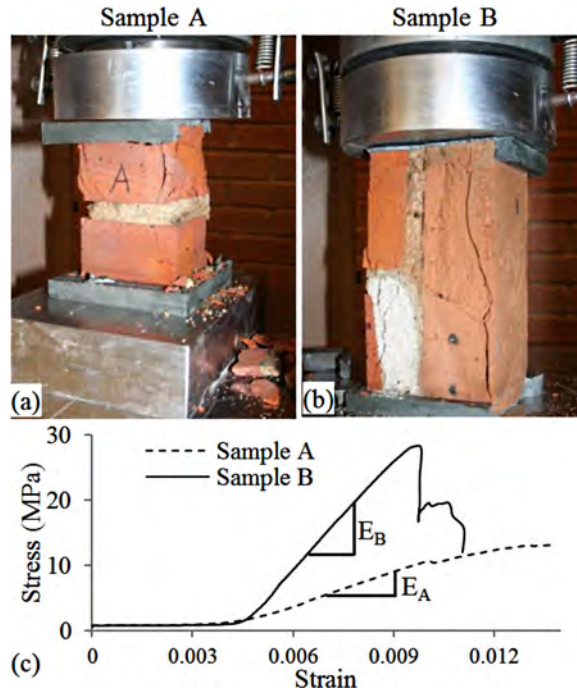
Figure 28: (a) Sample A crushed in the compression test; (b) Sample B crushed in the compression test; (c) Stress strain curves for Sample A and Sample B from the compression test. The slope of the elastic region is taken as the elastic modulus.
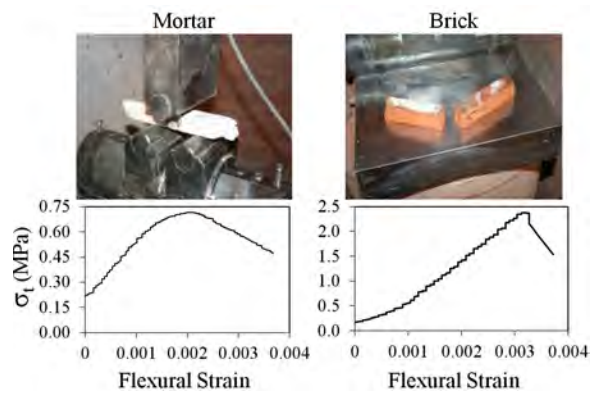
Figure 29: Samples cut from the block specimen for 3-point flexural test and corresponding stress-strain curves.

modulus of elasticity of the masonry are fine-tuned as described in Section 4.5.2.

4.3.2 Laser Scanning and Geometric Model Development

Masonry construction must carry loads in a compressive manner requiring curved elements to span distances, such as arches and vaults, and thus result in complex geometries. Over the life of the structure, the geometry is further complicated by the accumulation of structural degradation, such as permanent deformations, crack formation, and support movements. While geometric features must be simplified to reduce computational demands, it is crucial to preserve the structural properties (such as, cross sectional area, moment of inertia, etc.) for achieving high-fidelity numerical models [225]. For this purpose, laser scanning has been successfully applied to three-dimensional surveying of several masonry structures such as, masonry arch bridges [131, 134, 226] and masonry vaulted monuments [136].

To obtain the geometry of Fort Sumter in its present form, a high-resolution three-dimensional laser scan of the fort is performed. The Trimble CX laser scanner uses proprietary technology that combines time-of-flight methodology for long range distance discrimination and phase shift methodology for high short range accuracy. This combined methodology provides high resolution positional measurements of the

	Elastic Modulus (GPa)	Tensile Strength (MPa)	Compressive Strength (MPa)	Density (kg/m³)
Masonry of piers	3.1	2.07	20.7	1500
Masonry of vault	1.58	2.07	20.7	1500
Tabby concrete	0.53	0.53	6.37	1600

Table 2: Material properties of the masonry and tabby concrete.

object's surface at the rate of 54,000 points per second from distances in the order of up to 50 m and measures the return time for the reflection from the object. Assuming the pulse travels with a constant speed, the distance between the laser scanner and the object can be calculated in a straightforward manner [227]. This distance combined with the simultaneously measured horizontal and vertical angles provides high accuracy positions of the collected points. The Trimble CX scanner has a positioning accuracy of 4.5 mm at 30 m and a distance measurement accuracy of 1.2 mm at 30 m. Also, the scanner corrects for temperature and humidity. For the distances within the casemate, the expected positional accuracy is $\pm$ 3mm or better which is insignificant enough to cause a substantial change in the FE model outputs of interest. The scan data was collected from multiple setups of the scanner in and around the casemates. To maintain the integrity of the overall models created from multiple scanner setups, a high accuracy control survey was performed to provide control points for the scanner. The control points were established with procedures that insured gross and systematic errors were accounted for such that random errors were minimized in order to achieve a relative positional accuracy of $\pm$ 1 mm. This ensured that the individual scan setups meshed together accurately.

The laser scan data, obtained in the form of a point cloud is post-processed using Polyworks v.11 geometric modeling systems. Using triangulated irregular network generation, surfaces (triangles) are created between adjacent points in the point cloud. During triangulation, the maximum dihedral angle is kept at 45 degrees and maximum edge length is left unconstrained. The surfaces are then decimated by a factor of 80%. Finally, wireframe models are created from the casemate polygon mesh using RhinoV5 including important geometric features such as cracks and indentations. Figure 30 shows the polygonal mesh and the corresponding wireframe model for Casemate 4.
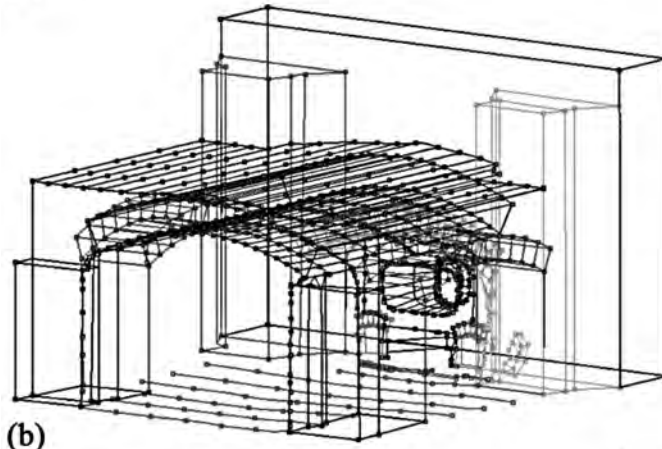
Figure 30: (a) Polygonal mesh of Casemate 4 generated in Polyworks V11; (b) Wireframe of Casemate 4 generated in Rhino v5.0.

4.3.3   Ambient Vibration Testing

Ambient vibration tests are performed on the casemate with a total of 41 measurement points located on the piers, arches and vault (Figure 31). 20 measurement points are located on the piers to measure horizontal acceleration response, while 9 measurement points on the three arches and 12 measurement points on the vault measure vertical acceleration response. The measurement locations are chosen after a careful study of the mode-shapes from a preliminary modal analysis performed on the FE model of the casemate. From this preliminary model, it is observed that for the first 10 modes of the casemate, the most dominant modal displacements are the vertical deflections of the vault and arches and the horizontal deflections of the piers. The sensor locations are chosen accordingly to capture these displacements with sufficient spatial resolution to prevent spatial aliasing.

PCB 393B04 seismic accelerometers are deployed to record 30 minute vibration responses due to ambient excitation forces (see [228] for a discussion on ambient vibration testing of historic masonry monuments). The PCB 393B04 seismic accelerometers have a sensitivity of 1000 mV/g, measurement range of ± 5g and a frequency range of 0.06-450 Hz. The high sensitivity is ideal for measuring low-amplitude ambient vibrations for an operational modal test. A baseband frequency range of 0-1.6 kHz is used with a sampling frequency of 819.2 Hz. Thus, a total of 1,474,560 samples are collected over the measurement duration. The sampling frequency is down-sampled to 160 Hz to reduce the size of the data vectors. Using Enhanced Frequency Domain Decomposition system identification method [229, 230], two modes are extracted from the raw data at 27.48 Hz and 45.2 Hz with a MAC rejection level of 0.8. The identified natural frequencies and the corresponding modes shapes are given in Figure 32.

Figure 31: The experimental set-up showing accelerometers mounted on the vaults and piers.

Figure 32: Comparison of measured and simulated modes with respective MAC values.

4.4 Development of the Structural Finite Element Model

This section discusses the development of the structural finite element model, including (i) generation of the model, (ii) verification of the mesh size and (iii) implementation of substructuring techniques to represent the adjacent components.

4.4.1 Generation of the Finite Element Model

The geometry of the FE model is built in ANSYS 13.0 according to the wireframe model generated in Rhino 5.0 (Figure 33). When necessary, property-preserving approximations are made to eliminate difficulties in geometric modeling and mesh discretization. A predefined 8-noded solid iso-parametric SOLID65 element in ANSYS 13.0 is implemented. SOLID65 element faithfully represents typical masonry failure, characterized by cracking in tension and crushing in compression. SOLID65 element accounts for cracking through a smeared crack analogy and crushing through a plasticity algorithm in three orthogonal directions according to Willam-Warnke failure

69
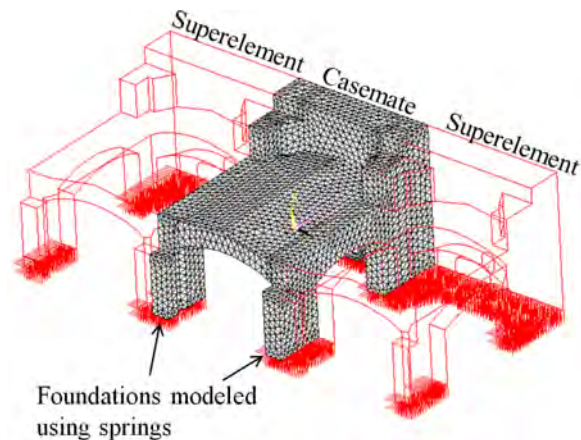
Figure 33: Sub-structured FE model of Casemate 4 with springs used to represent the foundation. The meshed region is the casemate itself adjoined by superelements of the neighboring casemates.

criterion [160, 231]. SOLID65 element allows the input of open and closed crack shear transfer coefficients ranging from 0 to 1, where 0 represents a smooth crack (no shear transfer at the crack surface) and 1 represents a perfectly rough crack (complete shear transfer at the crack surface) [232]. In this study, shear transfer coefficients are prescribed as 0.2 for open cracks and 0.6 for closed cracks, respectively [233, 234].

According to construction drawings, the initial construction of Fort Sumter included a narrow gap between the scarp wall and casemate (Figure 34). This gap has been closed due in part to permanent deformations and in part to the reconstruction of the fort. Currently, the interface between these two structural systems exhibits a contact of unknown nature with highly uncertain force transfer characteristics. In the FE model, this interface is modeled using contact elements on one surface (contact surface, CONTA174 in ANSYS) and target elements on the other surface (target surface, TARGE170 in ANSYS) forming a contact-target pair (as indicated in Figure 26) [235]. In these contact-target pairs, the nature of the force transfer is dictated by normal and tangential contact stiffness. Herein, normal contact stiffness, which controls the penetration, is assumed identical to the stiffness of the masonry beneath
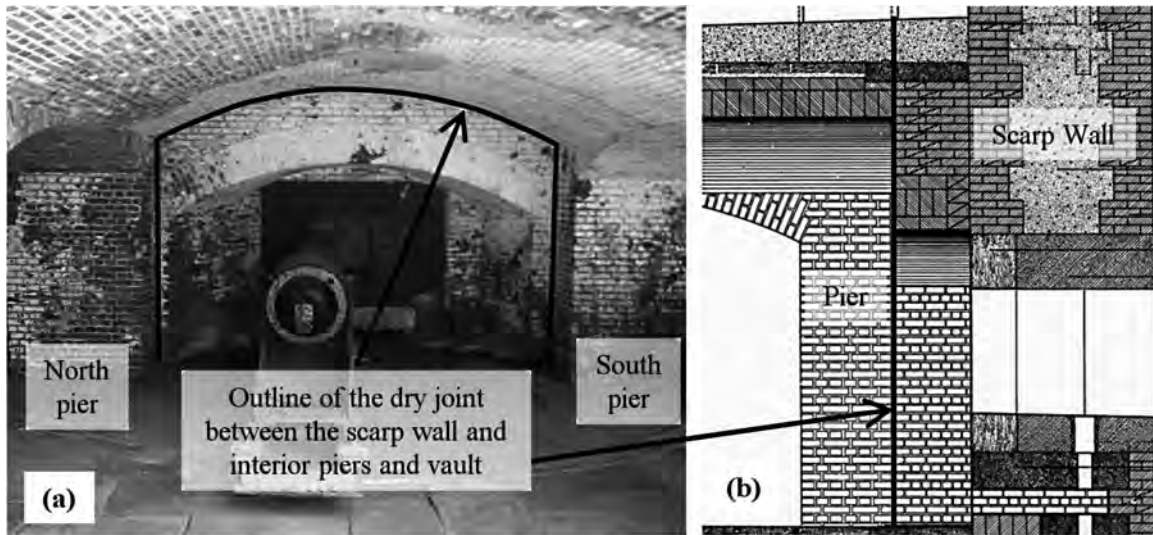
Figure 34: Casemate used for connectivity tests showing the outline of the scarp wall interface (a) in elevation and (b) in section.

the contact surface. The sliding behavior between the scarp wall and piers is a complex combination of interlocking, friction and possible cohesion, which are difficult to measure without destructive tests. The combined tangential force transfer, that governs the sliding behavior at the interface, can be idealized by a friction coefficient applied to the contact elements, which represents the tangential stiffness at the interface. This friction coefficient is, thus, a homogenized idealization of the sliding resistance at the scarp wall interface and must, therefore, be inferred via calibration measurements collected on site, as it will be discussed in Section 4.5.1.

The foundations, which are excluded from the model, provide a semi-rigid support to the casemate which can be idealized by a system of identical but independent, closely spaced vertical and horizontal linear springs (COMBIN14 in ANSYS) distributed throughout the base of the casemate forming a Winkler foundation [236,237] (as indicated in Figure 33). The springs are of course, fictitious and thus, the spring stiffness's are uncertain quantities requiring calibration to experimental measurements as it will be explained later in Section 4.5.2.

The resulting model is thus nonlinear, incorporating (i) the material non-linearity (concrete material model), (ii) geometric non-linearity (P-Δ effects) and (iii) non-linear boundary conditions (contact elements). Thus, the FE model requires an iterative solver. Herein, the Newton-Rhapson equilibrium iteration scheme [238] is used to update the tangent matrix and the restoring force vectors corresponding to the element internal forces. In solving the nonlinear equations, considerable use has been made of the Clemson University high performance computing capability, Palmetto Cluster.

4.4.2 Determining the Optimal Mesh Size

To ensure numerical solutions accuracy and prevent errors from compensating during calibration, a mesh size that strikes a balance between computational time and numerical precision is sought. First, a reference solution is defined using a generalized Richardson extrapolation [165]. This reference solution at element size , i.e. a model with infinite elements, theoretically yields the exact solution. The maximum element edge length, of the solid tetrahedral element is varied between 0.18 m to 0.26 m in steps of 0.01 m. Solution convergence as the maximum element edge length is reduced is checked for the first four free-free natural frequencies. Figure 35 shows that employing a mesh size of 0.23 m yields a numerical uncertainty below 4% of the reference solution, less than the experimental variability that can be attributed to temperature and moisture variations commonly observed in masonry and concrete construction (i.e., 5-6%) [172, 239]. Herein, a maximum element edge length of 0.23 m is implemented, which yields a model with 87,555 elements and 131,232 nodes with three translational degrees of freedom.
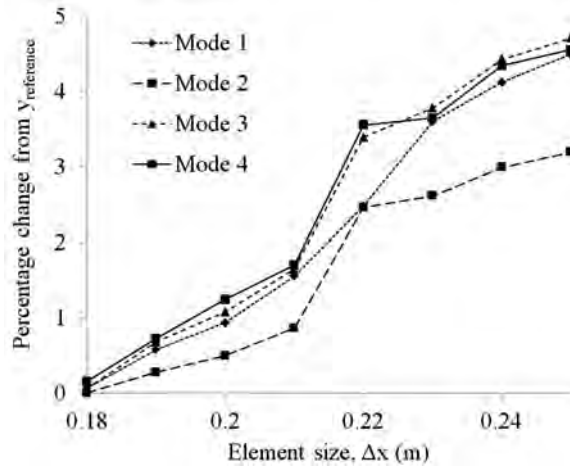
Figure 35: Mesh refinement study showing the change in the first four natural frequencies as a function of the element size.

4.4.3 Substructuring of the Un-modeled Adjacent Casemates

To represent lateral restraints from the un-modeled adjacent casemates, the structure is partitioned into substructures through Component Mode Synthesis (CMS) [240–245]. The method consists of first reducing the order of the components of lesser interest, i.e. the adjacent casemates, down to their interface degrees of freedom, generating what are referred to as superelements. Substructuring must therefore be applied after an appropriate mesh size is selected. Next, these reduced order superelements are coupled to the structure of interest, i.e., Casemate 4, to form the complete system. Note that the loads applied to Casemate 4 are also applied respectively to the adjacent casemates and are transferred through the interface degree-of-freedoms via a reduced superelement load vector. Herein, a fixed-interface CMS is employed, where the eigenvalue problem for the component is solved by restraining each of the interface degrees of freedom, as it is computationally less expensive due to the smaller size of the eigenvalue problem.

Substructuring is computationally advantageous over the common approach of

including adjacent structural components for each axis of symmetry [154, 246]. Note that the use of a substructuring technique for Casemate 4 results in an approximate three-fold reduction in the number of degrees-of-freedom that would be solved and stored if the adjacent casemates were also modeled.

4.5 Calibration of the Structural Finite Element Model

This section reviews the calibration activities that include (i) back-calculation of the unknown friction coefficient of the contact elements used to represent the interface between the casemate and scarp walls and (ii) inference of the imprecisely known spring constants model input parameters.

4.5.1 Back-calculating the Friction Coefficient through Load Path Analysis

Recall Section 4.4.1, where a fictitious friction coefficient is defined to represent the highly uncertain force transfer at the interface between the casemate and scarp wall. This coefficient, being highly dependent upon the present condition of connectivity and interlocking between these two structural components, is back-calculated from available on-site measurements. As suggested by [247], structural connectivity can be inferred by measuring the vibrations transferred between adjacent structural components. If the scarp wall and casemates are in full contact resulting in a complete force transfer (i.e. no sliding), the displacements parallel to the interface must be continuous (i.e. the displacement of the scarp wall and the casemate within the immediate vicinity of the cold-joint must be nearly identical). Therefore, the measured relative dynamic displacements of these two adjacent structural systems can be used to estimate the friction coefficient.

Figure 36: Test set-up on the North pier of Casemate 4 showing two adjacent accelerometers mounted parallel to the scarp wall interface with one accelerometer on the pier and one on the scarp wall.

A hammer impact test is performed [248, 249], in which two accelerometers, one on the casemate pier and one on the scarp wall, are mounted parallel to the interface and a hammer strike is applied parallel to the interface (Figure 36). PCB 393B04 accelerometers with a frequency range of 0.06 to 450 Hz ± 5% and weight of 50 gm each are used to measure the vibration response of the fort. B&K 8210 modal sledge hammer with a 5.44 kg (12 lb) head and a maximum force range of 22.2 kN (5000 lbf) is used to excite the structure. First, the low frequency noise in the acceleration time history measurements are filtered with a high-pass Butterworth filter with a frequency cutoff of 20 Hz [250]. Next, the acceleration response is converted to displacement using cumulative trapezoidal numerical time integration with a time step size of 0.002 sec [251]. The cutoff frequency of 20 Hz that yields displacement response with a zero-mean is applied after studying a range of cut-off frequencies. From displacement time histories, the ratios of the maximum displacements of the casemate and scarp walls are calculated. To capture the potentially nonlinear behavior of the interface, these ratios are calculated for six levels of impact force increasing from 2.6 kN to 8.8 kN. For all force levels, the average relative displacement ratio is obtained to be 3.8, considering both South and North sides of the casemate.
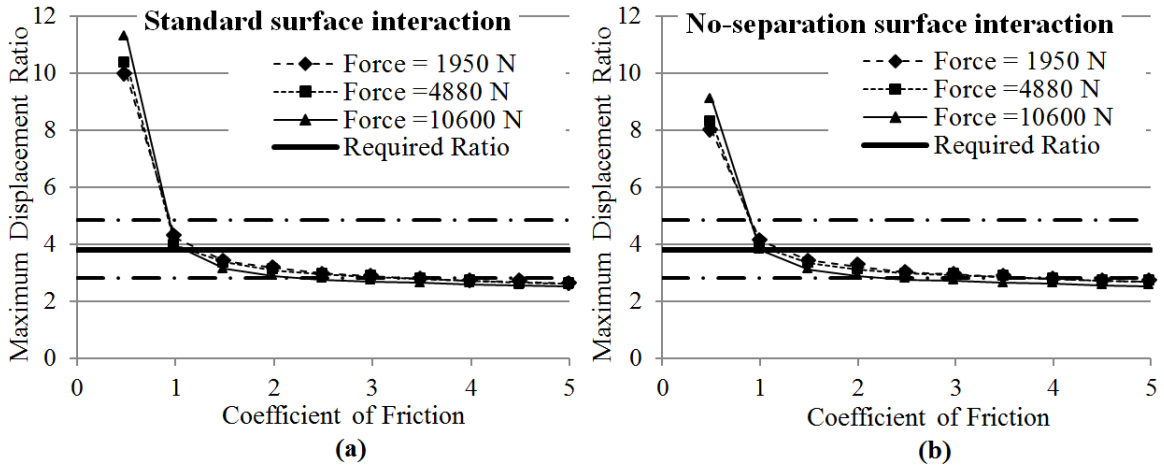
Figure 37: Plot showing the relative displacement ratio using (a) standard surface interaction model and (b) no-separation surface interaction model for different values of applied force and μ.

The friction coefficient μ, in the FE model shown earlier in Figure 33, is back-calculated such that the relative displacement ratio in the FE model is equal to 3.8. This back-calculation is completed considering two surface interaction models that differ in the treatment of separation between surfaces. In Figure 37, by interpolating between data points, a coefficient of 1.14 is obtained as an average of the two surface interaction models and the impact force levels. This value is used for the fictitious friction coefficient for the CONTACT174 elements in the FE model to approximate the connectivity and interlocking behavior between the scarp wall and casemate (as indicated earlier in Figure 26).

4.5.2 Calibrating the uncertain parameters of the Finite Element Model

Despite of the concerted efforts made to collect on-site information regarding the present condition of the fort, uncertainties remain in (i) the material property values and (ii) the spring constant that represents the support at the base of the structure. It

is of value to reduce the uncertainty in these input parameters by systematically comparing the numerical model predictions of global mechanical behavior of the casemate against those that are measured on site, a process commonly known as model calibration (see [154] for a thorough overview of model calibration as applied to masonry monuments).

With the modal parameters of the fort identified in Section 4.3.3, uncertain FE model input parameters can be calibrated. Since computation of modal parameters is deeply rooted in the linearity assumption, only parameters affecting the linear response can be calibrated, namely the elastic modulus of the materials and spring constants representing the boundary conditions. The elastic modulus of walls and piers (θ_1), the elastic modulus of the vaults (θ_2) (recall Figure 26) and stiffness of the springs at the supports (θ_3) (recall Figure 33) are imprecisely known input parameters in the FE model. Through a fully Bayesian implementation of the statistical inference procedure proposed by [168], these three model input parameters are inferred by exploiting the availability of known modal parameters (see [15] for the derivations of the statistical inference approach and [154] for a discussion on the implementation of this procedure on a masonry monument).

For the material properties (θ_1 and θ_2), in the absence of a sufficiently large number of material tests, prior distributions are defined to be uniform distributions. The bounding limits of the uniform distribution are determined such that the predicted natural modal parameters envelop the experimentally measured modal parameters; thus for θ_1 a range of 3 GPa – 4 GPa and for θ_2 a range of 1.5 GPa – 2.5 GPa are considered. The bounding limits of θ_2 are considered to be lower than those of θ_1 due to the vertical orientation of the joints in the vaults.

The range for the spring constant θ_3 is defined to ensure a semi-rigid connection through a parametric analysis of the first six natural frequencies, in which the stiffness
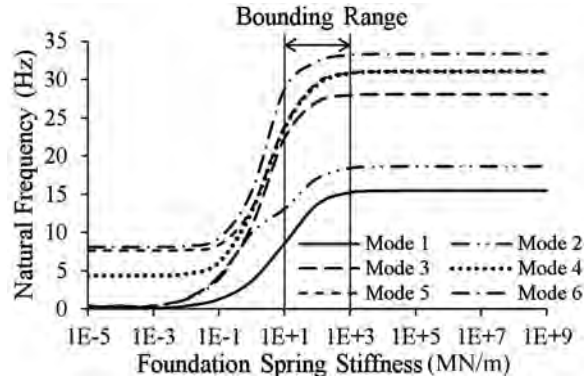
Figure 38: The first six natural frequencies obtained from the FE model plotted against logarithmically varied foundation spring stiffness.

of the linear springs is logarithmically varied to find the stiffness values at which the foundation becomes effectively pinned (lower bound) and effectively rigid (upper bound) (Figure 38). According to Figure 38, the prior distribution of the spring constant is set to be uniform between 10 and 10^3 MN/m.

The domain defined by the prior distributions of the three calibration parameters is explored via Markov Chain Monte Carlo (MCMC) sampling. A total of 20,000 MCMC accepted runs are obtained to generate the posterior distributions for the calibration parameters. These posterior distributions yield the likely values for the three uncertain model input parameters that improve the agreement between the two experimentally measured and predicted natural frequencies (see Figure 15).

The values corresponding to the peak of the probability distributions shown in Figure 39 are used as the calibrated input parameters, which correspond to an elastic modulus of 3.1 GPa for the walls and piers (θ_1), 1.58 GPa for the elastic modulus of the vault (θ_2), and a support spring stiffness of 60 MN/m (θ_3). The correlation between the first two experimental modes and the corresponding model predictions obtained with these calibrated input parameters is given in Figure 32.

The calibrated model yields a first natural frequency, which is 8.8% higher and
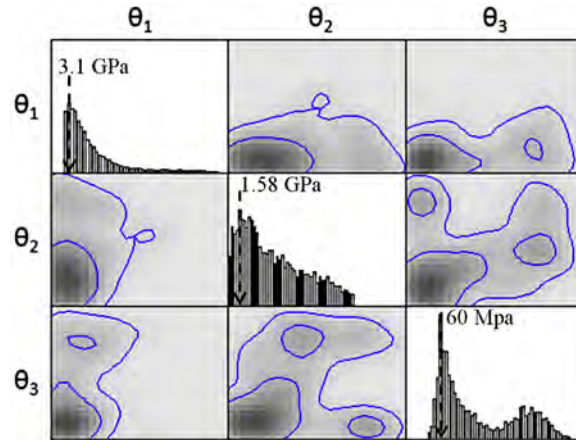
Figure 39: Posterior distribution of input parameters (θ_1 is the elastic modulus of walls and piers, θ_2 is the elastic modulus vaults and θ_3 is the foundation spring stiffness)

a second natural frequency, which is 5.3% lower than the experimentally obtained natural frequencies. While comparing the agreement between experiments and model predictions, another commonly used metric is modal assurance criteria (MAC) that represents the degree of linear correspondence between two mode shape vectors [252]. MAC lies between zero and unity, where a higher MAC value indicates better agreement. Between the experiments and the calibrated numerical model, a MAC value of 0.86 for the first mode and 0.60 for the second mode is observed for the experimental and simulated mode shapes.

4.6 Remaining Uncertainties

Models that are calibrated in a deterministic manner to maximize fidelity to limited experiments do not guarantee fidelity in their entire operational domain. In Section 4.5, the elastic moduli of two materials assumed in the FE model are calibrated using natural frequency and mode shapes. Despite the calibration efforts, uncertainty still remains in the two elastic moduli for the following reasons:

1. Spatial variations in the material properties: By using homogenized deterministic parameters to represent the masonry over entire structural components, the effects of brick-to-brick and joint-to-joint variations in material properties is ignored. Such an assumption may not be suitable for making predictions of quantities other than the ones used for calibration.

2. Temporal variations in material properties: Similar to spatial variations, time-dependent variations in material properties are ignored in the calibration. Factors such as moisture, ambient temperature and material aging modify properties of masonry.

Thus, predictive capability of the FE model depends on how well fidelity is maintained under such variations. The calibrated values of the elastic moduli maximize fidelity (i.e. minimize prediction error) to the first two measured natural frequencies and mode shapes, i.e. calibration experimental data. Thus, the calibrated parameter values are the best guess given the limited experimental measurements. In an effort to maximize fidelity, the calibration process may infer input parameter realizations that render the model highly sensitive to variation in parameter values. By quantifying the robustness of this model, the usefulness of the calibrated model in making predictions of required structural behavior can be validated. Observing the trade-off between allowable prediction error and parametric uncertainty allows making a decision whether to perform additional experiments to reduce uncertainty or accept larger errors in model predictions.

4.6.1 Design of Experiments

The usefulness of the model is specific to the purpose of the model, i.e. the desired prediction or model output. Here, for the purpose of demonstration, the desired

80

	Calibrated value	Upper bound	Lower bound
K_1	3.1 GPa	2.32 GPa	3.87 GPa
K_2	1.58 GPa	1.19 GPa	1.98 GPa

Table 3: Calibrated values, upper and lower bounds for uncertainty propagation.

prediction is the strain at the underside of the vault due to differential settlement. The settlement scenario considered here is the differential settlement of the south piers with respect to the north piers (Refer Figure 26) with a maximum settlement magnitude of 0.1 m. The simulation is divided into 25 substeps and normal strains are recorded at each step. The two uncertain elastic moduli, K_1 for the piers and K_2 for the vault, are sampled with a uniform distribution with a 25% uncertainty centered around the calibrated values (recall Section 4.5.2). The upper and lower bounds on the two parameters are given in Table 3. The sampled input space thus consists of combination of 20 uniformly spaced samples each of K_1 and K_2 resulting in 400 settlement simulations.

The two model outputs of interest Y_1 and Y_2 represent the vector composed of nodal strain predictions at each node at the underside of the vault in the X-direction (N-S, along the span of the vault) and Y-direction (E-W, along the length of the vault) respectively at each of the 25 substeps. Corresponding prediction errors R_1 and R_2 are calculated at each substep as the sum of the absolute difference with respect to the strain vectors $\tilde{Y}_1$ and $\tilde{Y}_2$ calculated on the model with calibrated elastic moduli values. R_1 and R_2 are plotted for 5 substep intervals in Figure 40 and 41 respectively.

4.6.2   Trade-off Analysis

Satisfying boundaries are obtained in the input space for varying levels of error tolerance R_c as well as at increasing time steps. Figures 42 to 46 show satisfying boundaries at an interval of 5 substeps. Recall that the 0.1m settlement is divided into 25 equal
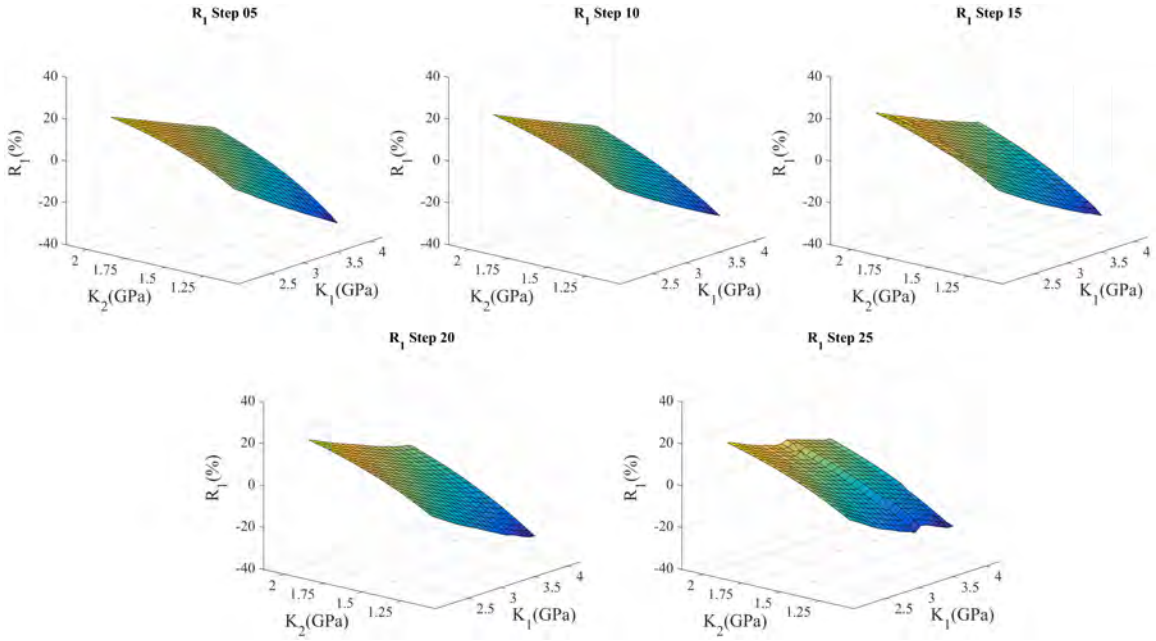
Figure 40: Error in X-direction strain predictions (R_1) for incremental load steps.
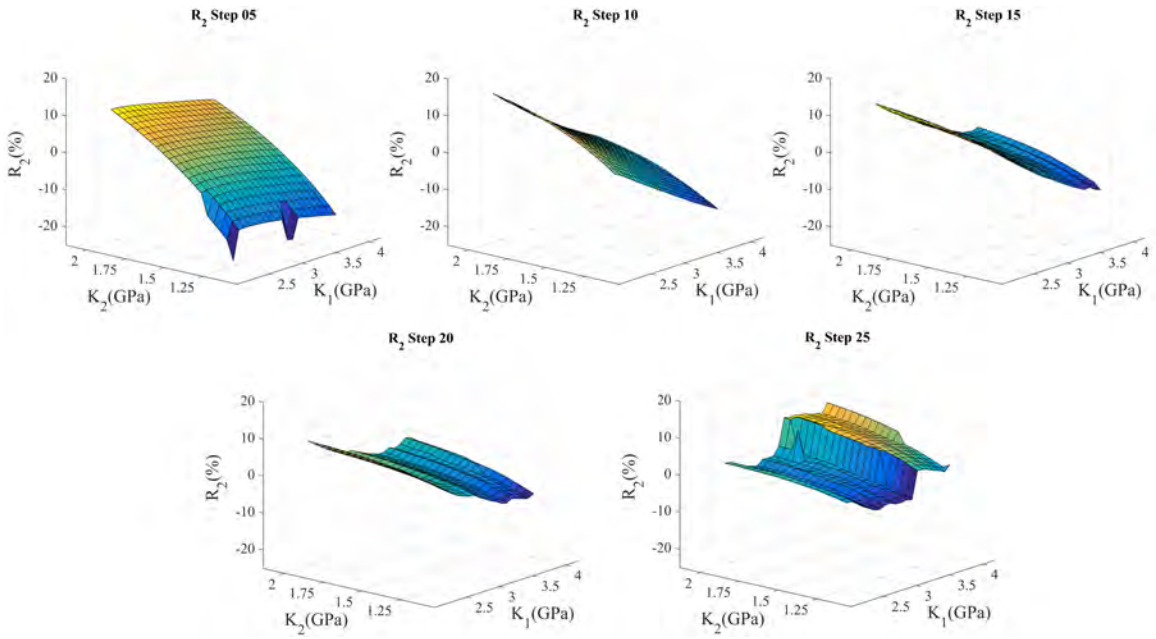
Figure 41: Error in Y-direction strain predictions (R_2) for incremental load steps.

substeps. Thus, the 5th substep corresponds to 0.02m, 10th step corresponds to 0.04m settlement and so on. It is evident at the 25th substep, the input-output relation no longer obeys the proper continuous behavior assumption for using satisfying boundaries. For instance, in Figure 46 corresponding to R_c of 6%, the parameter realizations are no longer compact, causing the satisfying boundary to encompass non-satisfying parameter realizations.

Figure 47 shows the trade-off between uncertainty in parameters, the error tolerance and probability of satisfying at increasing substeps denoting increasing settlement. Substeps 5 to 20 show expected relations between the three criteria. Probability of satisfying increases monotonically with increasing error tolerance and decreases monotonically with increasing uncertainty. However, for substep 25 (Figure 46), the monotonic relation is violated due to the non-compact input-output relation, due to which, the satisfying boundary encompasses failed samples. Thus, at this load-level the validity of the trade-off analysis is limited.

Some key decisions can be arrived at using the relation between the three criteria as seen in Figure 47. For instance, say the model developer decides that a 5% variability in predictions of strains under settlement is tolerable as such an error is unlikely to lead to potentially disastrous decision. Under this constraint, a 5% uncertainty or variability in the elastic moduli can provide reliable results with a probability of satisfying of 100%. Now, suppose the model developer realizes that anything less than 10% uncertainty is difficult to achieve even after further experimentation. In such a case, the model developer can specify to the end user that the confidence in model predictions is 70%, i.e. there is a 30% probability that model predictions vary more than 5%. Essentially, if any one of the criteria is known, the other two can be calculated. Based on this information, the model developer may decide to conduct further experiments or specify the tolerable output variability of the model or specify
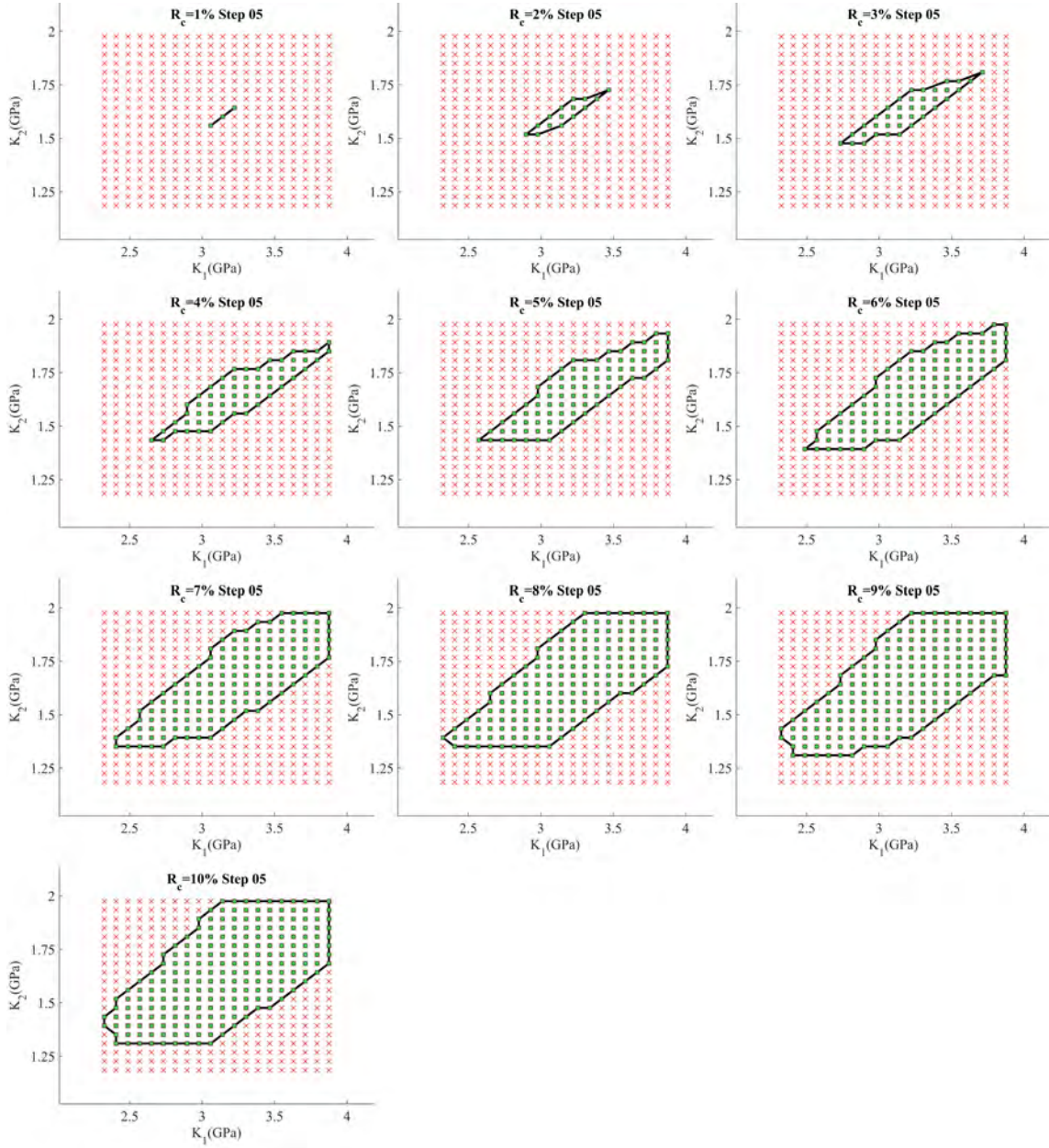
Figure 42: Satisfying boundaries for increasing error tolerance R_c obtained at the 5th substep.
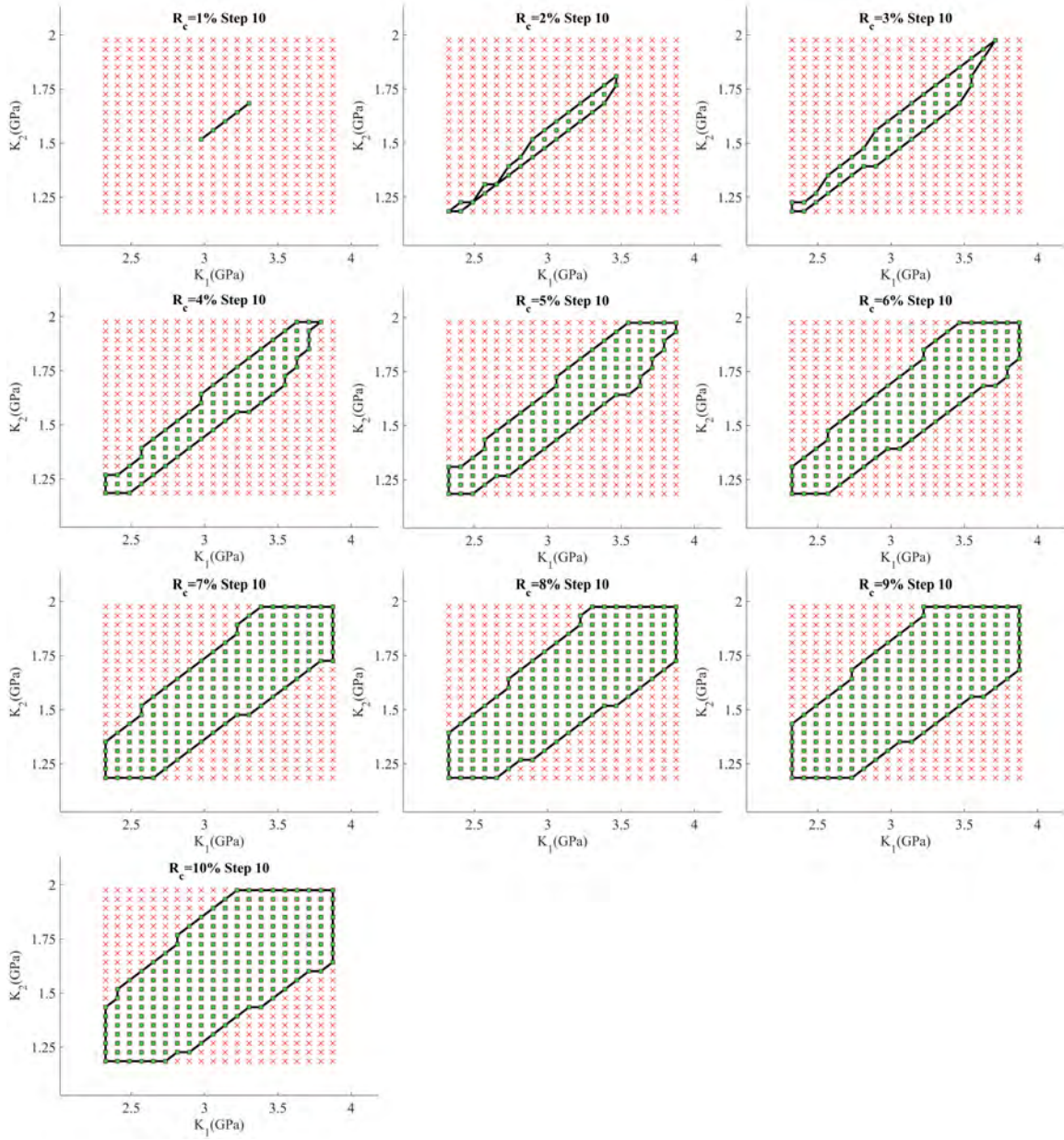
Figure 43: Satisfying boundaries for increasing error tolerance R_c obtained at the 10th substep.
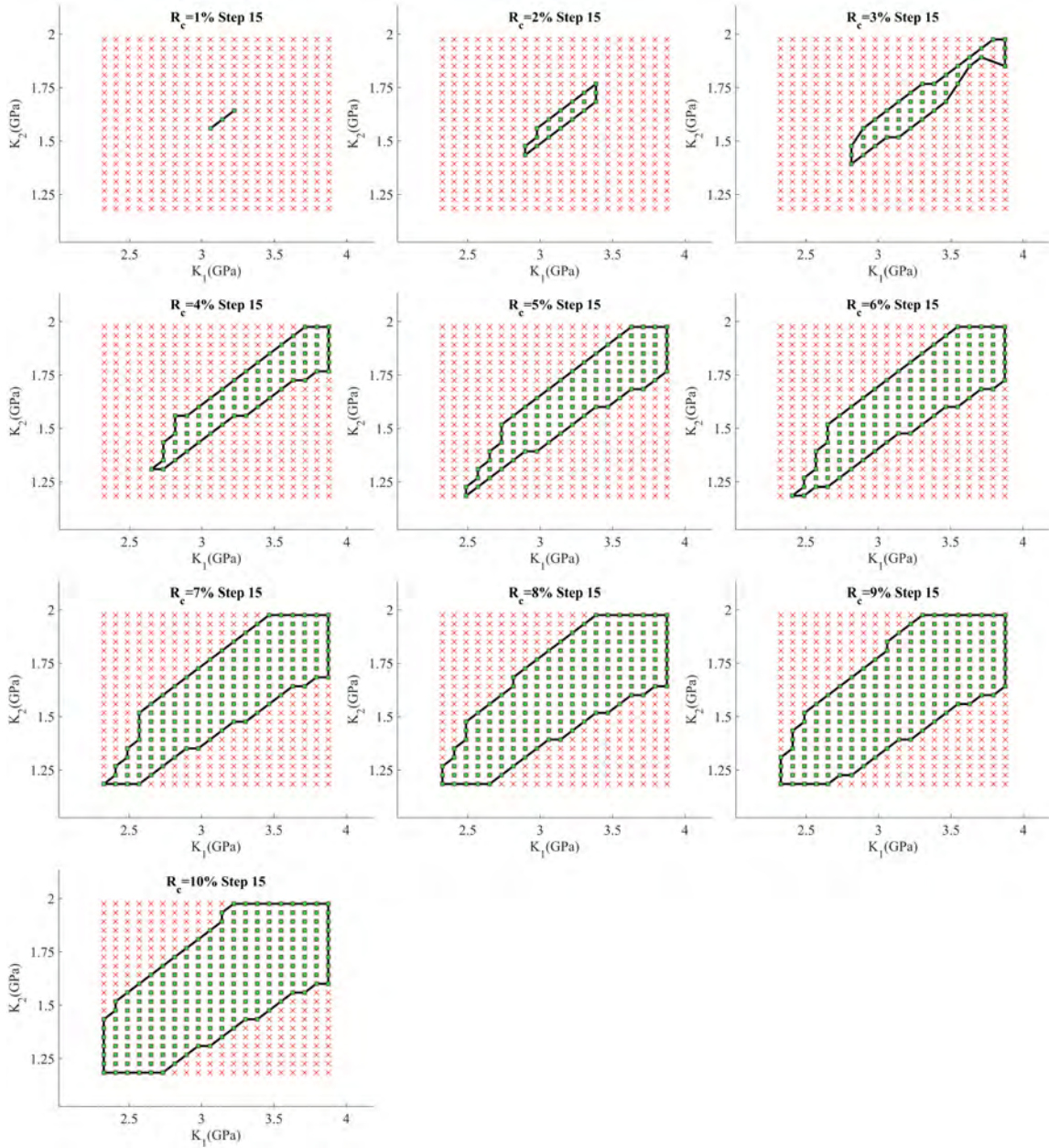
Figure 44: Satisfying boundaries for increasing error tolerance R_c obtained at the 15th substep.
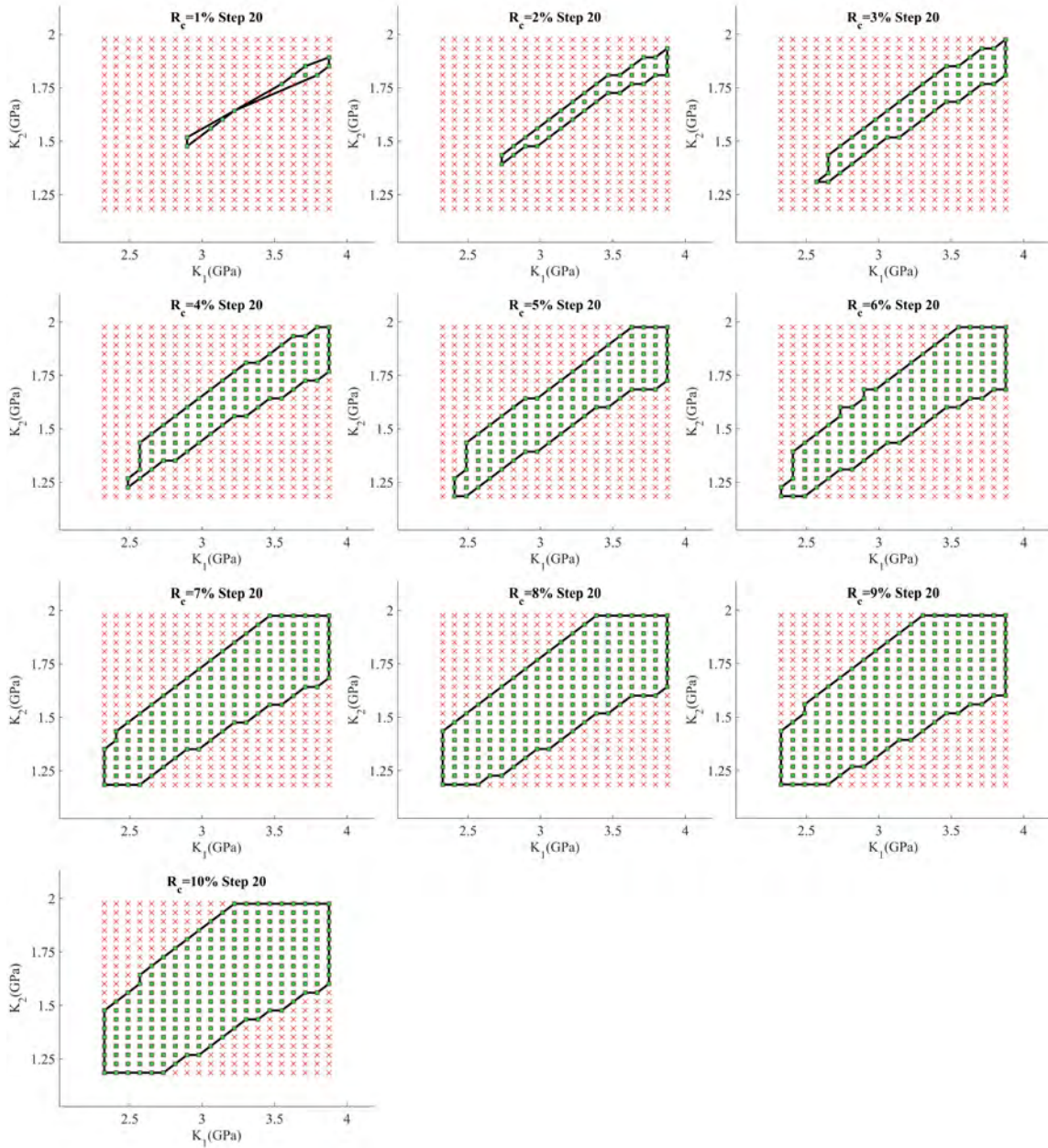
Figure 45: Satisfying boundaries for increasing error tolerance R_c obtained at the 20th substep.
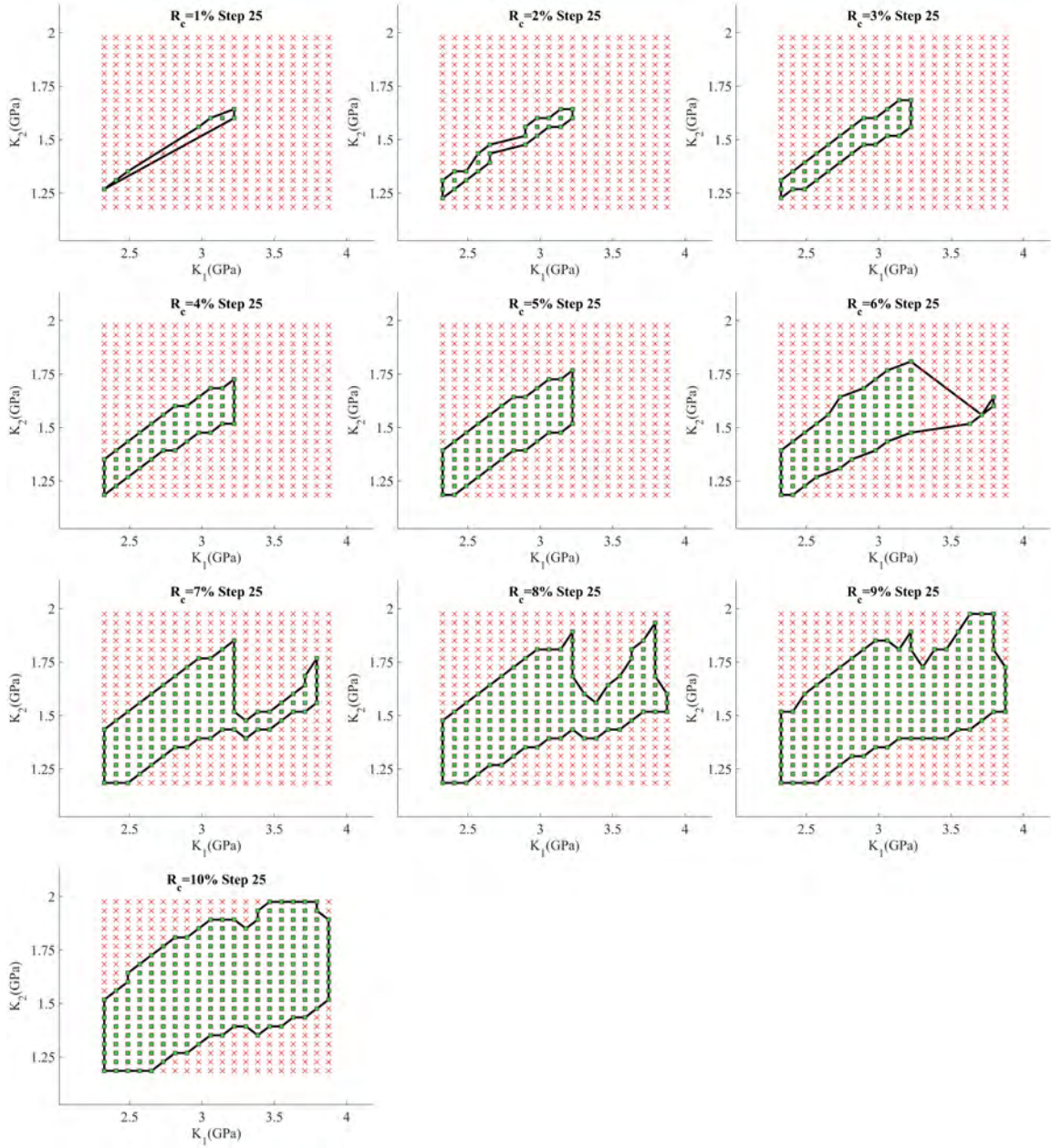
Figure 46: Satisfying boundaries for increasing error tolerance R_c obtained at the 25th substep.
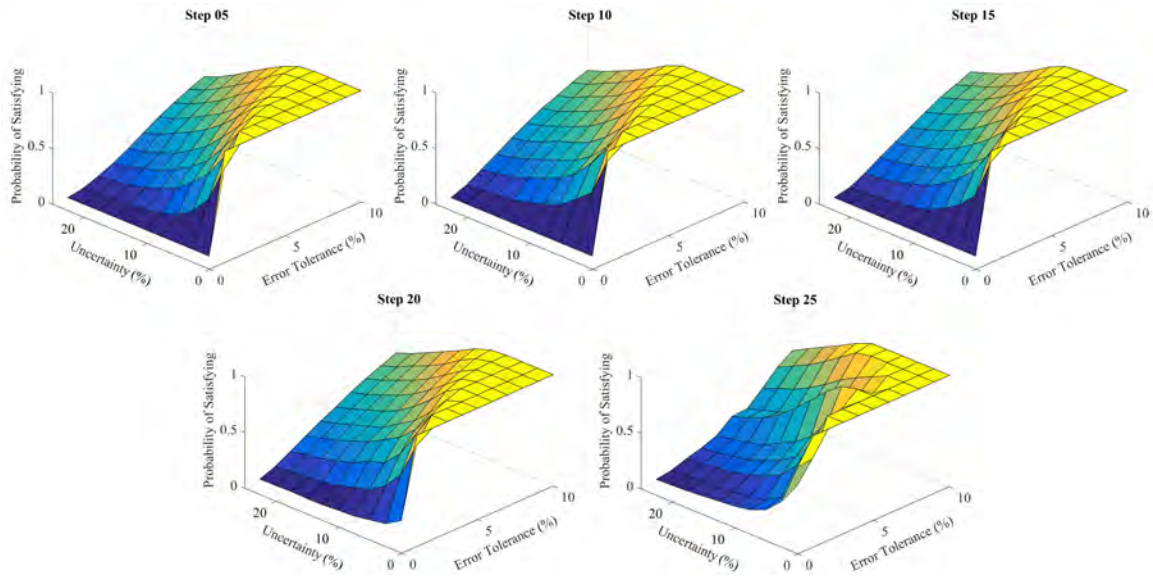
Figure 47: Three-dimensional plot showing trade-off between probability of satisfying, error tolerance and parametric uncertainty for increasing substeps.

the required probability of success.

4.7   Support Settlement Analysis of Fort Sumter

Seven possible settlement configurations are simulated, each with a maximum magnitude of 100 mm in the vertical direction as shown in Figure 48. Aside from the settlement of the supports, the self-weight of the casemate itself is also considered in the simulation. The configurations are designed accounting for the two adjacent casemates on the two sides of Casemate 4. The settlement configurations are generated as bi-variate quadratic curves using the MATLAB procedure polyfitn [253] and are designed to encompass global settlement of the three casemates as well as local settlement of the piers and walls. The settlement configurations are grouped as sagging configurations (1, 2 and 3), pier settlement (4) and tilting settlements (5, 6 and 7). As the settlement is incremented, cracks begin to develop in the casemate. The pattern of the cracking is observed to be dependent upon the settlement configuration
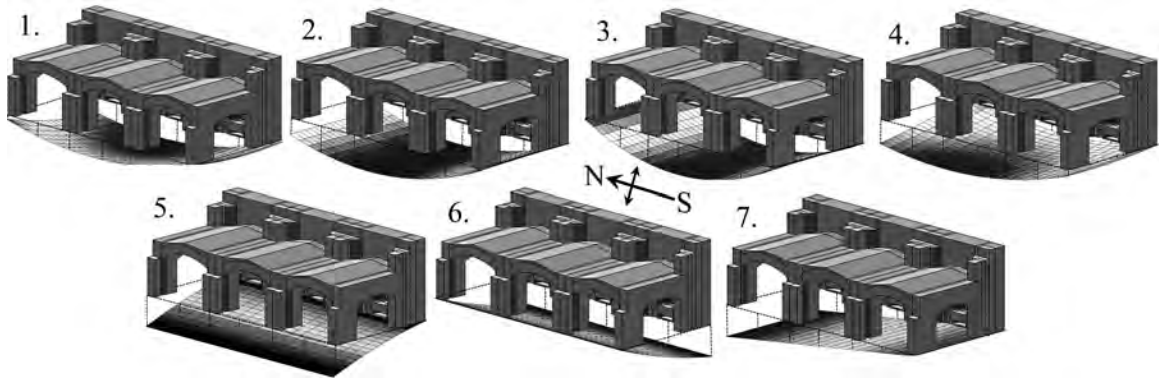
Figure 48: Seven settlement configurations used for FE simulations.

and magnitude:

Sagging Settlement Configuration 1 simulates the unsymmetrical sagging under the north side of the scarp wall. The cracks begin forming at the bottom of the scarp wall on the intact side and gradually progress upwards. At around 50 mm of settlement, a crack which initiates at the base of the scarp wall on the intact side progresses diagonally across the scarp wall and fully forms a diagonal crack (indicated with a dotted line in Figure 49). While such a settlement results in substantial cracking within the scarp wall, owing to the cold joint between the scarp wall and the rest of the casemate, the vault, arches and the inner piers are not significantly affected. Configuration 2 simulates the sagging under the entire north side of the casemate. Beginning at the scarp wall, heavy cracking is observed on the less settled side of the casemate. At approximately 50 mm of settlement, a complete diagonal crack is formed on the scarp wall (indicated by a dotted line in Figure 49). Cracking is also initiated at the springing of the arch on the South side at a 50 mm settlement magnitude. Configuration 3 simulates symmetrical sagging of the ground, which results in symmetrical cracking of the arches (indicated as a and b in Fig 49). At approximately 60 mm settlement, a load bearing arch is formed within the scarp wall
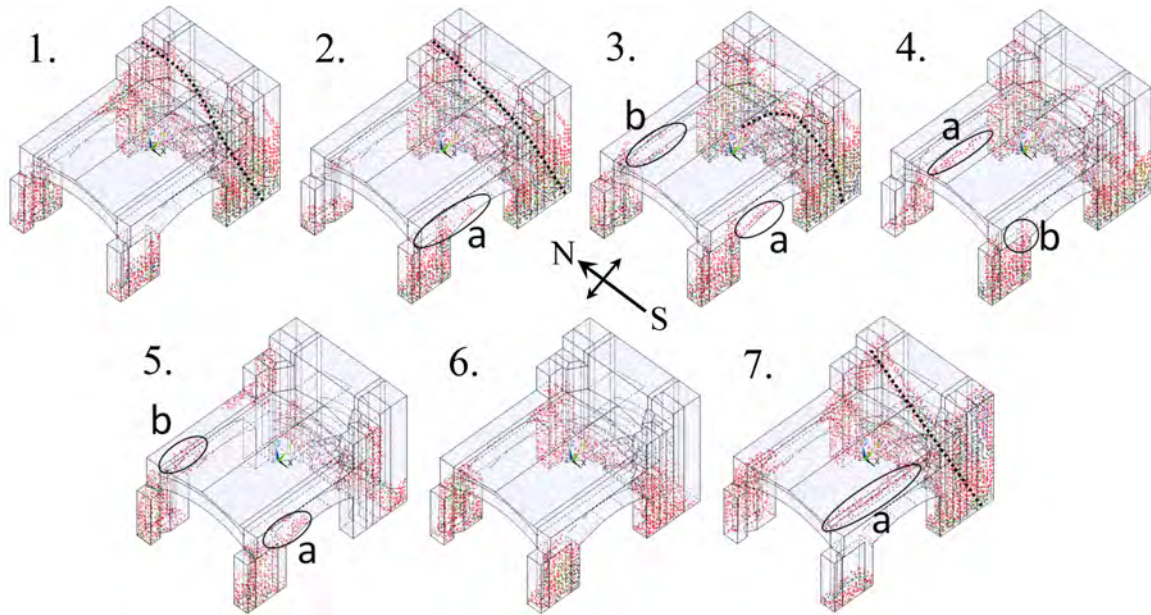
Figure 49: Crack plots of the casemate under 100 mm settlement of the seven configurations.

to span across the regions of settlement (as indicated by a dotted line in Figure 49) in agreement with an earlier simulation-based study by [213].

Settlement of Piers   Under Configuration 4, which simulates settlement under the north-pier, cracking begins first at the base of the scarp wall on the south side and the south-pier at a settlement magnitude of 10 mm. The configuration also leads to cracks at the springing of the arch (indicated as b in Figure 49) at a settlement magnitude of approximately 60 mm. Extensive cracking and formation of a hinge are also observed within the vault (indicated as a in Figure 49). It can be concluded that when one of the piers settles more than the other, unsymmetrical cracking of the vault occurs on the side of the pier that exhibits more settling. Also, the pier itself that settles less among the two endures more cracking than that which settles more.

91

Tilting settlements Configuration 5 represents inward tilting of the foundation towards the west. According to the model predictions, cracking is predicted at the springing of the arch above the inner piers of the casemate (indicated as a and b in Figure 49). Cracking is initiated at the outer tips of the base of the north- and south-piers at a settlement magnitude of approximately 10 mm while cracking at the outer edge of the base of the scarp wall is initiated at approximately 20 mm. These cracks gradually progress upwards and reach the springing point of the arch (indicated as a and b in Figure 49) at a magnitude of 50 mm. Configuration 6 simulates outward tilting of the foundation towards the east. Cracking is predicted at the springing point of the arches above the inner piers on the side of the scarp wall. At a settlement magnitude of 15 mm, cracking at the inner tips of the base of the piers is first observed, with the inner edge of the base of the scarp wall beginning to crack at around a 40 mm of settlement. Cracks in the piers and scarp wall progress upwards and reach the springing point of the arch at approximately 60 mm of settlement. Settlement in Configuration 6, which represents the outward tilting of the foundation towards the east, is less structurally critical compared to Configuration 5 primarily due to the highly stiff scarp wall resisting the thrust of the vault. Finally, Configuration 7 simulates tilting of the foundation towards the north in the longitudinal direction of the right face. The south pier of the casemate is heavily cracked due to the horizontal thrust exerted by the vault. Diagonal cracking, initiated in the scarp wall originating from the base on the south side runs completely across the scarp wall at a 50 mm settlement (indicated by a dotted line in Figure 49). Cracking at the springing point of the north arch is initiated at a 50 mm of settlement (indicated as b in Figure 49), while cracking of the vault on the south side is initiated at 80 mm (indicated as a in Figure 49). The cracks in the vault form a hinge rapidly through the length of the vault at a 90 mm settlement.

Results presented in this section reveal that the mechanism, in which the fort withstands the support settlement, differs significantly for different settlement configurations. Therefore, visual observations of crack patterns can be used to diagnose potential settlement configurations. However, it must be noted that not every cracking in the structure can be attributed to settlement. Cracking may occur due to temperature and moisture expansion, seismic and high wind activity, forces from adjacent buildings, chemical and biological processes, freeze-thaw cycles, etc.

4.8   Qualitative Classification of Settlement-Induced Damage

When cracking occurs within an element, the strain in the direction normal to the cracked element edge increases significantly. Total strain is, thus, proportional to the number of cracks and their widths. Therefore, the degree of settlement induced damage can be quantified using the total principal strain in the entire structure. Figure 50 plots the total principal strain as a function of the settlement magnitude. It can be deduced that configuration 3, which is the symmetric sagging under the casemate is the most damaged case in terms of the intensity of crack formation, while configuration 5 which is the outwards tilting of the casemate is the least damaged in the same sense.

Focusing on the damage patterns discussed in section 7, a qualitative damage classification scheme is devised. Minor smeared cracking limited to walls and/or piers is classified as slight damage, while the initiation of large cracks or discontinuities in walls and piers is classified as moderate damage. Severe damage is reported when through cracks are completely formed in the walls and piers. When the discontinuities are formed in the vaults and arches in the form of hinges, an instability condition is assumed. Although, further cracking may be allowed past the assumed instability

93
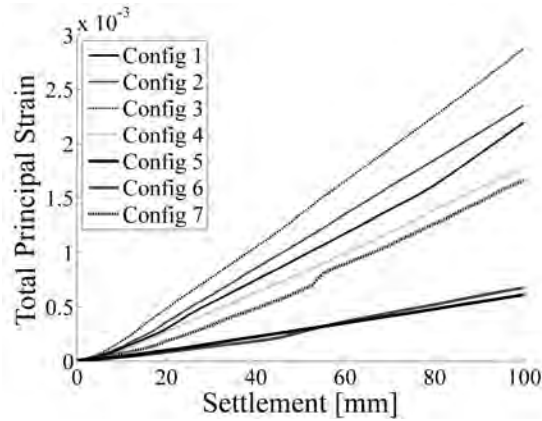
Figure 50: Total principal strain plotted as a function of settlement magnitude.
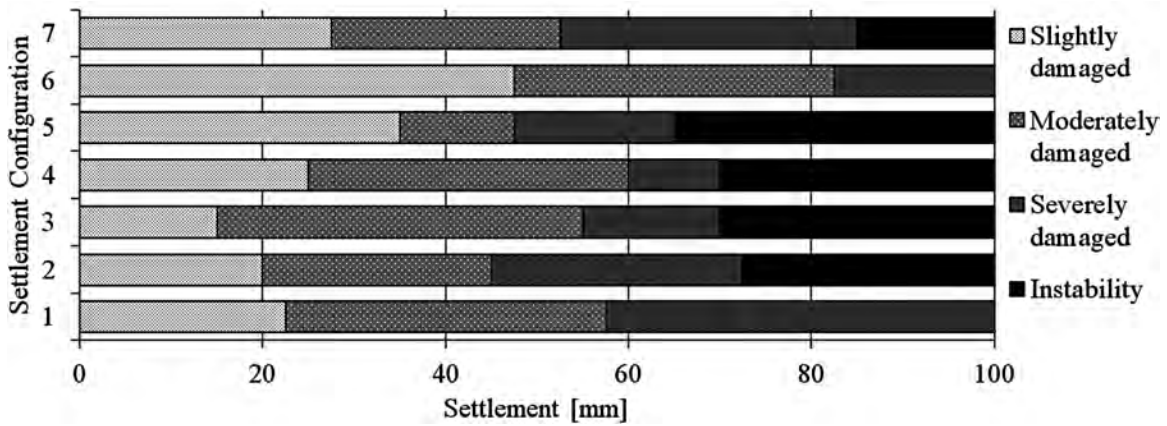
Figure 51: Qualitative structural damage matrix showing damage levels based on crack locations and magnitudes.

condition, cracking of vaults and arches is treated as a critical condition as structural collapse is imminent at any value of further settlement. Figure 51 indicates the settlement magnitudes at which the above-mentioned damage classifications occur. The instability condition, as defined herein, is not experienced under configurations 1 and 6 up until a 100 mm settlement magnitude. The assumed instability conditions are experienced under configurations 2, 3, 4 and 5 between 60 and 80 mm settlements.

4.9   Conclusions

This chapter investigates settlement-induced damage patterns specifically focusing on Fort Sumter, S.C., a historic 19th century island fort, through a numerical analysis substantiated with experiments and field investigations. The FE model of one of the fort's casemate is built that allows cracking of the masonry material when the failure criterion is exceeded. The input parameters of the model are determined following on-site experiments and model calibration.

In order to test the model's usefulness in making predictions of structural response under foundation settlement, the model's robustness to the remaining uncertainties in the calibrated parameters is assessed using the satisfying boundary approach. Critical decisions regarding the amount of tolerable uncertainty and expected variability in predictions can be reached at using the tradeoff between parameter uncertainty, error tolerance and probability of successful predictions.

A total of seven settlement configurations are simulated to include global settlements as well as localized settlements under the piers and walls. The cracking behavior is observed at each step as the settlement magnitude is increased up to 100 mm in increments of 2.5 mm. The formation and progression of cracks are observed to be unique to the settlement configurations. Therefore, by visual investigations of early warning signs in form of cracks, the stewards of historic monuments can draw conclusions regarding the settlement configuration causing damage to the structure.

Unsymmetrical sagging types of settlements are characterized by diagonal cracking of the scarp wall originating from the bottom on the less-settled side. Symmetric sagging under the casemate, however, forms cracks that originate from the bottom of the scarp wall from both sides and converge at the center forming an arch that spans the length of the casemate and bears the loads of the wall above. Cracks due to

stress concentrations are seen for most settlement configurations at the intersection of the structural members such as the springing of the arches and vaults. Cracking of the vault is observed in configurations that involve differential settlements of the piers. Cracks once formed in the vaults, progress rapidly without warning as the settlement increases. Thus, cracking of the vault should be taken as a structural stability concern.

Structural damage is quantified by the total principal strain in the casemate as it approximately reflects the number of cracks and the crack widths. Symmetrical sagging is found to be the settlement scenario that amounts to the most crack damage. A qualitative damage classification system is devised on the basis of crack propagation and location that indicates the level of damage encountered as the settlement magnitude increases. The damage levels range from slight damage signifying minor cracking in walls and piers to instability conditions when cracks occur in the horizontal members i.e. vaults and arches.

In future studies, the settlement analysis must be performed by also incorporating foundation soil properties and the soil-structure interactions that will alleviate the simplifications assumed in this study for the spring foundations that were assumed linear and isotropic. Such a study can also assess the effect of the fort on its foundation to infer the possible settlements to be expected in the future. Both a sound numerical model of the fort, discussed in this chapter, as well as a dependable numerical model of the soil will be required for coupling of these two fields.

5   ASSESSMENT OF STRENGTH DEGRADATION DUE TO DAMAGE USING A LOAD PATH-BASED APPROACH

5.1   Introduction

Masonry monuments constitute the vast majority of historic heritage around the world[5]. The negative effects of aging and accumulated damage have degraded the structural integrity of these monuments, making it necessary to closely monitor their remaining load-carrying capacity. Over the last two decades, Structural Health Monitoring (SHM) has been developed as an automated approach for such monitoring by detecting the onset of damage from the changes in the monument's response features measured in a non-destructive and continuous (or quasi-continuous) manner [254–260]. Dynamic testing has been a prominent damage identification technique for SHM, relying on the basic principle that change in the stiffness distribution in a structure from damage (similarly, from repair or retrofit activities) alters the structure's dynamic behavior [179, 261–264]. This concept has been successfully demonstrated on several historic masonry monuments primarily through the monitoring of modal parameters, such as natural frequencies and mode shapes [265–271].

SHM's popularity in long-term assessment of historic masonry can be attributed to its potential for enabling condition based repair and strengthening efforts, providing life-safety and economic benefits, and supporting historic preservation [170, 272]. However, the missing link between what is being measured (stiffness-related quantities) and what needs to be known for historic preservation (strength-related quan-

---

[5]Until the mid-19th century the only other widely used construction material was timber. Most of timber structures have since decayed or burnt during fires.

tities) is hindering these ambitious goals [181]. Dynamic response features provide an indication of stiffness degradation due to damage. However, structural engineers are more interested in the actual loss of load-carrying capacity to both justify and configure repair and rehabilitation activities. Stiffness degradation is seldom a direct representation of strength degradation and hence, determining the degree of change in such dynamic response features as natural frequencies and mode shapes is insufficient to assess how much the integrity of the structure (i.e. load-carrying capacity) is compromised due to damage. Model updating techniques implemented to pinpoint the location of damage, although useful for aiding inspection, still leave the stewards of historic monuments uninformed about the negative effects of the identified damage on structural integrity.

In this article, the authors implement a load path-based approach to first evaluate the negative effects of damage on structural redundancy and then, link this determined redundancy loss to the reduction in load-carrying capacity. In this context, redundancy is the ability of the structure to assume alternative load paths to carry the applied load such that if one path is disturbed due to damage, the loads can safely be transferred to the supports. Here, load path refers to the trajectory of the load between the point of application and the supports. The onset and progression of cracks disturbs this trajectory forcing the system to transfer the loads through alternative paths, gradually reducing the structural redundancy. In general, the higher the loss in a structure's redundancy, the higher the loss in its load-carrying capacity [273,274]. Using this relation, this study proposes a redundancy measure based on quantified disturbance in load path to estimate the loss in load-carrying capacity. In this study, disturbance in load path due to damage is calculated as the total force that must be redistributed from damaged regions to the intact regions within the structure. This calculation is performed using computational models of the structural system. Using

load path disturbance in conjunction with the relative position and magnitude of damage, this study formulates a redundancy measure. Thereafter, empirical relations between the redundancy measure and the consequent loss in load-carrying capacity are derived to enable estimation of strength degradation due to identified damage. In this chapter, the feasibility and application of the proposed approach are demonstrated on a 19th century brick masonry coastal fortification, Fort Sumter located in Charleston, S.C.

This chapter is organized as follows. Section 5.2 provides a brief background on the current practices and limitations of non-destructive vibration-based damage detection in the context of preservation of historic masonry monuments. Section 5.3 first demonstrates the dependance of load-carrying capacity on the disturbance in load paths due to damage, next provides a brief background on the available redundancy measures and finally presents a generalized methodology to calculate redundancy based on change in load path. Section 5.4 details the implementation of the proposed load path-based redundancy measure on the case-study structure. Finally, concluding remarks, including a discussion of generalizations and limitations of the proposed approach are provided in Section 5.8.

5.2 Background Perspectives on Vibration-based Damage Detection

In vibration-based SHM, changes in the predefined response features from an earlier measured reference state are used to infer the onset of damage (see [254, 261, 275] for a review). Vast majority of the damage detection studies on masonry structures have been completed on scaled laboratory models using shifts, for instance, in the modal parameters (natural frequencies, mode shapes and their derivatives) between

99

the damaged and undamaged (or repaired) state. For instance, [265] studied two laboratory scaled arches, one intact and one with spandrel wall separation and noted differences in mode shapes as well as mode sequences. [266] observed reduction in the first natural frequency of a $1/5^{\text{th}}$ scaled masonry building due to formation of cracks induced via a shake table. [172] imposed progressive damage scenarios on a laboratory scaled arch by increasing static load and observed that the natural frequencies identified after each load increment show a decreasing trend with progressing damage. [276] recorded reduction in natural frequencies of a full-scale model of a masonry triumphal arch after damage was induced in the form of settlement of one of the arch pedestals. Studies conducted on existing monuments were primarily focused on the changes in the dynamic behavior due to repair and retrofit activities as it is implausible to damage an existing masonry monument for research purposes. For instance, [275, 277–280] all documented an increase (up to 40-45%) in the natural frequencies after a retrofit or repair campaign.

Rytter [258] popularly categorized vibration-based damage detection into four levels involving *(i) detection,* which provides a qualitative indication of the existence of damage in a structure; *(ii) localization,* which determines the location of the damage detected in the first level; *(iii) assessment,* which identifies the severity or extent of the damage; and lastly (iv) *consequence,* which involves assessing the effect of the identified damage on structure's safety[6]. The first three levels have received the most attention in the published literature with the the fourth level being the least widely studied [282]. In earlier studies, the fourth level has commonly been treated as the residual service life of the structure in the context of prognostic evaluation. Such a treatment is perfectly suitable for aiding maintenance scheduling of replaceable

---

[6]Researchers have later added damage *classification* as a crucial process to understand the type of damage [281].

parts of equipments in a condition-based manner in, for instance, rotating machinery. However, in the context of civil engineering where every structure is one of a kind, a more practical treatment of Rytter's fourth level becomes estimating the damage-induced loss in load-carrying capacity.

Majority of the studies published on the use of vibration response features for estimating the reduction in load-carrying capacity were based on finite element (FE) model updating. For example, [283, 284] estimated the load-carrying capacity of a reinforced-concrete bridge deck by representing the effect of damage as reduced moment of inertia, the value of which was updated using measured natural frequencies of the damaged deck. This concept that involves the use of FE models updated against vibration measurements to calculate the load-carrying capacity has been applied in a number of recent studies on bridge structures [285–287] and masonry domes [181]. While the use of updated models is promising, its application on historic masonry monuments with complex geometries would be time-consuming, hard to automate and plagued with uncertainties due to poorly known model parameters.

Aside from these studies that use updated models, others have investigated the development of direct empirical relationships between natural frequencies and load carrying capacity for a given structure. For instance, [288] evaluated the relationship between the natural frequency and the applied load as the load was increased gradually until the failure for a small-scale masonry arch. Similarly, [289] observed that, upon monotonically increasing the back-fill load on a masonry arch, the natural frequency decreased until failure where sharp drops in natural frequency were correlated with crack formations. Developing such relationships, although helpful in relating easily measurable quantities such as natural frequency to the hard-to-measure load-carrying capacity, is plausible only for laboratory-scaled models. The need for destructive testing was bypassed by [181] through the use of updated FE models

for load carrying capacity estimation. Nevertheless, these empirically developed relationships may not guarantee uniqueness when damage is caused by factors other than the applied load. Non-uniqueness, here implies that similar loss in natural frequency may correspond to vastly different reductions in load-carrying capacity, which is demonstrated later in Section 5.3.1.

As seen, SHM research has been conceived to primarily address the first three levels of damage detection and the current capabilities are not amenable for strength assessment of full-scale historic masonry monuments. What is missing is a holistic treatment of strength estimation that is non-destructive and incorporates the nature of the SHM identified damage as well the nature of the operational load that the structure is expected to bear.

5.3 Redundancy Assessment based on Load Paths in Damaged Structures

After damage in a structure has been characterized according to the Rytter's first three levels of damage detection, the subsequent loss in load-carrying capacity must be predicted. This can be accomplished, for instance by performing a non-linear static analysis with load incremented until failure, or by establishing an empirical relation between an damage sensitive feature and the load-carrying capacity. The latter approach is more amenable to real-time long term health monitoring as it eliminates the necessity of performing a non-linear structural FE analysis each time a new instance of damage is characterized which in turn eliminates the need for expertise in non-linear modeling and powerful computing resources. Complicated non-linear simulations to estimate ultimate load are required only for developing the empirical relationships. Therefore, this study implements the later approach involving the development of an

empirical relationship and uses the concept of redundancy. Redundancy of a structure is the ability of the structure to assume alternate (i.e. sub-optimal) load paths to redistribute the loads after damage [273, 290–294]. Structural damage reduces the possible load paths, thus impairing redundancy. Loss in redundancy in turn leads to a loss in load-carrying capacity. Based on this association, the authors propose using a redundancy measure to estimate post-damage load-carrying capacity of a structure.

5.3.1 Role of load path in strength degradation due to damage

Let us consider a single bay frame shown in Figure 52 with a distributed load applied on one of its beams. The load carrying capacity of this frame will be analyzed under two hypothetical damage scenarios, one on the beam where the load is applied, which is directly within the load path of the system (referred to as damage scenario 1, DS_1) and one that is further away from the load on the opposite beam and not directly within the load path (referred to as damage scenario 2, DS_2). Here, damage is simulated by reducing the elastic modulus and the slopes of the strain hardening model by a factor of 10. For these two different damage scenarios, the load carrying capacity of the structure is computed as the load at which a sudden large vertical deformation occurs corresponding to a small increment in the load. From the load-deflection plots (Figure 52), the load carrying capacities are estimated as given in Table 4.

As seen in Table 4, damage scenario DS_1 results in a 50.6% loss in load-carrying capacity as opposed to a 2.5% loss resulting from DS_2. However, both damage cases result in an equal change in natural frequency of 10.9% when compared with the undamaged frame (Table 4). Hence, for this particular frame, a hypothetical vibration-based SHM campaign detecting approximately a 10% change in the first natural frequency could imply anywhere from an insignificant (2.5%) to a significant (50.6%)

103
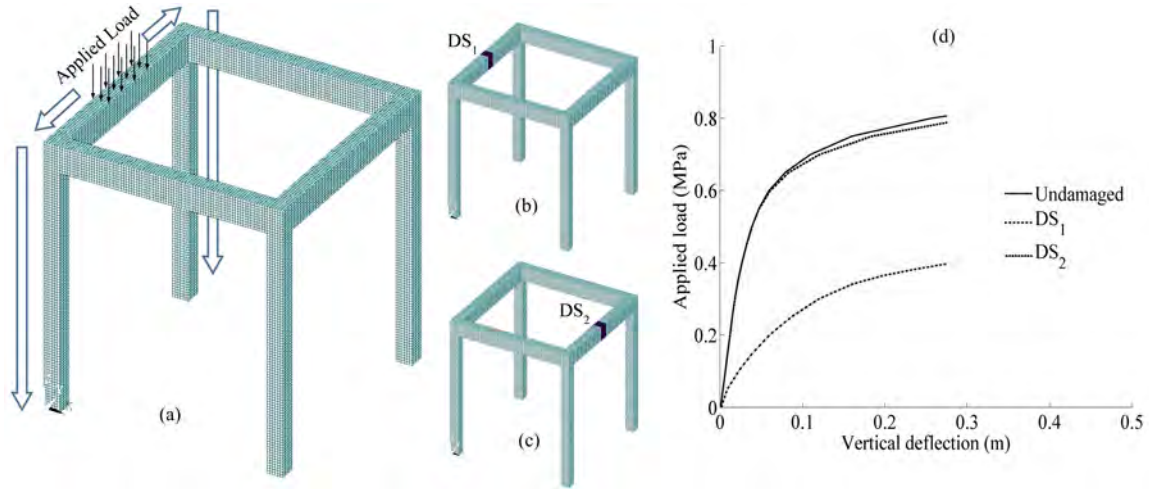
Figure 52: (a) FE model of the single-bay frame showing the location of the load and (b) damage scenarios DS1 and (c) DS2, and (d) the corresponding load-deflection plots.

	Load-carrying capacity (MPa)	Loss in load-carrying capacity (MPa)	Natural Frequency (Hz)
Undamaged	0.81	-	11.18
DS1	0.40	0.41(-50.6%)	10.05(-10.9%)
DS2	0.79	0.02(-2.5%)	10.05(-10.9%)

Table 4: Changes in the load-carrying capacity and first natural frequency between the undamaged and two damage scenarios.

loss in structural strength. Such dichotomy can be attributed to natural frequency being a global feature of the structure only accounting for loss in overall stiffness due to damage. As seen, an additional step to identify the actual impact of damage on structural integrity (Level 4: consequence, as Rytter [258] puts it) is essential to obtain meaningful information regarding the loss in load-carrying capacity. Such an identification must account for the relative location of the damage with respect to the applied loads.

5.3.2 Overview of existing redundancy measures

Several deterministic as well as probabilistic measures of structural redundancy have been proposed in published literature. Probabilistic measures of redundancy are employed when the damage itself is uncertain and must be treated as stochastic. For the purpose of strength assessment after having identified the damage, the authors limit this discussion to deterministic measures of static redundancy. For instance, [273] evaluated four measures of redundancy in trusses and bridges. The first was the static indeterminacy of the truss which was shown to be an inadequate measure of redundancy as the *importance* of each member in the load distribution is not accounted for:

$$R_1 = n_f - n_e \tag{9}$$

where n_f and n_e are the number of reactive forces and the number of equilibrium equations respectively. The next three redundancy measures in [273] were based on the load-carrying capacities of the intact (P_{intact}) and damaged ($P_{damaged}$) structure, given design load P_{design}:

$$R_2 = \frac{P_{ultimate}}{P_{design}} \tag{10}$$

$$R_3 = \frac{P_{damaged}}{P_{intact}} \tag{11}$$

$$R_4 = \frac{P_{intact}}{P_{intact} - P_{damaged}} = \frac{1}{1 - R_3} \tag{12}$$

where $P_{ultimate}$ is the ultimate load-carrying capacity of the structure. The measures of redundancy in Equations 10, 11 and 12 require the structure's load-carrying capacity to be computed, which defeats the goal of the present study of using redundancy measures to estimate the loss in load-carrying capacity.

[295] proposed a Redundancy-Strength index R_s as the ratio of load-carrying capacity of a structure to the load P_{yield} at which significant yielding of the overall structure occurs:

$$R_s = \frac{P_{ultimate}}{P_{yield}} \tag{13}$$

This redundancy measure is proposed as a representation of the ability of the structure to distribute loads from failed to intact members. The point of "significant yielding" is difficult to define for historic masonry monuments as the global ductility of unreinforced masonry structures is a result of several local brittle failures (see later Figure 60a). Also, similar to Equations 10, 11 and 12, this measure of redundancy requires calculation of $P_{ultimate}$, once again defeating the purpose of the present study.

[296] expressed redundancy of structures as being inversely proportional to the response sensitivity of the structure. Response sensitivity is a derivative of the structural response such as stress, strain, displacement, etc. with respect to a damage

parameter (for instance, the reduced material strength property or volume/area of the elements after damage). It is, however, not demonstrated how this redundancy measure relates to the ultimate load-carrying capacity of the structure. Nevertheless, this sensitivity-based approach comes closest to the approach proposed in this chapter as it demonstrates sensitivity to the distribution of forces within the structure.

5.3.3   Redundancy measure based on load paths

Applied loads on a continuous structure get distributed throughout the volume of the structure to reach the supports. However, some regions within the structure bear more load than other regions [297]. Load path defines the region within the structure that bears a higher portion of the load and thus, may be thought of as the trajectory of the applied load from the point of application to the supports [298]. This definition is reminiscent of the topology optimization problem in which, the optimal distribution of material between the load and the supports is sought [299, 300]. If we consider the load path as analogous to the optimal topology, any removal of material from this optimal topology would require an alternative sub-optimal topology to be found. This sub-optimal topology, however would provide a reduced, sub-optimal minimum compliance. Similarly, in existing structures, a disturbance in the primary load path due to the onset of damage would force the structure to assume a sub-optimal, alternative load path with a reduced (or equal) capacity to carry the loads. The challenge here is to calculate this damage-induced change in load path in a manner that is indicative of the loss in the structure's load-carrying capacity, which is precisely the goal of this chapter.

Here, the loss in structural redundancy is defined as the extent by which the primary load path in the intact structure is disturbed by damage. In this context, the primary load path is the trajectory of the operational load (i.e. loading of interest

under which structural integrity is to be determined) in the structure's undamaged state. Assuming a fixed mode of failure under a given operational load, the redundancy of a structure can be quantified as the maximum disturbance in load path that can be tolerated by means of load redistribution (i.e. damage tolerance). Structural damage adversely affects this redundancy at an extent that is governed by the location of the damage with respect to the load path.

In this study, the load path for a given load is quantified from the internal force distribution. Using the FE model, resultant force vectors at each node (i.e., integration points) are calculated from the nodal stress outputs. The arbitrary plane along which the force vectors are to be resolved is given by the normal vector $\vec{n}$:

$$\vec{n} = \begin{Bmatrix} n_x \\ n_y \\ n_z \end{Bmatrix} \tag{14}$$

The arbitrary plane $\vec{n}$ can represent, for instance, the plane of cracking in masonry, across which tensile forces cannot be transferred. The stress tensor at each node in the FE model is obtained by applying a small magnitude of operational load of interest. In this step, it is important that the stress tensor only includes stresses that are solely due to the applied operational loads under which the load carrying capacity is evaluated. The force vectors at each node in the arbitrary plane are then given by:

$$F_x = \sigma_{xx} A n_x + \tau_{xy} A n_y + \tau_{xz} A n_z \tag{15}$$

$$F_y = \tau_{xy} A n_x + \sigma_{yy} A n_y + \tau_{yz} A n_z \tag{16}$$

$$F_z = \tau_{xz}An_x + \tau_{yz}An_y + \sigma_{zz}An_z \qquad (17)$$

where A is the integration area of the node in the arbitrary plan that is the area over which the nodal stresses are integrated to obtain nodal forces. The change in load paths ΔF_d due to damage in region Ω_d in the structural domain Ω, is quantified as the sum of forces in Ω_d (see Figure 53). ΔF_d thus represents the forces that must be redistributed since the damaged region is no longer capable of force transmission.

$$\Delta F_d = \sum F_i \ \forall i \in \Omega_d \qquad (18)$$

In this study, for damage that is in the form of cracks, only the tensile forces are considered in the constitution of ΔF_d and, the compression forces and shear forces are accepted to be transferred across cracked elements. Thus, if tensile forces are taken as positive,

$$\Delta F_d = \sum F_i \ \forall i \in \Omega_d \,, \ F_i > 0 \qquad (19)$$

As regions critical to load transfer bear a larger force distribution, damage in these critical regions yields a higher ΔF_d. If given operational load is incremented up to failure, the corresponding change in load path ΔF_u would reflect the change in load path due both to the initial damage Ω_d and the damage caused by the operational load itself Ω_p, where the ultimate damage that causes structural failure can be approximated as $\Omega_u = \Omega_d + \Omega_p$:

$$\Delta F_u = \Delta F_d + \Delta F_p \qquad (20)$$

In Equation 20, ΔF_p is the change in load path resulting from the damage caused

by the operational load itself. Here, it is assumed that, under a given operational load, the maximum change in load path i.e. ΔF_u is irrespective of the initial damage. This assumption is reasonable if that initial damage does not alter the ultimate failure mode under operational load. Thus, having knowledge of ΔF_u and ΔF_d provides an estimation of $\Delta F_p = \Delta F_u - \Delta F_d$ which is the further load path disturbance that can be tolerated by means of load redistribution by the structure after the occurrence of initial damage.

Here, the ΔF_p is used for estimating structural redundancy effectively incorporating the relative importance of damage with respect to the operational load. Specifically, redundancy is calculated in this study as the ratio of the capacity of the damaged structure to tolerate change in load path (i.e. damage tolerance) to the maximum possible change in load path before collapse:

$$R = \frac{\Delta F_p}{\Delta F_u} \tag{21}$$

In this treatment, the loss in redundancy becomes proportional to the magnitude of the force that the damaged region was bearing prior to damage. If damage occurs in a region with a higher force distribution, then the corresponding loss in redundancy is greater. Hence, the value of R can take any value between 0 and 1. If, on the other hand, the structure is intact, $\Delta F_p = \Delta F_u$ which gives $R = 1$. If the structure is incapable of carrying the operational load, $\Delta F_p = 0$ and therefore $R = 0$. In the following section, the proposed redundancy measure is illustrated on a numerical model of a historic monument to assess its capability in estimating the load-carrying capacity.
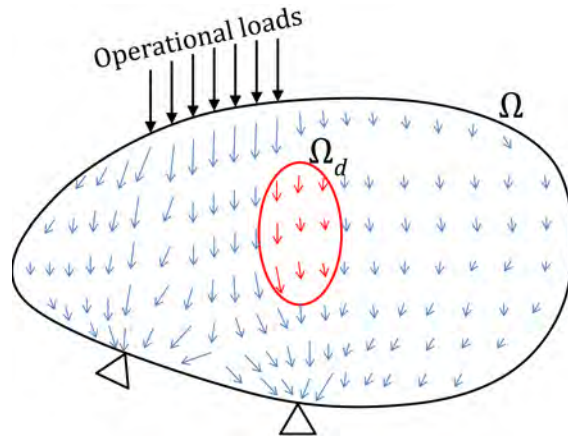
Figure 53: Force vectors enclosed by damaged region Ω_d constitute the change in load path due to the damage.

5.4 Case-study: Fort Sumter Coastal Fortification

Fort Sumter is a 19$^{\text{th}}$ coastal fortification in Charleston, South Carolina, best known for being the site of the first battle of the American Civil War in 1861. The pentagonal brick masonry fort is comprised of a number of vaulted casemates as shown in Figure 54. The fort stands on a man-made island which has been experiencing gradual differential settlement over more than 150 years. Understanding the degrading effects of the existing and future damage in the forms of cracks in the vaults and arches caused by such foundation settlement on the structural integrity of the fort is necessary to plan and justify future rehabilitation and retrofitting activities. In this study, using an FE model of Fort Sumter casemate, the natural frequency and load-carrying capacity of one of the fort's casemates are estimated and contrasted at incremental levels of damage resulting from foundation settlement.

5.5 FE Model Development and Settlement Simulation

The FE model of Fort Sumter is developed in ANSYS v14.0 (Figure 55) with the casemate geometry obtained from three-dimensional laser scans and material prop-

Figure 54: System of casemates at Fort Sumter showing (a) the Right face and (b) the Left flank of the fort.

erties obtained from tests performed on core samples from the fort's exterior walls (Table 5). Details of data-collection and model development can be found in [69].

The masonry material is represented with the SOLID65 element [161], a three-dimensional solid iso-parametric 8-noded element that is specially formulated to model concrete-like brittle materials [181,301–303]. SOLID65 represents the cracking as a smeared crack [304] where the crack is modeled as reduction in the stiffness of the cracked elements while maintaining continuum. The failure surface is defined by the ultimate uniaxial tensile strength f_t and ultimate uniaxial compressive strength f_c (Table 5).

Figure 55 shows the FE model of one of the Fort Sumter casemates. In this model, lateral restraining effects from the adjacent casemates are modeled using substructures, meaning that the FE models of the adjacent casemates are condensed down to a small number of interface degrees of freedom shared between the casemates (see Figure 55). To further reduce the number of degrees of freedom that needs to be analyzed, the fort's external scarp wall, which is structurally detached from the casemates, is omitted in the simulations as the behavior of interest is found not to be
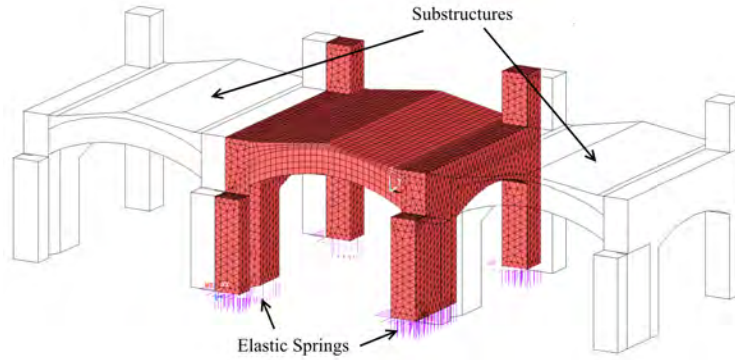
Figure 55: Meshed FE model of the casemate of Fort Sumter showing the substructures and the foundation springs.

Material Property	Property Value
Elastic Modulus	0.8 GPa
Poisson's Ratio	0.2
Ultimate uniaxial tensile strength	0.2 MPa
Ultimate uniaxial compressive strength	4 MPa
Open shear transfer coefficient	0.5
Closed shear transfer coefficient	0.9

Table 5: Material properties used for masonry.

significantly affected by the scarp wall. Semi-rigid supports are modeled with a total of 225 linear elastic springs (COMBIN14 element) with a stiffness constant of 60 MN/m at the base nodes of the piers [69].

Structural damage due to differential settlement between the North and South piers of the casemate is evaluated as shown in Figure 56. A total of 11 settlement magnitudes, δ from 0 m to 0.1 m in increments of 0.01 m are applied at the two South piers. Natural frequency and load-carrying capacity of the casemate are estimated for each of these 11 settlement scenarios.

The developed FE model incorporates two sources of non-linearity, i.e. material non-linearity (smeared cracking and multi-linear material model) and geometric non-linearity ($P - \Delta$ effects). A Newton-Rhapson iterative scheme is used to update the

113
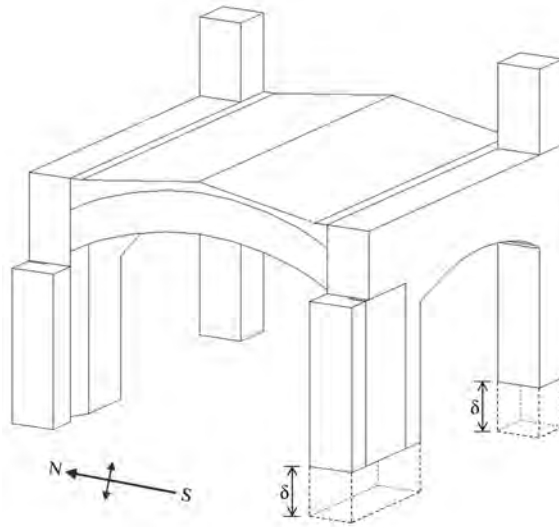
Figure 56: Differential settlement under the piers.

tangent matrix and internal force vectors at each iteration. Support settlement is applied gradually with the automatic time-stepping selecting an appropriate settlement increment to ensure convergence. Convergence criteria are specified on both the force vector (0.1% L-2 norm) and displacement vector (5% L-infinity norm), and are relaxed, if needed, to enable convergence.

Figure 57 shows the crack patterns predicted for six of the 11 settlement scenarios. With 0.02 m settlement, cracks form at the intrados of the vault over the South piers and at the extrados over the North piers. At 0.04 m and 0.06 m settlement levels, the same cracks expand without formation of new cracks. A new crack spanning across the vault develops at 0.08 m settlement. At 0.1 m settlement, the vault has several cracks across the span. These crack patterns represent Ω_d as described in Section 5.3.2.
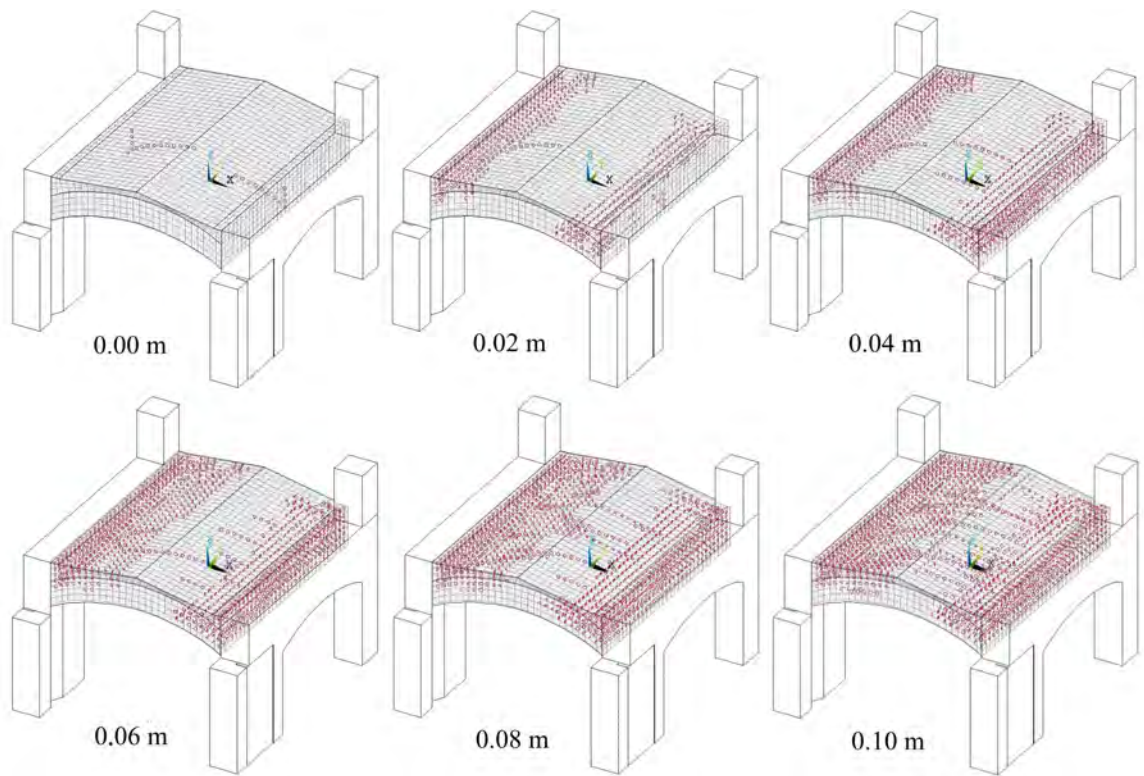
Figure 57: Predicted crack patterns in the casemate vaults resulting from settlement.
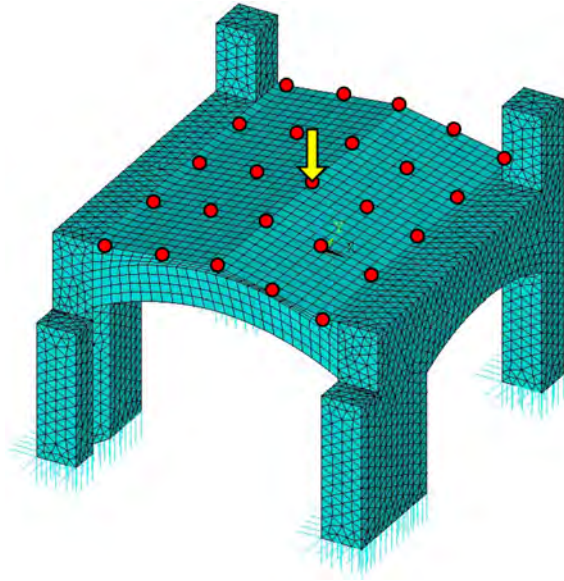
Figure 58: 25 measurement locations (circles) and impact force location (arrow) on the FE model.

5.6 Missing link between $\Delta\omega$ and ΔP

The changes in the natural frequencies, as the casemates are damaged in these 11 settlement scenarios, are determined through transient dynamic analysis, where the vibration response of the casemate is simulated under a fictitious hammer impact load. The transient analysis takes the non-linear effects due to the presence of cracks as well as the effect of opening and closing of cracks under vibration into account and hence is preferable over an eigenvalue analysis.

An impact force of 10 KN is applied as a ramped force at the center of the vault (Figure 58) without causing local crushing under the impact. The impact duration is set as 0.01 sec allowing an input frequency spectrum of 0-100 Hz and a Nyquist frequency of 50 Hz. The time-domain free vibration response (displacements in the vertical direction) is extracted at 25 measurement points (as shown in Figure 58) for 3 sec after impact with a sampling rate of 2000 Hz (i.e. time-resolution of 0.5 milliseconds).

Settlement (m)	1$^{\text{st}}$ mode	2$^{\text{nd}}$ mode
0	12.88	28.95
0.01	12.82	28.87
0.02	11.44	26.43
0.03	10.76	25.37
0.04	10.00	19.16
0.05	9.42	20.07
0.06	8.65	21.09
0.07	8.39	19.12
0.08	8.06	18.19
0.09	7.73	17.96
0.10	7.69	17.47

Table 6: First two natural frequencies of the casemate with incremental damage.

The calculated time-domain displacement response is first artificially damped and next, transformed into the frequency domain via Fast Fourier transform. The resulting frequency domain representation of the vibration response for each of the 25 measurement points are then used to identify the the natural frequencies. Figure 59a shows the cumulative frequency response summed over the 25 measurement points for increasing levels of settlement. The first peak of the cumulative frequency response function corresponds to the 1$^{\text{st}}$ natural frequency.

First two natural frequencies obtained using the rational fraction polynomial method [305] are listed in Table 6. The percentage change in the two natural frequencies $\Delta\omega$ with respect to the undamaged case (i.e. 0 m settlement), shown in Figure 59b, can be considered as a damage indicative features as was done in many of the earlier studies. The 1$^{\text{st}}$ natural frequency monotonically decreases with increasing settlement levels 59b, signifying a reduction in global stiffness. The second natural frequency however exhibits an uneven trend between 0.03 m and 0.06 m settlements which may lead to false positives (or false negatives) in damage identification (note that the $\Delta\omega$ corresponding to 0.04 m settlement is equal to $\Delta\omega$ for 0.07 m settlement).
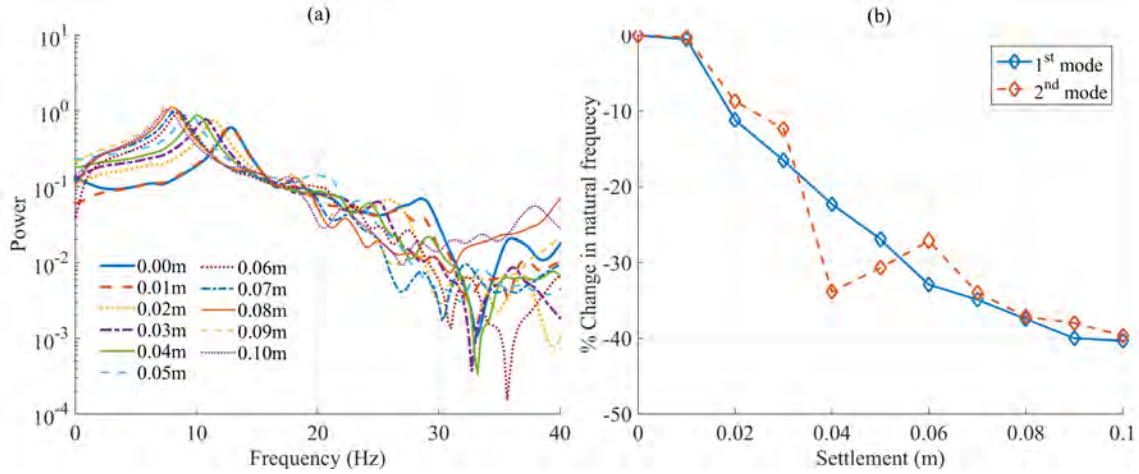
Figure 59: (a) Cumulative frequency response functions obtained from impact hammer simulations for increasing settlement; (b) Change in the 1st and 2nd resonant frequency for increasing settlement.

The operational load is taken to be uniformly distributed pressure of 0.5 MPa across the top of the vault. This operational load is gradually increased until the vault fails to estimate how much load-carrying capacity ΔP is lost due to initial damage from settlement. Here, load-carrying capacity is defined as the load at which vault's average vertical displacement shows a sudden increase for a relatively small increase in load. Such a sharp increase correlates to a hinge formation in the vault after which the structure achieves a new equilibrium with a significantly reduced stiffness.

The simulation is divided into two load-steps: In the first load step, the piers are settled while in the second load-step, the operational load is applied and the vault's vertical deformation is recorded. Figure 60a shows the calculated vertical deformation averaged over all the nodes in the vault plotted against the gradually increased operational load. Considering 0 m settlement case as undamaged, Figure 60b plots the relative loss in load-carrying capacity for increasing settlement damage. A generally decreasing trend in ΔP with increasing settlement is evident in Figure

118
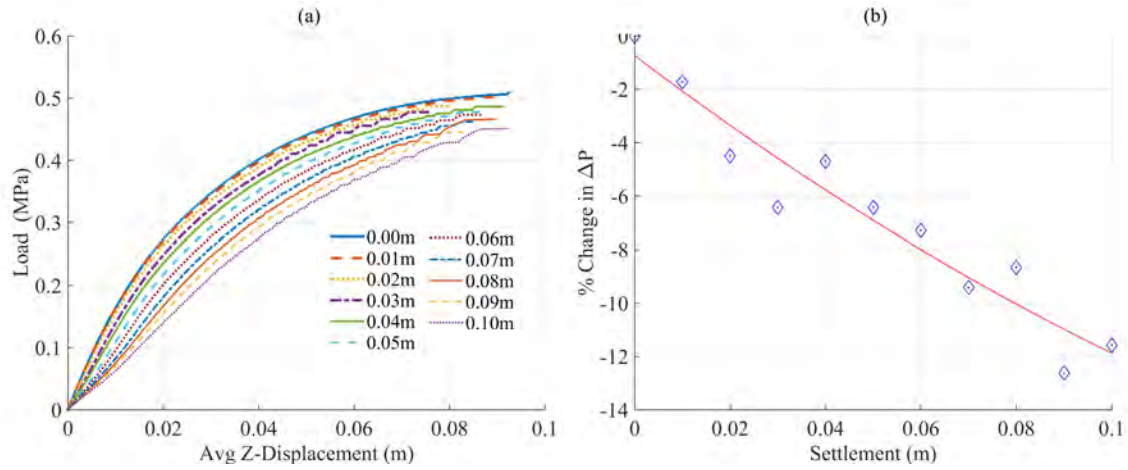
Figure 60: (a) Average displacement in the vault vs. the applied uniformly distributed load and (b) change in the load carrying capacity with incremental settlement.

60b.

5.7 Load Path Assessment

Figure 61 shows internal force vectors at the FE nodes in the vault acting in the plane perpendicular to the X-direction due to the operational load only meaning that stresses due to self-weight of the casemate are subtracted. The cracks denote the damaged region Ω_d and are determined using the crack status provided by SOLID65 elements at each element's integration points (i.e. the the angle of the cracking planes). Note that the applied load is the same operational load applied for estimation of ΔP.

ΔF_d is calculated by summing the tensile forces normal to the crack plane at all integration points of the cracked elements as explained in Section 5.3.2. Compressive and shear forces are not included in ΔF_d since they are assumed to be transferred across a cracks. ΔF_u is calculated similarly using the failure load (see Figure 60a) where the damage Ω_u includes Ω_p due to the applied load in addition to Ω_d.

Figure 62a plots ΔF_d, ΔF_p and ΔF_u for increasing levels of settlement damage.

119

As expected, ΔF_d increases monotonically as cracked region Ω_d expands due to increasing settlement. Also note that ΔF_u remains approximately constant for all levels of settlement, which indicates that the total change in load path that causes failure remains insensitive to the initial damage Ω_d in the system. Thus, the remaining load-carrying capacity can be related to the further load path disturbance ΔF_p that can be tolerated before structure fails. Figure 62b represents an empirical relation approximating loss in load-carrying capacity ΔP as functions of ΔF_d or ΔF_p. These relations are specific to the structure and, once established through the use of computer models, can be used to estimate the loss in strength corresponding to damage identified via SHM. Figure 63 plots the redundancy measure R (Eq. 21) as a function of the loss in load carrying capacity of the casemate.

5.8 Conclusions

Non-destructively obtained vibration features, although have proven to be indicators of onset and progression of damage, provide little to no information about the effect of the identified damage on the structure's integrity in terms of its ability to carry the expected operational loads. These stiffness based features also suffer from non-uniqueness as a given degradation in stiffness may indicate anywhere from a severe to negligible degradation in strength.

Structural strength is related to a structure's redundancy, which can be defined as the ability to assume alternative load paths that can safely transfer the applied load to the supports. Typically, higher the redundancy, higher is the structure's load-carrying capacity. Damage in the structure degrades this redundancy by reducing the number of possible alternative load paths. Based on this principle, the authors propose a redundancy measure for estimating post-damage strength degradation by
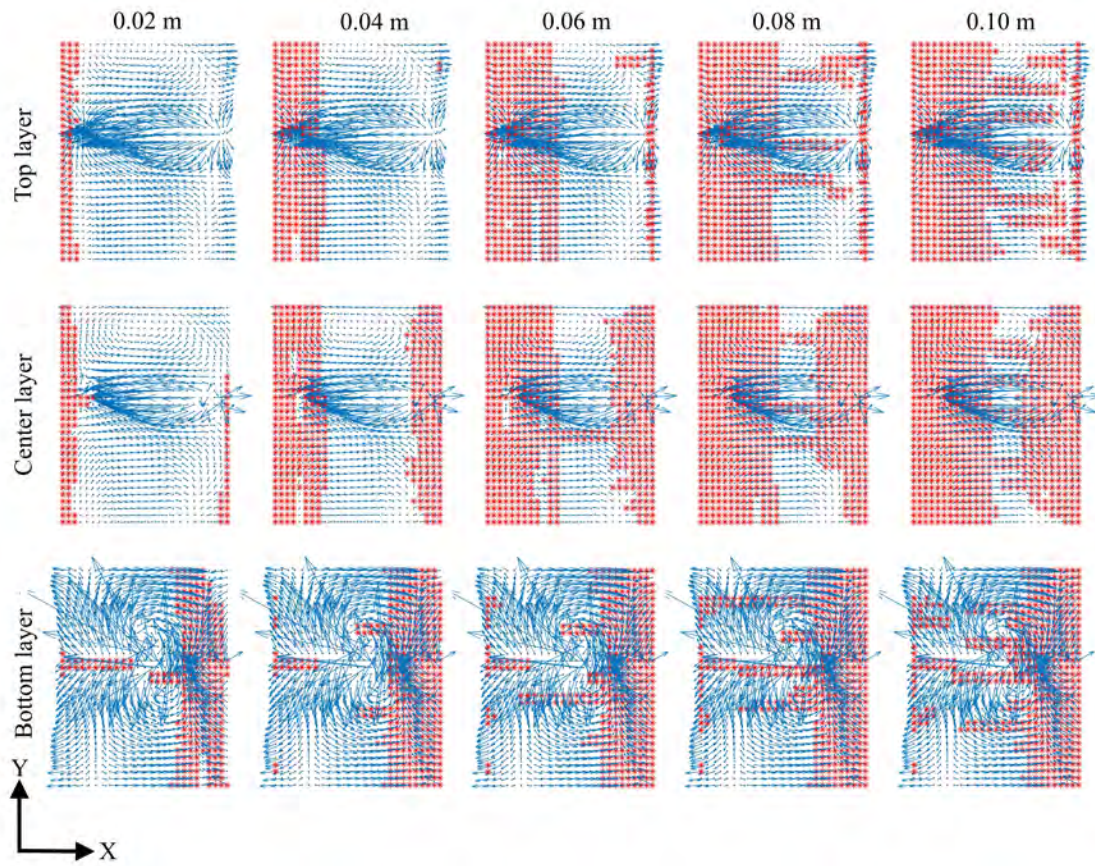
Figure 61: Force vectors at nodes in the vault divided into three layers for visualization purposes, with corresponding cracks are overlaid. Size of the arrows proportional to the magnitude of the force. Cracked nodes corresponding to applied settlement form the region of damage Ω_d.
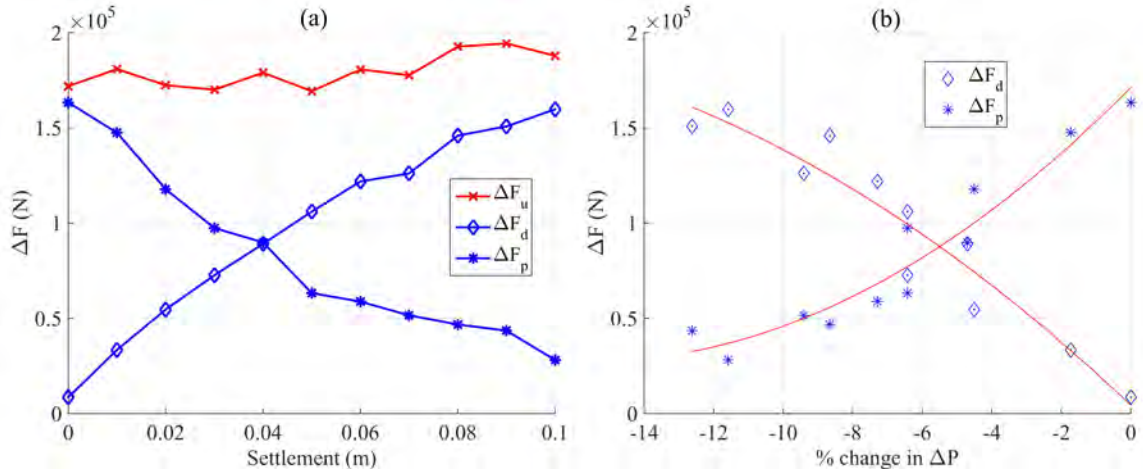
Figure 62: (a)ΔF_d and ΔF_u with increasing applied settlement; (b) ΔF_d as a function of change in load-carrying capacity ΔP
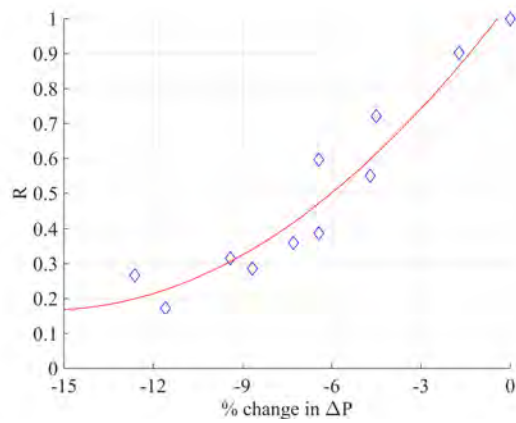
Figure 63: Redundancy measure R as a function of ΔP.

quantifying the how much a given damage disturbs load paths. This redundancy measure effectively accounts for the position of the damage with respect to the given operational loads.

A core assumption behind the proposed redundancy measure is that the failure mode of the structure under the operational load of interest remains constant regardless of the initial structural damage. Thus, empirical relationships between redundancy and load-carrying capacity becomes specific to the nature of the operational load itself. Thus, when several possible operational load configurations are of interest, individual empirical relationships must be developed for each configuration. The use of computer models allows developing these relationships by identifying all combinations of plausible loads as well as damage scenarios. In this chapter, the authors have demonstrated the development of such a relationship for a full-scale historic monument with a specific focus on one type of support settlement scenario.

6   CONCLUSIONS

6.1   Summary of Research

With the exponential advancement in computational power, numerical modeling has become the preferred means for structural for design of new structures as well as analysis of existing structures. Input parameters in these structural models are most often uncertain in nature. These input parameters can assume a range of possible values which can result in a range of possible model outcomes for a given load scenario. Thus, for the model to be useful for predicting structural response, the predictions must be satisfactory given the hard-to-control uncertainty in the input parameters.

The process of model calibration finds the input parameter realization that minimizes the error between the model prediction and the corresponding experimental measurement. Since variability in the properties of the structure is inevitable, the calibrated model must show robustness to the resulting uncertainty in the input parameters that define these properties. Higher this uncertainty, higher will be the error between the model predictions and observed reality, i.e. the truth. The concept of satisfying boundary, introduced in Chapter 3 investigates this trade-off between the amount of uncertainty in the parameters and the error in prediction with respect to the truth. By studying this trade-off, a model developer can make decisions regarding allocation of available resource. The model developer may chose to invest in reducing parametric uncertainty by obtaining more information by performing more experiments. Or, the model developer may decide to tolerate a higher error in prediction depending on the consequences of error and/or on the experimental uncertainty involved in defining the truth itself. A measure of the model's confidence is also analyzed in the trade-off, which is the probability that the model can perform satisfactorily at a given level of error tolerance.

In Chapter 4, an FE model of a historic masonry monument, Fort Sumter, is developed outlining the entire process from on-site data collection to calibration of uncertain material properties and support conditions. The geometry is obtained via laser scanning, material properties are obtained by lab test on specimen collected on-site and modal data is obtained by performing ambient vibration tests. The material properties that are uncertain even after lab tests and the hard-to-measure support conditions are calibrated to the experimental modal data. Even after calibration, uncertainty still remains in the calibrated parameters. The robustness of the model in making predictions under settlement is analyzed using the satisfying boundary concept. The model is then used for making predictions of structural response to several plausible settlement scenarios by looking at crack formation and propagation in the masonry.

Finally, Chapter 5 presents a novel measure of loss in structural redundancy due to structural damage, which is based on change in internal load paths between the load and the supports. The driving principle of the redundancy measure is that damage alters the load paths, which are essentially trajectories of the load between point of applications and the support. Structural damage reduces the number of such possible load paths, thus reducing the redundancy of the structure and, in turn, the structure's load-carrying capacity.

6.2 Major Findings of the Research

Following are the major findings of the presented research

Chapter 3: The Concept of Satisfying Boundary

Applying the satisfying boundary concept to proper continuous functions, the trade-off between amount of parametric uncertainty and allowable error in model predictions is obtained. The third criteria introduced is the probability of success, which is a measure of the confidence in predictions satisfying given error tolerances.

The shape of the satisfying boundary depicts the sensitivity of the output to the uncertain parameters. With this knowledge, the model developer can decide which parameters to focus on in further experimentation to reduce uncertainty.

Several existing model evaluation criteria become special cases of using the satisfying boundary analysis. The deterministic optimal design is obtained when error tolerance is set to zero. Info-gap robustness is obtained when the probability of satisfying is set to one.

Adding experimental outcomes to generate satisfying boundaries can lead to reduction in calculated robustness due to the reduction in the probability of satisfying error tolerances for additional model outputs. Thus, while choosing features and experimental observations for model correlation, one must establish all the purposes for which the model is expected to be used.

Chapter 4: Modeling and Simulation of Fort Sumter

Large variability of nearly 60% in seen in some of the measured material properties of the building material of Fort Sumter. This shows the importance of treating the input parameters that define the material properties as uncertain. Although homogenization of material is necessary from practical viewpoint, one must be careful in using the predictions of damage which may be underestimated if variability in input parameters is ignored.

Propagating the uncertainty in two of the uncertain input parameters shows the consequences of ignoring parameter uncertainty in making predictions. Ignoring the large variability (nearly 30%) in the strain output can lead to catastrophic consequences.

At higher settlement levels, when the structure becomes severely cracked and the response becomes highly non-linear, the relation between the uncertain input parameters and outputs of interest begin violating proper continuous behavior. Thus, the use of satisfying boundary concept at this load level becomes invalid.

Chapter 5: Assessment of Strength Degradation due to Damage using a Load Path based Approach

Non destructively obtained features, although indicative of loss in structural stiffness due to damage, cannot indicate the consequent loss in structural strength. This is because non-destructive measurements do not consider the damage in the context of the applied load. A given loss in stiffness could signify anywhere from negligible to total loss in the structure's load-carrying capacity, depending on the applied load.

Based on the principle that damage alters the internal load paths in the structure, a redundancy measure based on change in load paths effectively accounts for the position of damage with respect to the applied loads. It is found that the total allowable loss in redundancy prior to structural collapse remain constant for a given load configuration. Exploring this notion, the loss in load-carrying capacity due to damage can be related to the loss in total redundancy. This relation is specific to each load configuration.

6.3 Limitations and Recommendations for Future Research

The concept of satisfying boundaries is devised for proper continuous input-output relations. In many practical engineering problems, however, this assumption is not satisfied as seen at higher settlement levels in the case study FE model in Chapter 4. Such cases result in an inaccurate quantification of robustness. Further research can expand the satisfying boundary concept to problems that do not meet proper continuous input-output behavior.

Satisfying boundary concept can be adapted for robust optimization, which aims to maximize robustness of design given certain performance error tolerances. The goal is to find the input parameter realization within the uncertain input space that maximizes the design robustness.

Objective techniques to establish adequacy criteria in terms of error tolerance and probability of satisfying need to be devised considering experimental uncertainty. Moreover, the consequence of failure or replacement cost is an important factor for selecting the error tolerance. For instance, certain components of a larger system may have a lower consequence of failure compared to more critical components. Thus, concepts from the field of risk and vulnerability assessment can be incorporated with the satisfying boundary concept to widen the horizon of applications.

Model form error is another issue that deserves attention as biased model outputs can lead to overestimation or underestimation of model error.

As the number of input parameters increases, the generation of boundary surface becomes increasingly computationally intensive. In this dissertation, the satisfying boundary is defined by a discrete set of points in the input space without assuming a functional form. In presence of a larger number of input parameters, assuming a functional form for the satisfying boundary can ease computational demand.

References

[1] R. P. Feynman and R. Leighton, *" What do you care what other people think?":
further adventures of a curious character.* WW Norton & Company, 1988.

[2] I. Elishakoff, "Essay on uncertainties in elastic and viscoelastic structures: from
am freudenthal's criticisms to modern convex modeling," *Computers and Struc-
tures*, vol. 56, no. 6, pp. 871–895, 1995.

[3] D. Draper, "Assessment and propagation of model uncertainty," *Journal of the
Royal Statistical Society. Series B (Methodological)*, pp. 45–97, 1995.

[4] T. Wagener and H. V. Gupta, "Model identification for hydrological forecasting
under uncertainty," *Stochastic Environmental Research and Risk Assessment*,
vol. 19, no. 6, pp. 378–387, 2005.

[5] G. E. Box, "Robustness in the strategy of scientific model building," *Robustness
in statistics*, vol. 1, pp. 201–236, 1979.

[6] J. M. Carlson and J. Doyle, "Complexity and robustness," *Proceedings of the
National Academy of Sciences*, vol. 99, no. suppl 1, pp. 2538–2545, 2002.

[7] F. M. Hemez, "The myth of science-based predictive modeling," *Foundations*,
pp. 13–15, 2004.

[8] Y. Ben-Haim and F. M. Hemez, "Robustness, fidelity and prediction-looseness
of models," in *Proceedings of the Royal Society of London A: Mathematical,
Physical and Engineering Sciences*, vol. 468, no. 2137. The Royal Society,
2012, pp. 227–244.

[9] D. Bertsimas and M. Sim, "The price of robustness," *Operations research*, vol. 52, no. 1, pp. 35–53, 2004.

[10] G. Maier, M. Bocciarelli, G. Bolzon, and R. Fedele, "Inverse analyses in fracture mechanics," in *Advances in Fracture Research*. Springer, 2006, pp. 47–73.

[11] G. Stavroulakis, G. Bolzon, Z. Waszczyszyn, and L. Ziemianski, "Inverse analysis," *Comprehensive structural integrity*, vol. 3, pp. 685–718, 2003.

[12] L. Ljung, *System identification*. Springer, 1998.

[13] M. Fontan, A. Ndiaye, D. Breysse, and P. Castéra, "Inverse analysis in civil engineering: applications to identification of parameters and design of structural material using mono or multi-objective particle swarm optimization," *Theory and New Applications of Swarm Intelligence*, 2012.

[14] M. Ratto, S. Tarantola, and A. Saltelli, "Sensitivity analysis in model calibration: Gsa-glue approach," *Computer Physics Communications*, vol. 136, no. 3, pp. 212–224, 2001.

[15] D. Higdon, J. Gattiker, B. Williams, and M. Rightley, "Computer model calibration using high-dimensional output," *Journal of the American Statistical Association*, vol. 103, no. 482, 2008.

[16] A. Ben-Tal and A. Nemirovski, "Robust optimization-methodology and applications," *Mathematical Programming*, vol. 92, no. 3, pp. 453–480, 2002.

[17] L. E. Gulden, E. Rosero, Z.-L. Yang, T. Wagener, and G.-Y. Niu, "Model performance, model robustness, and model fitness scores: A new method for identifying good land-surface models," *Geophysical Research Letters*, vol. 35, no. 11, 2008.

[18] S. Atamturktur, Z. Liu, S. Cogan, and H. Juang, "Calibration of imprecise and inaccurate numerical models considering fidelity and robustness: a multi-objective optimization-based approach," *Structural and Multidisciplinary Optimization*, pp. 1–13, 2014.

[19] G. M. Gladwell, "Inverse problems in vibration-ii," *Applied Mechanics Reviews*, vol. 49, no. 10S, pp. S25–S34, 1996.

[20] S. Kubo, "Inverse analyses and their applications to nondestructive evaluations," in *Proc. 12th A-PCNDT 2006–Asia-Pacific Conference on NDT*, 2006.

[21] G.-R. Liu and X. Han, *Computational inverse techniques in nondestructive evaluation*. CRC press, 2003.

[22] J. Mottershead and M. Friswell, "Model updating in structural dynamics: a survey," *Journal of sound and vibration*, vol. 167, no. 2, pp. 347–375, 1993.

[23] J. M. Brownjohn, P.-Q. Xia, H. Hao, and Y. Xia, "Civil structure condition assessment by fe model updating:: methodology and case studies," *Finite Elements in Analysis and Design*, vol. 37, no. 10, pp. 761–775, 2001.

[24] B. Jaishi and W.-X. Ren, "Structural finite element model updating using ambient vibration test results," *Journal of Structural Engineering*, vol. 131, no. 4, pp. 617–628, 2005.

[25] S. Atamturktur and J. A. Laman, "Finite element model correlation and calibration of historic masonry monuments: review," *The Structural Design of Tall and Special Buildings*, vol. 21, no. 2, pp. 96–113, 2012.

[26] R. Mahnken and E. Stein, "A unified approach for parameter identification of inelastic material models in the frame of the finite element method," *Computer*

methods in applied mechanics and engineering, vol. 136, no. 3, pp. 225–258, 1996.

[27] R. Fedele and G. Maier, "Flat-jack tests and inverse analysis for the identification of stress states and elastic properties in concrete dams," *Meccanica*, vol. 42, no. 4, pp. 387–402, 2007.

[28] C. Hsein Juang, Z. Luo, S. Atamturktur, and H. Huang, "Bayesian updating of soil parameters for braced excavations using field observations," *Journal of Geotechnical and Geoenvironmental Engineering*, vol. 139, no. 3, pp. 395–406, 2012.

[29] Y. Robert-Nicoud, B. Raphael, O. Burdet, and I. Smith, "Model identification of bridges using measurement data," *Computer-Aided Civil and Infrastructure Engineering*, vol. 20, no. 2, pp. 118–131, 2005.

[30] H. S. Atamturktur, F. M. Hemez, C. Unal, and B. J. Williams, "Verification and validation under uncertainty applied to finite element models of historic masonry monuments," Los Alamos National Laboratory (LANL), Tech. Rep., 2008.

[31] A. Teughels and G. De Roeck, "Structural damage identification of the highway bridge z24 by fe model updating," *Journal of Sound and Vibration*, vol. 278, no. 3, pp. 589–610, 2004.

[32] G. Maier, R. Ardito, and R. Fedele, "Inverse analysis problems in structural engineering of concrete dams," in *6th World Conference of Computational Mechanics WCCM VI, Beijing (China)*, 2004.

[33] C. K. Soh and Y. X. Dong, "Evolutionary programming for inverse problems in civil engineering," *Journal of computing in civil engineering*, vol. 15, no. 2, pp. 144–150, 2001.

[34] K. Hjelmstad and S. Shin, "Damage detection and assessment of structures from static response," *Journal of Engineering Mechanics*, vol. 123, no. 6, pp. 568–576, 1997.

[35] M. R. Banan, M. R. Banan, and K. Hjelmstad, "Parameter estimation of structures from static response. i. computational aspects," *Journal of Structural Engineering*, vol. 120, no. 11, pp. 3243–3258, 1994.

[36] M. Sanayei and O. Onipede, "Damage assessment of structures using static test data," *AIAA journal*, vol. 29, no. 7, pp. 1174–1179, 1991.

[37] R. Ruotolo and C. Surace, "Damage assessment of multiple cracked beams: numerical results and experimental validation," *Journal of Sound and Vibration*, vol. 206, no. 4, pp. 567–588, 1997.

[38] S. W. Doebling, C. R. Farrar, M. B. Prime *et al.*, "A summary review of vibration-based damage identification methods," *Shock and vibration digest*, vol. 30, no. 2, pp. 91–105, 1998.

[39] A. Teughels, J. Maeck, and G. De Roeck, "Damage assessment by fe model updating using damage functions," *Computers & structures*, vol. 80, no. 25, pp. 1869–1879, 2002.

[40] B. Jaishi and W.-X. Ren, "Damage detection by finite element model updating using modal flexibility residual," *Journal of sound and vibration*, vol. 290, no. 1, pp. 369–387, 2006.

[41] M. I. Friswell, "Damage identification using inverse methods," *Philosophical Transactions of the Royal Society of London A: Mathematical, Physical and Engineering Sciences*, vol. 365, no. 1851, pp. 393–410, 2007.

[42] J. Doyle, "Experimentally determining the contact force during the transverse impact of an orthotropic plate," *Journal of Sound and Vibration*, vol. 118, no. 3, pp. 441–448, 1987.

[43] C.-S. Yen and E. Wu, "On the inverse problem of rectangular plates subjected to elastic impact, part i: Method development and numerical verification," *Journal of Applied Mechanics*, vol. 62, no. 3, pp. 692–698, 1995.

[44] E. Jacquelin, A. Bennani, and P. Hamelin, "Force reconstruction: analysis and regularization of a deconvolution problem," *Journal of Sound and Vibration*, vol. 265, no. 1, pp. 81–107, 2003.

[45] F. E. Gunawan, H. Homma, and Y. Kanto, "Two-step b-splines regularization method for solving an ill-posed problem of impact-force reconstruction," *Journal of Sound and Vibration*, vol. 297, no. 1, pp. 200–214, 2006.

[46] F. O'Sullivan, "A statistical perspective on ill-posed inverse problems," *Statistical science*, pp. 502–518, 1986.

[47] J. Kaipio, V. Kolehmainen, M. Vauhkonen, and E. Somersalo, "Inverse problems with structural prior information," *Inverse problems*, vol. 15, no. 3, p. 713, 1999.

[48] M. M. Lavrent_ev, V. G. Romanov, and S. P. Shishatski_, *Ill-posed problems of mathematical physics and analysis*. American Mathematical Soc., 1986, vol. 64.

[49] T. Poggio and V. Torre, "Ill-posed problems and regularization analysis in early vision," DTIC Document, Tech. Rep., 1984.

[50] D. Kimes, Y. Knyazikhin, J. Privette, A. Abuelgasim, and F. Gao, "Inversion methods for physically-based models," *Remote Sensing Reviews*, vol. 18, no. 2-4, pp. 381–439, 2000.

[51] V. Turchin, V. Kozlov, and M. Malkevich, "The use of mathematical-statistics methods in the solution of incorrectly posed problems," *Physics-Uspekhi*, vol. 13, no. 6, pp. 681–703, 1971.

[52] Y. Robert-Nicoud, B. Raphael, and I. Smith, "System identification through model composition and stochastic search," *Journal of computing in civil engineering*, vol. 19, no. 3, pp. 239–247, 2005.

[53] W. M. Bulleit, "Uncertainty in structural engineering," *Practice Periodical on Structural Design and Construction*, vol. 13, no. 1, pp. 24–30, 2008.

[54] O. Ditlevsen, "Model uncertainty in structural reliability," *Structural safety*, vol. 1, no. 1, pp. 73–86, 1983.

[55] A. Der Kiureghian and O. Ditlevsen, "Aleatory or epistemic? does it matter?" *Structural Safety*, vol. 31, no. 2, pp. 105–112, 2009.

[56] K. Sörensen, *Tabu searching for robust solutions.* Citeseer, 2002.

[57] Y. Ben-Haim, "Info-gap decision theory for engineering design. or: why 'good' is preferable to 'best'," *Engineering Design Reliability Handbook, CRC Press, Boca Raton*, 2005.

[58] J. M. Mulvey, R. J. Vanderbei, and S. A. Zenios, "Robust optimization of large-scale systems," *Operations research*, vol. 43, no. 2, pp. 264–281, 1995.

[59] M. S. Phadke, *Quality engineering using robust design.* Prentice Hall PTR, 1995.

[60] K.-H. Lee and G.-J. Park, "Robust optimization considering tolerances of design variables," *Computers & Structures*, vol. 79, no. 1, pp. 77–86, 2001.

[61] E. Sandgren and T. Cameron, "Robust design optimization of structures through consideration of variation," *Computers & structures*, vol. 80, no. 20, pp. 1605–1613, 2002.

[62] I. Doltsinis and Z. Kang, "Robust design of structures using optimization methods," *Computer Methods in Applied Mechanics and Engineering*, vol. 193, no. 23, pp. 2221–2237, 2004.

[63] C. Zang, M. Friswell, and J. Mottershead, "A review of robust optimal design and its application in dynamics," *Computers & structures*, vol. 83, no. 4, pp. 315–326, 2005.

[64] Y. Ben-Haim, *Info-gap decision theory: decisions under severe uncertainty.* Academic Press, 2006.

[65] ——, "Design certification with information-gap uncertainty," *Structural Safety*, vol. 21, no. 3, pp. 269–289, 1999.

[66] S. Prabhu and S. Atamturktur, "A review on prognostic evaluation of historic masonry structures: Present challenges and future direction(accepted, in print)," *The Masonry Society Journal*, 2015.

[67] S. Atamturktur, S. Prabhu, and G. Roche, "Predictive modeling of large scale historic masonry monuments: uncertainty quantification and model validation,"

in *Proceedings of the 9th International Conference on Structural Dynamics, EURODYN 2014*, Porto, Portugal, June 2014, pp. 2721–2727.

[68] S. Prabhu, S. Atamturktur, and S. Cogan, "Model selection in scientific computing: Considering robustness to bounded uncertainty in input parameters (conditionally accepted)," *Computers and Structures*, 2015.

[69] S. Prabhu, S. Atamturktur, D. Brosnan, P. Messier, and R. Dorrance, "Foundation settlement analysis of fort sumter national monument: Model development and predictive assessment," *Engineering Structures*, vol. 65, pp. 1–12, 2014.

[70] S. Prabhu and S. Atamturktur, "Assessment of strength degradation due to damage using load path based approach(submitted)," *ASCE Journal of Structural Engineering*, 2015.

[71] L. Binda, G. Gatti, G. Mangano, C. Poggi, and G. S. Landriani, "Collapse of the civic tower of pavia: a survey of the materials and structure," *Masonry International*, vol. 6, no. 1, pp. 11–20, 1992.

[72] E. Verstrynge, L. Schueremans, D. Van Gemert, and M. Hendriks, "Modelling and analysis of time-dependent behaviour of historical masonry under high stress levels," *Engineering Structures*, vol. 33, no. 1, pp. 210–217, 2011.

[73] L. Binda, G. Baronio, C. Gavarini, R. De Benedictis, and S. Tringali, "Investigation on materials and structures for the reconstruction of the partially collapsed cathedral of noto (sicily)," in *International conference structural studies, repairs and maintenance of historical buildings*, 1999, pp. 323–332.

[74] E. Verstrynge, S. Ignoul, L. Schueremans, D. Van Gemert, and W. Wevers, "Long term behaviour of historical masonry–a quantitative acquisition of the

damage evolution," in *SAHC08–6th International Conference on Structural Analysis of Historical Constructions*, 2008, pp. 2–4.

[75] J. C. Jaeger, N. G. Cook, and R. Zimmerman, *Fundamentals of rock mechanics.* John Wiley and Sons, 2009.

[76] D. Potts and T. Addenbrooke, "A structure's influence on tunnelling induced ground movements," *Proceedings of the Institution of Civil Engineers-Geotechnical Engineering*, vol. 125, no. 2, pp. 109–125, 1997.

[77] H. Burd, G. Houlsby, C. Augarde, and G. Liu, "Prediction of tunnel-induced settlement damage to masonry structures," *OUEL Report 2162/98, Department of Engineering Science, Oxford University*, 1998.

[78] C. E. Augarde, "Numerical modelling of tunnelling processes for assessment of damage to buildings," Ph.D. dissertation, University of Oxford, 1997.

[79] C. G. Balachandran, "Assessment of construction vibration impacts on historic structures," *Journal of the Acoustic Society of America*, vol. 103, no. 5, pp. 3022–3022, 1998.

[80] A. Erkal, D. Laefer, P. Fanning, E. Durukal, U. Hancilar, and Y. Kaya, "Investigation of the rail-induced vibrations on a masonry historical building," *Advanced Materials Research*, vol. 133, pp. 569–574, 2010.

[81] O. Hunaidi, *Traffic vibrations in buildings.* Institute for Research in Construction, National Research Council of Canada, 2000.

[82] L. Binda, M. Falco, C. Poggi, A. Zasso, G. M. Roberti, R. Corradi, and R. T. Folli, "Static and dynamic studies on the torrazzo in cremona (italy): the highest

masonry bell tower in europe," in *International symposium on Bridging Large Spans (BLS) from antiquity to the present, Istanbul, Turkey*, 2000, pp. 100–110.

[83] J. Pina-Henriques and P. B. Lourenço, "Testing and modelling of masonry creep and damage in uniaxial compression," *Struct Stud Repairs Maint Herit Archit*, vol. 8, no. 16, pp. 151–160, 2003.

[84] A. Anzani, E. Garavaglia, and L. Binda, "Long-term damage of historic masonry: A probabilistic model," *Construction and Building Materials*, vol. 23, no. 2, pp. 713–724, 2009.

[85] H. Twelmeier, S. Sperbeck, and H. Budelmann, "Durability prognosis model of historical natural stone masonry regarding joint repairing measures," in *Proceedings of the 5th International Conference on Structural Analysis of Historical Constructions: possibilities of numerical and experimental techniques*. Macmillan, 2006, p. 1051.

[86] C. T. Grimm, "Water permeance of masonry walls: a review of the literature," *Masonry: materials, properties and performance, ASTM STP*, vol. 778, pp. 178–199, 1982.

[87] M. Collepardi, "Degradation and restoration of masonry walls of historical buildings," *Materials and Structures*, vol. 23, no. 2, pp. 81–102, 1990.

[88] C. J. Groot and J. Gunneweg, "Water permeance problems in single wythe masonry walls: the case of wind mills," *Construction and Building Materials*, vol. 18, no. 5, pp. 325–329, 2004.

[89] R. C. Mack and A. E. Grimmer, *Assessing Cleaning and Water-Repellent Treatments for Historic Masonry Buildings*. Government Printing Office, 2000.

[90] A. Mishra, K. K. Jain, and K. Garg, "Role of higher plants in the deterioration of historic buildings," *Science of the total environment*, vol. 167, no. 1, pp. 375–392, 1995.

[91] G. Caneva, G. Galotta, L. Cancellieri, and V. Savo, "Tree roots and damages in the jewish catacombs of villa torlonia (roma)," *Journal of Cultural Heritage*, vol. 10, no. 1, pp. 53–62, 2009.

[92] E. Uchida, Y. Ogawa, N. Maeda, and T. Nakagawa, "Deterioration of stone materials in the angkor monuments, cambodia," *Engineering Geology*, vol. 55, no. 1, pp. 101–112, 2000.

[93] P. B. Lourenço, "Computations on historic masonry structures," *Progress in Structural Engineering and Materials*, vol. 4, no. 3, pp. 301–319, 2002.

[94] P. B. Lourenço, "Computations on historic masonry structures," *Progress in Structural Engineering and Materials*, vol. 4, no. 3, pp. 301–319, 2002.

[95] P. Roca, M. Cervera, G. Gariup *et al.*, "Structural analysis of masonry historical constructions. classical and advanced approaches," *Archives of Computational Methods in Engineering*, vol. 17, no. 3, pp. 299–325, 2010.

[96] G. Macchi, G. Ruggeri, M. Eusebio, and M. Moncecchi, "Structural assessment of the leaning tower of pisa," *IABSE REPORTS*, pp. 401–401, 1993.

[97] A. Chiarugi, M. Fanelli, and G. Giuseppetti, "Diagnosis and strengthening of the brunelleschi dome," *IABSE REPORTS*, pp. 441–441, 1993.

[98] G. Croci and A. Viscovik, "Causes of failures of colosseum over the centuries and evaluation of the safety levels," *Public assembly structures. From antiquity to the present. IASS-Mimar Sinan University, Istanbul, Turkey*, pp. 29–52, 1993.

[99] G. Croci, "The colosseum: safety evaluation and preliminary criteria of intervention," *Structural Analysis of Historical Constructions, Barcelona*, 1995.

[100] R. Meli and A. R. Sanchez-Ramirez, "Rehabilitation of the mexico city cathedral," *Structural engineering international*, vol. 7, no. 2, pp. 101–106, 1997.

[101] F. Mola and R. Vitaliani, "Analysis, diagnosis and preservation of ancient monuments: the st mark's basilica in venice," in *1st International seminar on structural analysis of historical construction, Barcelona (Spain)*, 1997.

[102] T. Li and S. Atamturktur, "Fidelity and robustness of detailed micromodeling, simplified micromodeling, and macromodeling techniques for a masonry dome," *Journal of Performance of Constructed Facilities*, 2013.

[103] L. Macorini and B. Izzuddin, "Nonlinear analysis of masonry structures using mesoscale partitioned modelling," *Advances in Engineering Software*, vol. 60, pp. 58–69, 2013.

[104] O. Kamal, G. Hamdy, and T. El-Salakawy, "Nonlinear analysis of historic and contemporary vaulted masonry assemblages," *HBRC Journal*, vol. 10, no. 3, pp. 235–246, 2014.

[105] D. Theodossopoulos and B. Sinha, "A review of analytical methods in the current design processes and assessment of performance of masonry structures," *Construction and Building Materials*, vol. 41, pp. 990–1001, 2013.

[106] A. Zucchini and P. Lourenço, "A micro-mechanical model for the homogenisation of masonry," *International Journal of Solids and Structures*, vol. 39, no. 12, pp. 3233–3255, 2002.

[107] H. R. Lotfi and P. B. Shing, "Interface model applied to fracture of masonry structures," *Journal of structural engineering*, vol. 120, no. 1, pp. 63–80, 1994.

[108] P. B. Lourenço and J. G. Rots, "Multisurface interface model for analysis of masonry structures," *Journal of engineering mechanics*, vol. 123, no. 7, pp. 660–668, 1997.

[109] D. Sutcliffe, H. Yu, and A. Page, "Lower bound limit analysis of unreinforced masonry shear walls," *Computers & Structures*, vol. 79, no. 14, pp. 1295–1312, 2001.

[110] L. Gambarotta and S. Lagomarsino, "Damage models for the seismic response of brick masonry shear walls. part i: the mortar joint model and its applications," *Earthquake engineering & structural dynamics*, vol. 26, no. 4, pp. 423–439, 1997.

[111] C. Sandoval, P. Roca, E. Bernat, and L. Gil, "Testing and numerical modelling of buckling failure of masonry walls," *Construction and Building Materials*, vol. 25, no. 12, pp. 4394–4402, 2011.

[112] A. Colas, J. Morel, and D. Garnier, "Yield design of dry-stone masonry retaining structures - comparisons with analytical, numerical, and experimental data," *International journal for numerical and analytical methods in geomechanics*, vol. 32, no. 14, pp. 1817–1832, 2008.

[113] A. Cecchi and K. Sab, "Out of plane model for heterogeneous periodic materials: the case of masonry," *European Journal of Mechanics-A/Solids*, vol. 21, no. 5, pp. 715–746, 2002.

[114] I. Stefanou, K. Sab, and J.-V. Heck, "Three dimensional homogenization of masonry structures with building blocks of finite strength: A closed form strength

domain," *International Journal of Solids and Structures*, vol. 54, pp. 258–270, 2015.

[115] G. De Felice, A. Amorosi, and M. Malena, "Elasto-plastic analysis of block structures through a homogenization method," *International journal for numerical and analytical methods in geomechanics*, vol. 34, no. 3, pp. 221–247, 2010.

[116] G. Milani, P. B. Lourenço, and A. Tralli, "Homogenised limit analysis of masonry walls, part i: Failure surfaces," *Computers & structures*, vol. 84, no. 3, pp. 166–180, 2006.

[117] A. Anthoine, "Derivation of the in-plane elastic characteristics of masonry through homogenization theory," *International Journal of Solids and Structures*, vol. 32, no. 2, pp. 137–163, 1995.

[118] R. Luciano and E. Sacco, "Homogenization technique and damage model for old masonry material," *International Journal of Solids and Structures*, vol. 34, no. 24, pp. 3191–3208, 1997.

[119] G. Giambanco, S. Rizzo, and R. Spallino, "Numerical analysis of masonry structures via interface models," *Computer methods in applied mechanics and engineering*, vol. 190, no. 49, pp. 6493–6511, 2001.

[120] M. Ainsworth and L. A. Mihai, "Modeling and numerical analysis of masonry structures," *Numerical Methods for Partial Differential Equations*, vol. 23, no. 4, pp. 798–816, 2007.

[121] M. Son and E. J. Cording, "Responses of buildings with different structural types to excavation-induced ground settlements," *Journal of Geotechnical and Geoenvironmental Engineering*, vol. 137, no. 4, pp. 323–333, 2010.

[122] T. Ford, C. Augarde, and S. Tuxford, "Modelling masonry arch bridges using commercial finite element software," in *Proceedings of the 9th International Conference on Civil and Structural Engineering Computing, BHV Topping, ed., The Netherlands*, 2003.

[123] G. Liu, G. Houlsby, and C. Augarde, "2-dimensional analysis of settlement damage to masonry buildings caused by tunnelling," *Structural Engineer*, vol. 79, no. 1, pp. 19–25, 2001.

[124] H. Burd, G. Houlsby, C. Augarde, and G. Liu, "Modelling tunnelling-induced settlement of masonry buildings," *Proceedings of the ICE-Geotechnical Engineering*, vol. 143, no. 1, pp. 17–29, 2000.

[125] A. Bloodworth, G. Houlsby, H. Burd, and C. Augarde, "Three-dimensional modelling of the interaction between buildings and tunnelling operations," 2001.

[126] G. Giardina, M. A. Hendriks, and J. G. Rots, "Numerical analyses of tunnel-induced settlement damage to a masonry wall," in *7th fib PhD Symposium in Stuttgart, Germany*, 2008, pp. 11–13.

[127] J. Rots, "The role of structural modelling in preserving amsterdam architectural city heritage," *Historical constructions. Guimarães, Portugal*, pp. 685–696, 2001.

[128] S. Invernizzi, G. Lacidogna, A. Manuello, and A. Carpinteri, "Damage assessment of a two-span model masonry arch bridge," in *Proceedings of the SEM Annual Conference. Albuquerque, USA*, 2009.

[129] N. Domede, A. Sellier, and T. Stablon, "Structural analysis of a multi-span railway masonry bridge combining in situ observations, laboratory tests and damage modelling," *Engineering Structures*, vol. 56, pp. 837–849, 2013.

[130] H. M. Yilmaz, M. Yakar, S. A. Gulec, and O. N. Dulgerler, "Importance of digital close-range photogrammetry in documentation of cultural heritage," *Journal of Cultural Heritage*, vol. 8, no. 4, pp. 428–433, 2007.

[131] P. Arias, J. Armesto, D. Di-Capua, R. GonzÃ¡lez-Drigo, H. Lorenzo, and V. PÃ©rez-Gracia, "Digital photogrammetry, gpr and computational analysis of structural damages in a mediaeval bridge," *Engineering Failure Analysis*, vol. 14, no. 8, pp. 1444–1457, 2007.

[132] N. Yastikli, "Documentation of cultural heritage using digital photogrammetry and laser scanning," *Journal of Cultural Heritage*, vol. 8, no. 4, pp. 423–427, 2007.

[133] Y. Fujii, E. Fodde, K. Watanabe, and K. Murakami, "Digital photogrammetry for the documentation of structural damage in earthen archaeological sites: The case of ajina tepa, tajikistan," *Engineering Geology*, vol. 105, no. 1, pp. 124–133, 2009.

[134] J. Armesto, J. Roca-Pardiñas, H. Lorenzo, and P. Arias, "Modelling masonry arches shape using terrestrial laser scanning data and nonparametric methods," *Engineering Structures*, vol. 32, no. 2, pp. 607–615, 2010.

[135] I. Lubowiecka, J. Armesto, P. Arias, and H. Lorenzo, "Historic bridge modelling using laser scanning, ground penetrating radar and finite element methods in the context of structural dynamics," *Engineering Structures*, vol. 31, no. 11, pp. 2667–2676, 2009.

[136] L. Schueremans and B. Van Genechten, "The use of 3d-laser scanning in assessing the safety of masonry vaults - a case study on the church of saint-jacobs," *Optics and Lasers in Engineering*, vol. 47, no. 3, pp. 329–335, 2009.

[137] C. Colla, P. Das, D. McCann, and M. Forde, "Sonic, electromagnetic and impulse radar investigation of stone masonry bridges," *NDT and E International*, vol. 30, no. 4, pp. 249–254, 1997.

[138] J. J. Hughes and K. Callebaut, "Practical sampling of historic mortars," in *RILEM International Workshop, Historic Mortars: Characteristics and tests, PJM Bartos, CJWP Groot and JJ Hughes (eds.), RILEM proceedings PRO*, vol. 12, 2000, pp. 17–26.

[139] R. Capozucca, "Experimental analysis of historic masonry walls reinforced by cfrp under in-plane cyclic loading," *Composite Structures*, vol. 94, no. 1, pp. 277–289, 2011.

[140] C. Modena, M. R. Valluzzi, F. da Porto, and F. Casarin, "Structural aspects of the conservation of historic masonry constructions in seismic areas: remedial measures and emergency actions," *International Journal of Architectural Heritage*, vol. 5, no. 4-5, pp. 539–558, 2011.

[141] P. B. Lourenço, J. G. Rots, and J. Blaauwendraad, "Continuum model for masonry: parameter estimation and validation," *Journal of structural engineering*, vol. 124, no. 6, pp. 642–652, 1998.

[142] S. Pietruszczak and X. Niu, "A mathematical description of macroscopic behaviour of brick masonry," *International journal of solids and structures*, vol. 29, no. 5, pp. 531–546, 1992.

[143] G. Pande, J. Liang, and J. Middleton, "Equivalent elastic moduli for brick masonry," *Computers and Geotechnics*, vol. 8, no. 3, pp. 243–265, 1989.

[144] P. De Buhan and G. De Felice, "A homogenization approach to the ultimate strength of brick masonry," *Journal of the Mechanics and Physics of Solids*, vol. 45, no. 7, pp. 1085–1104, 1997.

[145] P. B. Lourénço, R. De Borst, and J. G. Rots, "A plane stress softening plasticity model for orthotropic materials," *International Journal for Numerical Methods in Engineering 40 (21), 4033-4057.(1997)*, 1997.

[146] L. Berto, A. Saetta, R. Scotta, and R. Vitaliani, "An orthotropic damage model for masonry structures," *International Journal for Numerical Methods in Engineering*, vol. 55, no. 2, pp. 127–157, 2002.

[147] A. Cecchi and K. Sab, "A multi-parameter homogenization study for modeling elastic masonry," *European Journal of Mechanics-A/Solids*, vol. 21, no. 2, pp. 249–268, 2002.

[148] P. Pegon and A. Anthoine, "Numerical strategies for solving continuum damage problems with softening: application to the homogenization of masonry," *Computers & structures*, vol. 64, no. 1, pp. 623–642, 1997.

[149] G. Milani and P. B. Lourenço, "Monte carlo homogenized limit analysis model for randomly assembled blocks in-plane loaded," *Computational Mechanics*, vol. 46, no. 6, pp. 827–849, 2010.

[150] A. A. Costa, B. Quelhas, and J. P. Almeida, "Numerical modelling approaches for existing masonry and rc structures," in *Structural Rehabilitation of Old Buildings*. Springer, 2014, pp. 285–305.

147

[151] T. E. Boothby, H. S. Atamtürktür, and E. Erdogmus, "Manual for the assessment of load-bearing unreinforced masonry structures," *w ww. arche. psu. edu/masonryassessment*, 2006.

[152] A. Giordano, E. Mele, and A. De Luca, "Modelling of historical masonry structures: comparison of different approaches through a case study," *Engineering Structures*, vol. 24, no. 8, pp. 1057–1069, 2002.

[153] C. Gentile and A. Saisi, "Ambient vibration testing of historic masonry towers for structural identification and damage assessment," *Construction and Building Materials*, vol. 21, no. 6, pp. 1311–1321, 2007.

[154] S. Atamturktur, F. Hemez, and J. Laman, "Uncertainty quantification in model verification and validation as applied to large scale historic masonry monuments," *Engineering Structures*, vol. 43, pp. 221–234, 2012.

[155] R. H. MacNeal, "A hybrid method of component mode synthesis," *Computers and Structures*, vol. 1, no. 4, pp. 581–601, 1971.

[156] R. Craig, "A review of time-domain and frequency-domain component mode synthesis method," *Combined experimental/analytical modeling of dynamic structural systems*, pp. 1–30, 1985.

[157] W. C. Hurty, "Vibrations of structural systems by component mode synthesis," *Journal of the Engineering Mechanics Division*, vol. 86, no. 4, pp. 51–70, 1960.

[158] D.-M. Tran, "Component mode synthesis methods using interface modes. application to structures with cyclic symmetry," *Computers and Structures*, vol. 79, no. 2, pp. 209–222, 2001.

[159] H. Lotfi and P. Shing, "An appraisal of smeared crack models for masonry shear wall analysis," *Computers & structures*, vol. 41, no. 3, pp. 413–425, 1991.

[160] P. Fanning, "Nonlinear models of reinforced and post-tensioned concrete beams," *Electronic Journal of Structural Engineering*, vol. 1, pp. 111–119, 2001.

[161] P. Kohnke, *ANSYS, Inc. Theory: Release 5.7.* Ansys, 2001.

[162] S. Mahini, H. Ronagh, and A. Eslami, "Seismic rehabilitation of historical masonry vaults using frps–a case study," in *Proceeding of Asia-Pacific conference on FRP in structures (APFIS 2007)*, vol. 1, 2007.

[163] A. Carpinteri, G. Lacidogna, S. Invernizzi, A. Manuello, and L. Binda, "Stability of the vertical bearing structures of the syracuse cathedral: experimental and numerical evaluation," *Materials and structures*, vol. 42, no. 7, pp. 877–888, 2009.

[164] M. Betti and A. Vignoli, "Numerical assessment of the static and seismic behaviour of the basilica of santa maria all'impruneta (italy)," *Construction and Building Materials*, vol. 25, no. 12, pp. 4308–4324, 2011.

[165] R. Patrick, "Perspective: a method for uniform reporting of grid refinement studies," *Journal of Fluids Engineering*, vol. 116, no. 3, pp. 405–413, 1994.

[166] P. J. Roache and P. M. Knupp, "Completed richardson extrapolation," *Communications in Numerical Methods in Engineering*, vol. 9, no. 5, pp. 365–374, 1993.

[167] S. A. Richards, "Completed richardson extrapolation in space and time," *Communications in numerical methods in engineering*, vol. 13, no. 7, pp. 573–582, 1997.

[168] M. C. Kennedy and A. O'Hagan, "Bayesian calibration of computer models," *Journal of the Royal Statistical Society: Series B (Statistical Methodology)*, vol. 63, no. 3, pp. 425–464, 2001.

[169] T. G. Trucano, L. P. Swiler, T. Igusa, W. L. Oberkampf, and M. Pilch, "Calibration, validation, and sensitivity analysis: What's what," *Reliability Engineering & System Safety*, vol. 91, no. 10, pp. 1331–1357, 2006.

[170] A. De Stefano, "Structural identification and health monitoring on the historical architectural heritage," in *Key Engineering Materials*, vol. 347. Trans Tech Publ, 2007, pp. 37–54.

[171] E. Antonacci, A. De Sortis, and F. Vestroni, "Dynamic identification of masonry buildings by forced vibration tests," in *PROCEEDINGS OF THE INTERNATIONAL SEMINAR ON MODAL ANALYSIS*, vol. 3. KU Leuven; 1998, 2001, pp. 1669–1676.

[172] L. F. Ramos, *Damage identification on masonry structures based on vibration signatures*, 2007.

[173] T. Aoki, D. Sabia, D. Rivella, and H. Muto, "Dynamic identification and model updating of the hawa brick chimney, tokoname, japan," *Transactions on the built environment*, pp. 265–275, 2005.

[174] S. Atamturktur, "Validation and verification under uncertainty applied to finite element models of historic masonry monuments," in *Proceedings of 27th Society of Experimental Mechanics (SEM) International Modal Analysis Conference (IMAC-XXVII)*, 2009.

[175] E. N. B. S. Júlio, C. A. da Silva Rebelo, D. A. S. G. Dias-da *et al.*, "Structural assessment of the tower of the university of coimbra by modal identification," *Engineering Structures*, vol. 30, no. 12, pp. 3468–3477, 2008.

[176] S. Atamturktur and T. Boothby, "Stochastic bayesian calibration of finite element models of masonry vaults," *TMS J*, vol. 28, no. 2, pp. 77–93, 2010.

[177] B. Jaishi, W.-X. Ren, Z.-H. Zong, and P. N. Maskey, "Dynamic and seismic performance of old multi-tiered temples in nepal," *Engineering Structures*, vol. 25, no. 14, pp. 1827–1839, 2003.

[178] A. Bayraktar, A. Altunisik, B. Sevim, T. Turker, M. Akkose, and N. Coskun, "Modal analysis, experimental validation, and calibration of a historical masonry minaret," *Journal of testing and evaluation*, vol. 36, no. 6, p. 594, 2008.

[179] S. Prabhu and S. Atamturktur, "Feature assimilation for vibration based damage detection," *Evaluation*, vol. 41, no. 1, pp. 1–11, 2013.

[180] L. Binda, A. Saisi, and C. Tiraboschi, "Investigation procedures for the diagnosis of historic masonries," *Construction and Building Materials*, vol. 14, no. 4, pp. 199–233, 2000.

[181] S. Atamturktur, T. Li, M. H. Ramage, and I. Farajpour, "Load carrying capacity assessment of a scaled masonry dome: Simulations validated with non-destructive and destructive measurements," *Construction and Building Materials*, vol. 34, pp. 418–429, 2012.

[182] M. Pilch, *Guidelines for Sandia ASCI verification and validation plans-content and format: version 2.0.* Sandia National Laboratories, 2001.

[183] D. J. Diamond, "Experience using phenomena identification and ranking technique (pirt) for nuclear analysis," in *PHYSOR-2006 Topical Meeting, Vancouver, Canada*, 2006.

[184] J. Hegenderfer and S. Atamturktur, "Prioritization of code development efforts in partitioned analysis," *Computer-Aided Civil and Infrastructure Engineering*, vol. 28, no. 4, pp. 289–306, 2013.

[185] G. W. Milligan, "A review of monte carlo tests of cluster analysis," *Multivariate Behavioral Research*, vol. 16, no. 3, pp. 379–407, 1981.

[186] R. De Maesschalck, D. Jouan-Rimbaud, and D. L. Massart, "The mahalanobis distance," *Chemometrics and intelligent laboratory systems*, vol. 50, no. 1, pp. 1–18, 2000.

[187] E. Choi and C. Lee, "Feature extraction based on the bhattacharyya distance," *Pattern Recognition*, vol. 36, no. 8, pp. 1703–1709, 2003.

[188] I. Farajpour and S. Atamturktur, "Error and uncertainty analysis of inexact and imprecise computer models," *Journal of Computing in Civil Engineering*, vol. 27, no. 4, pp. 407–418, 2012.

[189] F. Hemez, H. S. Atamturktur, and C. Unal, "Defining predictive maturity for validated numerical simulations," *Computers & structures*, vol. 88, no. 7, pp. 497–505, 2010.

[190] J. Mankin, R. O'Neill, H. Shugart, and B. Rust, "The importance of validation in ecosystem analysis," *New directions in the analysis of ecological systems, part*, vol. 1, pp. 63–71, 1975.

[191] P. J. Kiviat, "Digital computer simulation: modeling concepts," DTIC Document, Tech. Rep., 1967.

[192] S. K. Gupta and J. Rosenhead, "Robustness in sequential investment decisions," *Management Science*, vol. 15, no. 2, pp. B–18–B–29, 1968.

[193] J. Rosenhead, M. Elton, and S. K. Gupta, "Robustness and optimality as criteria for strategic decisions," *Operational Research Quarterly*, pp. 413–431, 1972.

[194] I. Elishakoff, R. Haftka, and J. Fang, "Strutural design under bounded uncertainty - optimization with anti-optimization," *Computers and structures*, vol. 53, no. 6, pp. 1401–1405, 1994.

[195] Y. Ben-Haim and I. Elishakoff, *Convex Models of Uncertainty in Applied Mechanics*, ser. Studies in Applied Mechanics. Elsevier Science, 1990. [Online]. Available: http://books.google.com/books?id=nkovBQAAQBAJ

[196] A. Berman, "Multiple acceptable solutions in structural model improvement," *AIAA journal*, vol. 33, no. 5, pp. 924–927, 1995.

[197] J. G. March and H. A. Simon, "Organizations." 1958.

[198] H. A. Simon, "Theories of decision-making in economics and behavioral science," *The American Economic Review*, vol. 49, no. 3, pp. pp. 253–283, 1959. [Online]. Available: http://www.jstor.org/stable/1809901

[199] R. L. Mayes, "Developing adequacy criterion for model validation based on requirements," *Proceedings of the IMAC-XXVII*, pp. 8–12, 2009.

[200] M. Starr, "Discussion of some normative criteria for decision-making under uncertainty," *Industrial Management Review*, vol. 8, no. 1, pp. 71–78, 1966.

[201] J. R. Charnetski and R. M. Soland, "Multiple-attribute decision making with partial information: The comparative hypervolume criterion," *Naval Research Logistics Quarterly*, vol. 25, no. 2, pp. 279–288, 1978. [Online]. Available: http://dx.doi.org/10.1002/nav.3800250208

[202] R. Vetschera, "A recursive algorithm for volume-based sensitivity analysis of linear decision models," *Comput. Oper. Res.*, vol. 24, no. 5, pp. 477–491, May 1997. [Online]. Available: http://dx.doi.org/10.1016/S0305-0548(96)00073-1

[203] G. Schneller IV and G. Sphicas, "Decision making under uncertainty: Starr's domain criterion," *Theory and Decision*, vol. 15, no. 4, pp. 321–336, 1983.

[204] H. A. Eiselt and A. Langley, "Some extensions of domain criteria in decision making under uncertainty*," *Decision Sciences*, vol. 21, no. 1, pp. 138–153, 1990.

[205] S. Bi, S. Atamturktur, and Z. Deng, "Comparative study of uncertainty quantification metrics via a stochastic method of model validation," in *Dynamics of Civil Structures, Volume 4.* Springer, 2014, pp. 235–243.

[206] S. Sakurai, B. R. Ellingwood, and S. Kushiyama, "Probabilistic study of the behavior of steel frames with partially restrained connections," *Engineering structures*, vol. 23, no. 11, pp. 1410–1417, 2001.

[207] C. Díaz, M. Victoria, O. M. Querin, and P. Martí, "Optimum design of semirigid connections using metamodels," *Journal of Constructional Steel Research*, vol. 78, pp. 97–106, 2012.

[208] K.-J. Bathe, *Finite element procedures.* Klaus-Jurgen Bathe, 2006.

[209] R. Grant, J. T. Christian, and E. H. Vanmarcke, "Differential settlement of buildings," *Journal of the Geotechnical Engineering Division*, vol. 100, no. 9, pp. 973–991, 1974.

[210] D. Polshin and R. Tokar, "Maximum allowable non-uniform settlement of structures," in *Proceedings Fourth International Conference on Soil Mechanics and Foundation Engineering*, vol. 1, 1957, pp. 402–405.

[211] A. W. Skempton and D. H. MacDonald, "The allowable settlements of buildings." in *ICE proceedings: engineering divisions*, vol. 5. Thomas Telford, 1956, pp. 727–768.

[212] H. Walhls, "Tolerable settlement of buildings," *Journal of Geotechnical and Geoenvironmental Engineering*, vol. 107, no. ASCE 16628 Proceeding, 1981.

[213] C. E. Augarde, *Numerical modelling of tunnelling processes for assessment of damage to buildings*, 1997.

[214] J. Rots, "Settlement damage predictions for masonry," in *Maintenance and restrengthening of materials and structures: Brick and brickwork. Proc. Int. Workshop on urban heritage and building maintenance*, 2000, pp. 47–62.

[215] P. Roca, *Structural analysis of historical constructions: possibilities of numerical and experimental techniques*. International Center for Numerical Methods in Engineering CIMNE, 1997.

[216] P. B. Lourenço, "Recommendations for restoration of ancient buildings and the survival of a masonry chimney," *Construction and Building Materials*, vol. 20, no. 4, pp. 239–251, 2006.

[217] A. D. Sortis, E. Antonacci, and F. Vestroni, "Dynamic identification of a masonry building using forced vibration tests," *Engineering Structures*, vol. 27, no. 2, pp. 155–165, 2005.

[218] C. Gentile and A. Saisi, "Ambient vibration testing of historic masonry towers for structural identification and damage assessment," *Construction and Building Materials*, vol. 21, no. 6, pp. 1311–1321, 2007.

[219] A. F. Hunter and C. L. Symonds, *A Year on a Monitor and the Destruction of Fort Sumter*. University of South Carolina Press, 1987.

[220] J. Johnson, *The Defense of Charleston Harbor: Including Fort Sumter and the Adjacent Islands, 1863-1865*. Walker, Evans and Cogswell Company, 1890.

[221] F. Barnes, *Fort Sumter: Anvil of War: Fort Sumter National Monument, South Carolina*. Division of Publications, National Park Service, 1984.

[222] D. A. Brosnan, J. P. Sanders, and R. P. Stroble, "Application of thermal analysis in preservation and restoration of historic masonry materials," *Journal of thermal analysis and calorimetry*, vol. 113, no. 2, pp. 507–510, 2013.

[223] G. Treussart, "On hydraulic and common mortars," *Journal of the Franklin Institute*, vol. 25, no. 4, pp. 217–245, 1838.

[224] T. E. Clark, *Falling to pieces: the preservation of ruins in coastal Georgia*, 2006.

[225] S. Atamturktur and B. Sevim, "Seismic performance assessment of masonry tile domes through nonlinear finite-element analysis," *Journal of Performance of Constructed Facilities*, vol. 26, no. 4, pp. 410–423, 2011.

[226] G. Drosopoulos, G. Stavroulakis, and C. Massalas, "Influence of the geometry and the abutments movement on the collapse of stone arch bridges," *Construction and Building Materials*, vol. 22, no. 3, pp. 200–210, 2008.

[227] B. Riveiro, J. Caamaño, P. Arias, and E. Sanz, "Photogrammetric 3d modelling and mechanical analysis of masonry arches: An approach based on a discontinuous model of voussoirs," *Automation in Construction*, vol. 20, no. 4, pp. 380–388, 2011.

[228] S. Atamturktur, A. Pavic, P. Reynolds, and T. Boothby, "Full-scale modal testing of vaulted gothic churches: lessons learned," *Experimental Techniques*, vol. 33, no. 4, pp. 65–74, 2009.

[229] R. Brincker, L. Zhang, and P. Andersen, "Output-only modal analysis by frequency domain decomposition," in *The International Conference on Noise and Vibration Engineering*, 2001, pp. 717–723.

[230] S. Gade, N. MÃžller, H. Herlufsen, and H. Konstantin-Hansen, "Frequency domain techniques for operational modal analysis," in *Proceedings 1st IOMAC Conference*, 2005, pp. 26–27.

[231] K. William and E. Warnke, "Constitutive model for the triaxial behavior of concrete," 1975.

[232] P. Kohnke, *ANSYS theory reference*.   Ansys, 1999.

[233] F. Queiroz, P. Vellasco, and D. Nethercot, "Finite element modelling of composite beams with full and partial shear connection," *Journal of Constructional Steel Research*, vol. 63, no. 4, pp. 505–521, 2007.

[234] F. Cubel, A. Mas, J. Vercher, and E. Gil, "Design and construction recommendations for brick enclosures with continuous air chamber," *Construction and Building Materials*, vol. 36, pp. 151–164, 2012.

[235] ANSYS, *Element Reference Release 12.1.* ANSYS Inc., 2009.

[236] C. B. Brown, J. R. Tilton, and J. M. Laurent, "Beam-plate system on winkler foundation," *Journal of the Engineering Mechanics Division*, vol. 103, no. 4, pp. 589–600, 1977.

[237] S. C. Dutta and R. Roy, "A critical review on idealization and modeling for interaction among soil-foundation-structure system," *Computers and Structures*, vol. 80, no. 20, pp. 1579–1594, 2002.

[238] K.-J. Bathe, *Finite element procedures.* Klaus-Jurgen Bathe, 2006.

[239] H. Sohn, "Effects of environmental and operational variability on structural health monitoring," *Philosophical transactions.Series A, Mathematical, physical, and engineering sciences*, vol. 365, no. 1851, pp. 539–560, Feb 15 2007, lR: 20130424; JID: 101133385; RF: 85; ppublish.

[240] R. C. Jr, "Methods of component mode synthesis," 1977.

[241] S. Ali, I. Moore, and A. Page, "Substructuring technique in nonlinear analysis of brick masonry subjected to concentrated load," *Computers and Structures*, vol. 27, no. 3, pp. 417–425, 1987.

[242] R. R. Craig, "Coupling of substructures for dynamic analyses: an overview," in *Proceedings of AIAA/ASME/ASCE/AHS/ASC structures, structural dynamics, and materials conference and exhibit*, 2000, pp. 1573–1584.

[243] M. Bampton and J. C. RR, "Coupling of substructures for dynamic analyses." *AIAA Journal*, vol. 6, no. 7, pp. 1313–1319, 1968.

[244] R. Craig, "Substructure methods in vibration," *Journal of Vibration and Acoustics*, vol. 117, no. B, pp. 207–213, 1995.

[245] D.-M. Tran, "Component mode synthesis methods using partial interface modes: Application to tuned and mistuned structures with cyclic symmetry," *Computers and Structures*, vol. 87, no. 17, pp. 1141–1153, 2009.

[246] E. Erdogmus, T. E. Boothby, and E. B. Smith, "Structural appraisal of the florentine gothic construction system," *Journal of Architectural Engineering*, vol. 13, no. 1, pp. 9–17, 2007.

[247] S. Atamturktur, L. Bornn, and F. Hemez, "Damage detection in masonry vaults by time-domain vibration measurements," *Journal of Engineering Structures*, 2009.

[248] P. Avitabile, "Experimental modal analysis," *Sound and vibration*, vol. 35, no. 1, pp. 20–31, 2001.

[249] D. J. Ewins, *Modal testing: theory, practice and application*. Research studies press Baldock, 2000, vol. 2.

[250] C. Burrus and T. Parks, "Digital filter design," *New York*, 1987.

[251] S. Han and J.-B. Lee, "Analysis of errors in the conversion of acceleration into displacement," *Proceedings of 19th IMAC, CD ROM*, 2001.

[252] R. J. Allemang, "The modal assurance criterion-twenty years of use and abuse," *Sound and vibration*, vol. 37, no. 8, pp. 14–23, 2003.

[253] J. D'Errico, "Polyfitn function," *Mathworks Central Repository, www.mathworks.com*, 2006.

[254] S. W. Doebling, C. R. Farrar, M. B. Prime, and D. W. Shevitz, "Damage identification and health monitoring of structural and mechanical systems from changes in their vibration characteristics: a literature review," Los Alamos National Lab., NM (United States), Tech. Rep., 1996.

[255] H. Sohn, C. R. Farrar, F. M. Hemez, D. D. Shunk, D. W. Stinemates, B. R. Nadler, and J. J. Czarnecki, *A review of structural health monitoring literature: 1996-2001.* Los Alamos National Laboratory Los Alamos, NM, 2004.

[256] W. Fan and P. Qiao, "Vibration-based damage identification methods: a review and comparative study," *Structural Health Monitoring*, vol. 10, no. 1, pp. 83–111, 2011.

[257] C. R. Farrar, S. W. Doebling, and D. A. Nix, "Vibration–based structural damage identification," *Philosophical Transactions of the Royal Society of London. Series A: Mathematical, Physical and Engineering Sciences*, vol. 359, no. 1778, pp. 131–149, 2001.

[258] A. Rytter, "Vibrational based inspection of civil engineering structures," Ph.D. dissertation, unknown, 1993.

[259] J. M. Brownjohn, A. De Stefano, Y.-L. Xu, H. Wenzel, and A. E. Aktan, "Vibration-based monitoring of civil infrastructure: challenges and successes," *Journal of Civil Structural Health Monitoring*, vol. 1, no. 3-4, pp. 79–95, 2011.

[260] K. Worden, C. R. Farrar, G. Manson, and G. Park, "The fundamental axioms of structural health monitoring," *Proceedings of the Royal Society A: Mathe-*

matical, Physical and Engineering Science, vol. 463, no. 2082, pp. 1639–1664, 2007.

[261] E. P. Carden and P. Fanning, "Vibration based condition monitoring: a review," *Structural health monitoring*, vol. 3, no. 4, pp. 355–377, 2004.

[262] E. Cross, K. Wordon, and C. Farrar, "Structural health monitoring for civil infrastructure," *Health assessment of engineered structures. World Scientific Publishing*, p. 1, 2013.

[263] H. Sohn, C. R. Farrar, N. F. Hunter, and K. Worden, "Structural health monitoring using statistical pattern recognition techniques," *Journal of dynamic systems, measurement, and control*, vol. 123, no. 4, pp. 706–711, 2001.

[264] B. Peeters, "System identification and damage detection in civil engeneering," 2000.

[265] D. Armstrong, A. Sibbald, C. Fairfield, and M. Forde, "Modal analysis for masonry arch bridge spandrell wall separation identification," *NDT and E International*, vol. 28, no. 6, pp. 377–386, 1995.

[266] F. Vestroni, G. Beolchini, E. Antonacci, and C. Modena, "Identification of dynamic characteristics of masonry buildings from forced vibration tests," in *Proceedings of the 11th World Conference on Earthquake Engineering*, 1996.

[267] A. Bensalem, H. Ali-Ahmed, C. Fairfield, and A. Sibbald, "Non-destructive testing to detect voids hidden behind the extrados of an arch bridge," *NDT and E International*, vol. 32, no. 6, pp. 343–353, 1999.

[268] A. De Sortis, E. Antonacci, and F. Vestroni, "Dynamic identification of a masonry building using forced vibration tests," *Engineering Structures*, vol. 27, no. 2, pp. 155–165, 2005.

[269] C. Gentile and A. Saisi, "Ambient vibration testing of historic masonry towers for structural identification and damage assessment," *Construction and Building Materials*, vol. 21, no. 6, pp. 1311–1321, 2007.

[270] L. F. Ramos, G. De Roeck, P. B. Lourenço, and A. Campos-Costa, "Damage identification on arched masonry structures using ambient and random impact vibrations," *Engineering Structures*, vol. 32, no. 1, pp. 146–162, 2010.

[271] S. Atamturktur, L. Bornn, and F. Hemez, "Vibration characteristics of vaulted masonry monuments undergoing differential support settlement," *Engineering Structures*, vol. 33, no. 9, pp. 2472–2484, 2011.

[272] S. Atamturktur, A. Pavic, P. Reynolds, and T. Boothby, "Full-scale modal testing of vaulted gothic churches: lessons learned," *Experimental Techniques*, vol. 33, no. 4, pp. 65–74, 2009.

[273] D. M. Frangopol and J. P. Curley, "Effects of damage and redundancy on structural reliability," *Journal of Structural Engineering*, vol. 113, no. 7, pp. 1533–1549, 1987.

[274] M. Ghosn, F. Moses, and D. M. Frangopol, "Redundancy and robustness of highway bridge superstructures and substructures," *Structure and Infrastructure Engineering*, vol. 6, no. 1-2, pp. 257–278, 2010.

[275] A. De Stefano and R. Ceravolo, "Assessing the health state of ancient structures: the role of vibrational tests," *Journal of intelligent material systems and structures*, vol. 18, no. 8, pp. 793–807, 2007.

[276] S. Podesta, G. Riotto, and F. Marazzi, "Reliability of dynamic identification techniques connected to structural monitoring of monumental buildings," *Structural Control and Health Monitoring*, vol. 15, no. 4, pp. 622–641, 2008.

[277] E. Antonacci, G. Beolchini, F. Di Fabio, and V. Gatullini, "Retrofitting effects on the dynamic behaviour of basilica s. maria di collemaggio," *Computational Methods and Experimental Measurements*, vol. 10, pp. 479–488, 2001.

[278] M. Turek, C. E. Ventura, and P. Placencia, "Dynamic characteristics of a 17th century church in quito, ecuador," in *Proceedings of SPIE*, vol. 4753, no. 2, 2002, pp. 1259–1264.

[279] L. F. Ramos, L. Marques, P. B. Lourenço, G. De Roeck, A. Campos-Costa, and J. Roque, "Monitoring historical masonry structures with operational modal analysis: Two case studies," *Mechanical Systems and Signal Processing*, vol. 24, no. 5, pp. 1291–1305, 2010.

[280] S. Russo, "On the monitoring of historic anime sante church damaged by earthquake in l'aquila," *Structural Control and Health Monitoring*, vol. 20, no. 9, pp. 1226–1239, 2013.

[281] K. Worden, *Structural Health Monitoring using Pattern Recognition*. Springer, 2010.

[282] N. Stubbs, C. Sikorsky, S. Park, S. Choi, and R. Bolton, "A methodology to nondestructively evaluate the structural properties of bridges," in *Society for*

Experimental Mechanics, Inc, 17 th International Modal Analysis Conference., vol. 2, 1999, pp. 1260–1268.

[283] S. Law, H. Ward, G. Shi, R. Chen, P. Waldron, and C. Taylor, "Dynamic assessment of bridge load-carrying capacities. i," *Journal of Structural Engineering*, vol. 121, no. 3, pp. 478–487, 1995.

[284] ——, "Dynamic assessment of bridge load-carrying capacities. ii," *Journal of Structural Engineering*, vol. 121, no. 3, pp. 488–495, 1995.

[285] O. Yang, H. Li, J. Ou, and Q. Li, "Failure patterns and ultimate load-carrying capacity evolution of a prestressed concrete cable-stayed bridge: Case study," *Advances in Structural Engineering*, vol. 16, no. 7, pp. 1283–1296, 2013.

[286] X. Zhu and H. Hao, "Development of an integrated structural health monitoring system for bridge structures in operational conditions," *Frontiers of Structural and Civil Engineering*, vol. 6, no. 3, pp. 321–333, 2012.

[287] J.-H. Yi, S. Cho, K.-Y. Koo, C.-B. Yun, J.-T. Kim, C.-G. Lee, and W.-T. Lee, "Structural performance evaluation of a steel-plate girder bridge using ambient acceleration measurements," *Smart Structures and Systems*, vol. 3, no. 3, pp. 281–298, 2007.

[288] G. Brown, A. Pretlove, J. Ellick, V. Hogg, and B. Choo, "Changes in the dynamic characteristics of a masonry arch bridge subjected to monotonic loading to failure," in *Proceedings of the 1st international conference on arch bridges, Bolton (UK)*, 1995, pp. 375–383.

[289] A. Bensalem, H. Ali-Ahmed, C. Fairfield, and A. Sibbald, "Ndt as a tool for detection of gradual safety factor deterioration in loaded arches," in *Proc. II Int. Arch Br. Conf*, 1998, pp. 271–277.

[290] N. C. Lind, "A measure of vulnerability and damage tolerance," *Reliability Engineering and System Safety*, vol. 48, no. 1, pp. 1–6, 1995.

[291] B. Schafer and P. Bajpai, "Stability degradation and redundancy in damaged structures," *Engineering Structures*, vol. 27, no. 11, pp. 1642–1651, 2005.

[292] F. Biondini, D. M. Frangopol, and S. Restelli, "On structural robustness, redundancy and static indeterminacy," in *ASCE Structures Congress 2008*, 2008, pp. 24–26.

[293] U. Starossek and M. Haberland, "Disproportionate collapse: terminology and procedures," *Journal of Performance of Constructed Facilities*, vol. 24, no. 6, pp. 519–528, 2010.

[294] Y. Kanno and Y. Ben-Haim, "Redundancy and robustness, or when is redundancy redundant?" *Journal of Structural Engineering*, vol. 137, no. 9, pp. 935–945, 2011.

[295] M. Husain and P. Tsopelas, "Measures of structural redundancy in reinforced concrete buildings. i: redundancy indices," *Journal of Structural Engineering*, vol. 130, no. 11, pp. 1651–1658, 2004.

[296] P. Pandey and S. Barai, "Structural sensitivity as a measure of redundancy," *Journal of Structural Engineering*, vol. 123, no. 3, pp. 360–364, 1997.

[297] H. Harasaki and J. S. Arora, "New concepts of transferred and potential transferred forces in structures," *Computer methods in applied mechanics and engineering*, vol. 191, no. 3, pp. 385–406, 2001.

[298] S. Venkataraman, K. S. Marhadi, and M. A. Haney, "Investigating alternate load paths and damage tolerance of structures optimized for multiple load cases," in *50th AIAA/ASME/ASCE/AHS/ASC Structures, Structural Dynamics, and Materials Conference 17th AIAA/ASME/AHS Adaptive Structures Conference 11th AIAA No*, 2009, p. 2185.

[299] M. P. Bendsøe, "Optimal shape design as a material distribution problem," *Structural optimization*, vol. 1, no. 4, pp. 193–202, 1989.

[300] M. P. Bendsoe and O. Sigmund, *Topology optimization: theory, methods and applications*. Springer Science and Business Media, 2003.

[301] G. Ö. Özen, "Comparison of elastic and inelastic behavior of historic masonry structures at the low load levels," Ph.D. dissertation, Middle East Technical Univesrity, 2006.

[302] M. Kabir and A. Kalali, "In-plane numerical modelling of strengthened perforated masonry walls using frp under cyclic loading," *Asian Journal of Civil Engineering (BHRC)*, vol. 14, no. 1, pp. 161–179, 2013.

[303] A. D. Sorensen and E. Erdogmus, "Horizontal support displacement of a thin-tile masonry dome: Experiments and analysis," *Journal of Performance of Constructed Facilities*, 2013.

[304] J. Rots, P. Nauta, G. Kuster, and J. Blaauwendraad, "Smeared crack approach and fracture localization in concrete," *HERON, 30 (1), 1985*, 1985.

[305] M. H. Richardson and D. L. Formenti, "Parameter estimation from frequency response measurements using rational fraction polynomials," in *Proceedings of the International Modal Analysis Conference*, 1982, pp. 167–182.